.

A Proposal for a New Experiment

Using the Booster and NuMI Neutrino Beamlines: MicroBooNE

October 15, 2007

H. Chen, J. Farrell, F. Lanni, D. Lissauer, D. Makowiecki, J. Mead,

V. Radeka, S. Rescia, J. Sondericker, B. Yu

Brookhaven National Laboratory, Upton, NY

L. Bugel, J. M. Conrad, V. Nguyen, M. Shaevitz, W. Willis[‡]

Columbia University, New York, NY

C. James, S. Pordes, G. Rameika

Fermi National Accelerator Laboratory, Batavia, IL

C. Bromberg, D. Edmunds

Michigan State University, Lansing, MI

P. Nienaber

St. Mary's University of Minnesota, Winona, MN

S. Kopp, K. Lang

University of Texas at Austin, Austin, TX

C. Anderson, B. T. Fleming[†], S. Linden, M. Soderberg, J. Spitz

Yale University, New Haven, CT

[†]= Spokesperson, [‡]= Deputy Spokesperson

Contents

List of Tables

List of Figures

Chapter 1

Introduction

Liquid argon time projection chambers are one of the most promising technologies for future large scale neutrino detectors. Research and Development towards realizing these large detectors in the U.S. has been hampered by the lack of a real proof of principle experiment using this technology to do a forefront neutrino measurement. MicroBooNE is proposed to fill this gap and not only provide realistic technology tests but also accomplish very important neutrino physics measurements in the Fermilab Booster and NuMI Neutrino Beams. The MicroBooNE experiment is a small, focused effort, designed to exploit the advantages of liquid argon detectors to make detailed measurements of neutrino interactions. The major physics goal of MicroBooNE is to address the excess of events at low energies observed by MiniBooNE [1]. In addition, the fine-grained information available with the MicroBooNE detector will allow much improved cross section measurements especially by detecting and measuring all of the outgoing particles (except neutrinos).

The low-energy excess observed by MiniBooNE highlights the fact that most neutrino experiments do not distinguish electrons from single photons, either real direct photons or asymmetrical neutral pion decays. MicroBooNE employs a $\sim$70 ton fiducial volume Liqid Argon Time Projection Chamber (LArTPC), which offers excellent dis-

crimination between photons and electrons and good particle identification in general. The high spatial resolution and energy measurement down to the MeV scale provides information for low and high energy particles that has not been available using high intensity beams. MicroBooNE will run on the surface enclosed in a shielding block hut near the MiniBooNE enclosure. MicroBooNE will be exposed to the Booster Neutrino Beam (BNB) with 6 $\times 10^{20}$ protons on target, as well as to an off-axis component of the NuMI beam. The motivation for this experiment is the physics of neutrino interactions, however, MicroBooNE advances the R&D effort towards massive LArTPCs for long baseline ν_e appearance physics as well.

While MiniBooNE ruled out a two-neutrino interpretation of the LSND result, seeing no excess of events above E_ν=475 MeV, a 96 $\pm 19_{stat} \pm 21_{syst}$ event excess from 300-475 MeV and a 91 $\pm 19_{stat} \pm 25_{stat}$ event excess from 200-300 MeV suggest an as yet unpredicted background, or new physics [2, 3, 4, 5, 6, 7, 8, 9]. In either case, the nature of these events must be understood.

MicroBooNE is ideal for understanding this low energy excess; it detects neutrino interactions with very high efficiency, nearly free from background from misidentified particles, usually the dominant background in this energy region. While the MiniBooNE detector cannot differentiate electrons from photons, MicroBooNE can, even at low energies. This capability reduces the number of misidentified events and, by improving the signal to noise ratio, allows the use of a detector that is about an order of magnitude smaller than MiniBooNE. MicroBooNE's 70 ton fiducial volume is within a 2.5m x 2.5m x 12m drift region of 100 tons active volume. The total mass of the Argon in the detector is 170 tons.

MicroBooNE's sensitivity to the MiniBooNE low energy excess can be determined by scaling from the background and excess "signal" events observed in MiniBooNE. MicroBooNE's efficiency for all ν_e events, the "signal" events and backgrounds from intrinsic beam ν_e events, increases by a factor of two while the backgrounds from misidentified

events are reduced by almost an order of magnitude. Folding in both statistical and systematic errors, the same signal MiniBooNE sees in the 200-475 MeV range corresponds to $53.4 \pm 5.6_{stat} \pm 1.9_{syst}$ events in MicroBooNE.

The capability of MicroBooNE to distinguish photons from electrons is also very useful for study of cross sections which are of interest in their own right and also of interest to future long baseline neutrino experiments. In the (1-2) GeV neutrino range covered by the fluxes of the Booster and NuMI off-axis neutrino beams, MicroBooNE will observe a significant number of neutral current π^0 interactions which are a significant background to long baseline $\nu_\mu \rightarrow \nu_e$ oscillation searches. Furthermore, MicroBooNE will acquire a significant number of charged current ν_e interactions from the off-axis NuMI neutrino beam, which is useful for the careful study of the kinematics and multiplicities of these reactions in the same energy range as the future long baseline experiments.

The extensive development for the ICARUS experiment [10] has given confidence that a large drift chamber with a long drift can indeed be realized and much practical information about the techniques involved has been gained. In parallel, the developments in other LA experiments have demonstrated the practicality of a number of advances in technique, such as the use of electronics mounted on the detector in the liquid argon, and advanced feedthroughs and connections for very large numbers of channels. MicroBooNE's design will take advantage of these developments to allow the fastest possible completion of the experiment, minimize cost, deliver the physics as soon as possible, fit into the beam schedule, and quickly provide a result that we need in the U.S.: a published physics paper on a topical issue derived from a Liquid Argon TPC.

While priority is placed on physics and speed of preparation, MicroBooNE will also provide experience with designs for construction of very large detectors. In particular, the scale and the parameters of drift, noise and resolution performance will give a good basis for the design of the next generation of detectors at a larger scale. MicroBooNE is the necessary next step in a phased program of R&D on LArTPCs for use in future long

baseline experiments.

The importance of this has been recognized by a number of recent committees and reports. The DOE's Neutrino Scientific Assessment Group (NuSAG) report [11] from July 2007 states as one of its four top level recommendations:

> "A phased R&D program with milestones and using a technology suitable for a 50-100 kton detector is recommended for the liquid argon detector option. Upon completion of the existing R&D project to achieve purity sufficient for long drift times, to design low noise electronics, and to qualify materials, construction of a test module that could be exposed to a neutrino beam is recommended."

MicroBooNE fits perfectly into this phased program. Cold electronics will demonstrate "low noise electronics", a large sample of neutrino interactions will be recorded, and in conjunction with the purity testing already underway at Fermilab, LArTPC R&D will advance in the manner that NuSAG advises.

The seven collaborating institutions on MicroBooNE make up a small, focused, and experienced group. This collaboration brings together groups using the BNB and the NuMI beamline as well as groups with extensive technical expertise in LAr detectors and LArTPCs in particular. This benefits both the MicroBooNE experiment and interest in the next stage of LArTPC development.

The experiment is presented in the following order:

- Chapter 2 provides the physics motivation for these measurements;
- Chapter 3 describes the flux, event rates, and beam requirements;
- Chapter 4 details detector design with a strategy to avoid innovations towards construction of an excellent detector within a short time and with minimal cost;

- Chapter 5 examines neutrino interactions in the detector;
- Chapter 6 outlines cost;
- Chapter 7 provides summary and conclusions.

Chapter 2

Motivation

The MicroBooNE experiment is motivated by resolution of the MiniBooNE low energy excess, measurement of neutrino cross sections on Argon, and as a step in a staged program using Liquid Argon TPCs towards the search for CP Violation in the neutrino sector. In addressing the MiniBooNE result, a LArTPC is the ideal detector as it can resolve events at low energies and is capable of e/γ separation. In addition, dedicated measurements of neutrino cross sections are important for next generation neutrino experiments and interesting in their own right. Finally, as a step in a phased program for LArTPC development towards massive detectors, MicroBooNE will teach us a number of things including gaining experience with a running physics experiment maintaining and achieving purity, using cold electronics, reconstructing events in a surface detector, and understanding the costing for large LArTPC detectors. The motivation for MicroBooNE is described in more detail below.

2.1 Addressing the MiniBooNE Low Energy Excess

The recent MiniBooNE results show that the observed data with neutrino energies above 475 MeV is consistent with the expected background and rules out a two-neutrino inter-

pretation of the LSND signal. However for E_ν between 300-475 MeV, a 96 $\pm 19_{stat} \pm 21_{syst}$ event excess is observed. Below this, between 200-300 MeV a 91 $\pm 19_{stat} \pm 25_{syst}$ event excess is observed [12]. In this low energy region the backgrounds from misidentified ν_μs are rising and cannot be resolved by the MiniBooNE detector. Specifically, the MiniBooNE detector is unable to distinguish electrons from photons which make it difficult both to reduce the backgrounds and to interpret the signal. MiniBooNE has not reported data below E_ν=200 MeV. The low energy performance of the MiniBooNE detector makes analysis in this region very difficult.

The MicroBooNE LArTPC is well-suited for the study of the low energy events since it records tracks with good resolution down to several MeV, resulting in a low background for the events of interest.

2.1.1 The Low Energy Excess

The low energy excess observed by MiniBooNE is shown in Figure 2.1 as a function of E_ν^{QE}, the reconstructed neutrino energy assuming these are charged current quasi-elastic events. The excess is significant below $E_\nu^{QE} < 475$ MeV.

In this region, the dominant background is misidentified ν_μ interactions. Table 2.1 shows the breakdown of the different background components for the oscillation analysis region (above 475 MeV) and for the 200-475 MeV region. While the backgrounds contribute equally from intrinsic ν_e and misidentified ν_μ interations at higher energies, the backgrounds from intrinsic ν_es are falling off at the lowest energies while those from misidentified ν_μs continue to rise.

The backgrounds due to misidentified ν_μs over the entire energy range of the analysis are evaluated using MiniBooNE data. For example, the measured rate of neutral current pion (NCπ^0) interactions in MiniBooNE is used to normalize the Monte Carlo to predict the number of NCπ^0 and radiative delta backgrounds ($\Delta \rightarrow N\gamma$). The measured rate

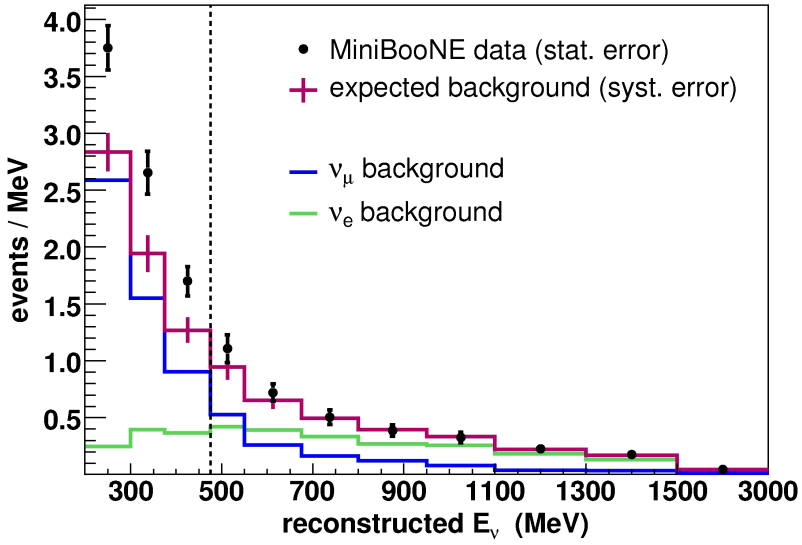

Figure 2.1: MiniBooNE data is consistent with background predictions above 475 MeV, however an excess of events above backgrounds is observed down to 200 MeV.

of ν_μ charged current quasi-elastic scattering is used to re-tune the Monte Carlo to predict the number of other backgrounds including single γ events arising primarily from interactions in the dirt outside the detector. In these so-called dirt interactions, only one γ from primarily NC π^0 enters the detector and converts. The Monte Carlo predictions are set using the measured data. Therefore, uncertainties in the flux and cross sections are tightly constrained.

Two other sources of misidentified events not considered during the oscillation analysis have now been considered but do not comprise a sizable fraction of the excess of events. The first are NC π^0 interactions where one of the secondary γs is absorbed via a photo-nuclear interaction. The size of this background is under study and will be presented at the time of the PAC.

The second is a standard model process that has never been observed: diffractive scattering from a neutrino leading to a photon and a recoil nucleon [8]. This process can have significant effects on neutron-star cooling and supernova evolution. It is an

Table 2.1: Signal and Backgrounds in MiniBooNE

Process	200-300 MeV	300-475 MeV	475-1250 MeV
NC π^0	115	76	62
NC$\Delta \rightarrow N\gamma$	20	51	17
Dirt	99	50	17
Other	24	30	30
Total ν_μ induced	258	207	129
Total ν_e intrinsic	26	67	229
Total Background	284±25	274±21	358±35
Data	375±19	369±19	380±19

important measurement as well it is essential for understanding neutrino experiments. It will be discussed further in Section 8.

MiniBooNE has performed a set of checks that show the events do not look unusual as compared to the rest of the data set. The events are spread evenly in time through the MiniBooNE run, distributed evenly in the detector, and look like ring-like events when viewed using the event display [12].

If the events are electron-like, the distribution of the events in reconstructed neutrino energy is relevant. If these events are not ν_es, the excess in visible energy is more relevant. The excess distributed in visible energy deposited in the detector, consistent with the neutrino energy distribution, is shown in Figure 2.2.

MiniBooNE has also looked for this excess in the sample of neutrino interactions from the off-axis component of the NuMI beam that the MiniBooNE detector samples. Results from this analysis are anticipated by Fall 2007.

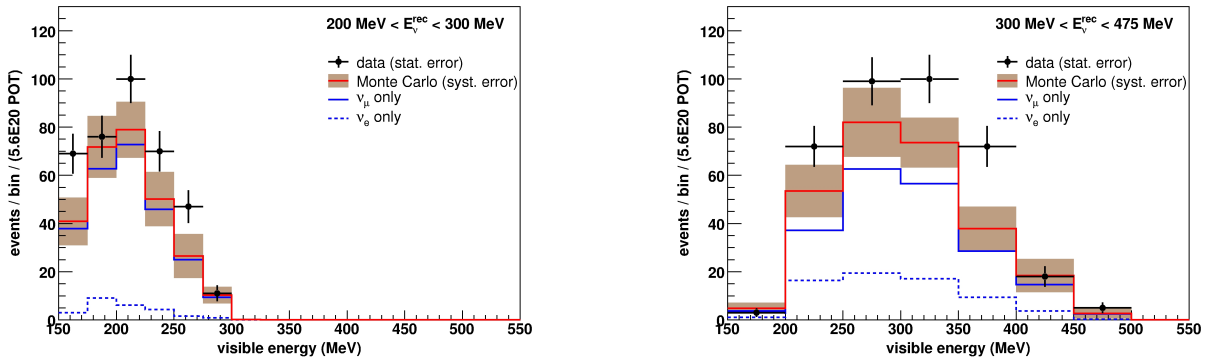

Figure 2.2: Left – Visible Energy of events with E_ν from 200-300 MeV. Right – Visible Energy of events with E_ν from 300-475 MeV.

2.1.2 Interpretation of the Low Energy Excess

The MiniBooNE results were presented in April, 2007, and in the six months which have followed, a number of different interpretations which incorporate beyond-the-Standard-Model physics have been published. It is notable that there is also one model which was published in 2006, which **pre**dicted MiniBooNE would observe no excess in the "signal" region ($>$ 475 MeV), but rather an excess at lower energies. These models, listed below, are described in detail in Appendix 8.

- 3+2 Models using Sterile Neutrinos [2, 3, 13]
- Sterile Neutrinos and Extra Dimensions [4]
- Electron Neutrino Disappearance [5]
- Lorentz Violation [6, 14, 7]
- Neutrino Photon Interactions [**?**, 8]
- Neutrino Decay [9]

2.1.3 Addressing the Low Energy Excess at MicroBooNE

There are a wide variety of interpretations of the MiniBooNE signal. A follow-on to MiniBooNE must not only be able to resolve the events better, but should also be able to go lower in energy to make a more complete meaurement to see if the effect disappears as is expected in some models. The LArTPC technology satisfies both criteria. LArTPCs have a low energy threshold at a few MeV – far below the hundreds of MeV threshold on MiniBooNE, and will therefore be able to resolve the size of the signal at lower energies. MiniBooNE cannot differentiate between electrons and photons. By contrast, MicroBooNE can compare the first few centimeters of electron and photon showers to differentiate between the two. In electron showers, only one minimum ionizing paricle (MIP) deposition is recorded before the shower develops. Photons convert to e^+e^-, depositing two MIPs. These tags will virtually eliminate the backgrounds from misidentified ν_μ events. The backgrounds from intrinsic ν_es are irreducable, but, MicroBooNE will take advantage of the fact that we can predict from Monte Carlo simulation the neutrino event spectrum as well as MiniBooNE has done, using the same analysis tools.

MicroBooNE's sensitivity to the low energy excess can be determined by comparison to MiniBooNE's efficiency for signal events and systematic errors for background events. Table 2.2 lists the signal and backgrounds for MiniBooNE and MicroBooNE. These are listed separately for the 300-475 MeV and 200-300 MeV energy bins. Table 2.3 lists the associated systematic errors and experimental sensitivity. The differences between the MiniBooNE and MicroBooNE signal and errors are described below. Number of events are also scaled for the MicroBooNE tonnage and for run time. The MicroBooNE fiducial volume is $\sim$73 tons and the necessary protons on target is 6×10^{20} total.

Table 2.2: Number of Signal and Background Events in MiniBooNE(mB) and MicroBooNE(μB). Events in MicroBooNE are scaled from the number of events in MiniBooNE. The intrinsic ν_e backgrounds in MicroBooNE are scaled up by a factor of 2 for the increase in detection efficiency and electron identification, and down by a factor of 73/500, the ratio of the fiducial volumes of MicroBooNE/MiniBooNE. The backgrounds from misidentified ν_μs are scaled down by 94% (see Section 5.1.3) because of the $\frac{dE}{dx}$ tag, and down by 73/500 for the change in fiducial volume.

Process	200-300 MeV (mB)	300-475 MeV (mB)	total events (mB)	Scaling factor	total events (μB)
"signal"	91	96	187	0.29	54
Backgrounds from Intrinsic ν_es					
$\nu_e - \mu$	19.2	48	67.2	0.29	19.2
$\nu_e - k^+$	7	14	21	0.29	6.0
$\nu_e - k^0$	2	4	6	0.29	1.7
$\nu_e - \pi$	0	1	1	0.29	0.3
Backgrounds from ν_μ misIDs					
NCπ^0	115	76	191	0.0084	1.6
Dirt	99	50	149	0.0084	1.3
$\Delta \to N\gamma$	20	51	71	0.0084	0.6
Other	24	30	54	0.0084	0.5
Total	286	274	560		31.2

Table 2.3: Number of Signal and Background Events and Uncertainties in MicroBooNE(μB). "Uncertainties from mBooNE" are fractional. Uncertainty in "dE/dx" is described in the text. "Error" gives number of events due to uncertainties.

Process	total events(μB)	Uncertainties from mB	dE/dx unc.	Total unc.	Error
"signal"	54				
$\nu_e - \mu$	19.2	0.075	0	0.075	1.44
$\nu_e - k^+$	6.0	0.16	0	0.16	0.96
$\nu_e - k^0$	1.7	0.3	0	0.3	0.51
$\nu_e - \pi$	0.3	0.33	0	0.33	0.09
NCπ^0	1.6	0.16	0.1	0.53	0.86
Dirt	1.3	0.18	0.1	0.531	0.68
$\Delta \rightarrow N\gamma$	0.6	0.2	0.1	0.54	0.33
Other	0.5	0.18	0.1	0.53	0.25
Total	31.2				1.86
			"signal"	**84.6**	
			Excess	**53.4**	
			Statistical Error	**5.58**	
			Systematic Error	**1.86**	
			Total Error	**5.98**	
			Significance	**9.1**	

Electron Neutrino Efficiency

MiniBooNE's ν_e efficiency within the fiducial volume, folding in pre-cuts and the track based analysis cuts is $< 40\%$. A number of studies have shown that the efficiency for electron neutrino CCQE events within the fiducial volume in LArTPCs is 80% at worst [11, 81]. Therefore, MicroBooNE electron neutrino efficiency is assumed to be $\sim$x2 better than MiniBooNE. This factor is taken into account both for efficiency of the "signal" events and the background intrinsic ν_e events.

With upcoming new results from HARP, the error on the background intrinsics from kaons may improve on MicroBooNE. With MicroBooNE's fine-grained detector, MicroBooNE may be able to improve upon MiniBooNE's determination of the ν_es from muons [1]. Conservatively, it is assumed that MicroBooNE will do only as well as MiniBooNE in determining the error on these intrinsic electron neutrino backgrounds.

Misidentified ν_μs

Misidentified ν_μ interactions are rising at low energies in the MiniBooNE "signal" region. Most of these backgrounds come from γ-like events which cannot be differentiated from electron-like events in MiniBooNE. Specifically, misidentified NCπ^0s arise from asymmetric events where only one photon converts to an e^+e^- shower, and the event looks electron-like. The "dirt" backgrounds on MiniBooNE arise from neutrino interactions outside of the detector which enter the detector without firing the veto. Seventy-five percent of these are NCπ^0 interactions where only one γ sneaks into the detector and converts. Radiative delta decays ($\Delta \rightarrow N\gamma$) again produce only one photon which can appear electron like. For these three classes of events, MicroBooNE will be able to tag the single γ shower and differentiate from an electron with an inefficiency of 6%, as shown in Section 5.1.3. Therefore, these backgrounds on MiniBooNE are reduced by 94% with MicroBooNE. The "Other" backgrounds listed in the table are from a combination of

CCQE events and radiative interactions. Using topology and the Michel tag, MicroBooNE should be able to eliminate many of these events. Conservatively, it is assumed that these will also be reduced by only 94%.

The errors on these backgrounds may improve with the precision of the MicroBooNE detector. Specifically, the uncertainties in light propogation in the MiniBooNE detector, the so-called "optical model errors" which dominate on MiniBooNE will not be present in MicroBooNE. Conservatively, the errors on the backgrounds in MiniBooNE are assumed here with the error on the $\frac{dE}{dx}$ tag, estimated at 10%, folded in.

Sensitivity with Statistical and Systematic Errors

As described in Table 2.3, the predicted background in the energy region from 200-475 MeV is 31.2 events with a systematic uncertainty of 1.9 events. Scaling from the MiniBooNE excess assuming the excess events are electron-like, one would expect an excess in MicroBooNE of 53.4 events. So, the total expected events, excess plus background, is 84.6 events.

The probability that the predicted background would fluctuate up to an observed 84.6 events can be calculated from the level of the excess divided by the total error in the predicted background, $\sigma_{total} = \sqrt{31.2 + 1.9^2} = 5.9$. The 53.4 excess would then correspond to a $53.4/5.9 = 9.1\sigma$ effect.

Treated as a signal, the excess would correspond to a measured signal of $53.4 \pm 9.2_{stat} \pm 1.0_{syst}$. With MicroBoone's high detection and measurement efficiency, the angular and energy dependence of the excess signal will also give important information on the interpretation of these anomalous events.

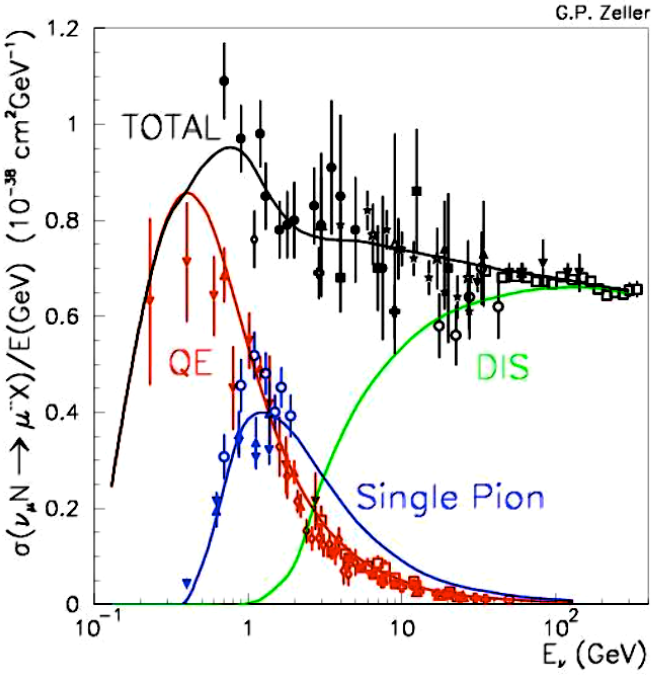

Figure 2.3: Compilation of previous measurements of charged-current quasielastic, deep inelastic, and single pion production, taken from [15].

2.2 Cross Section Measurements

Neutrino cross sections are of interest in their own right and precision measurements are required for these rates in the $(0-2)$ GeV region (see Figure 2.3). Exposure of the MicroBooNE experiment, which has very low detection threshold, to both the BNB and NuMI beams, could significantly improve our knowledge in this interesting region. Figure 2.3 summarizes much of the world's data for neutrino cross sections. As the statistics accumulated at long baseline experiments improves, the need for precision measurements grows, both in terms of modelling signal processes, and for studies of background rejection. While there are a variety of topics that could be addressed, we discuss here just a few for which MicroBooNE could add some unique information.

As can be seen in Figure 2.3, the quasielastic process $\nu_\mu p \rightarrow \mu^- n$, has a strong peak

at 500 MeV and dominates the charged-current cross section for $E_\nu < 1$ GeV. Cherenkov detectors such as MiniBooNE, T2K and Super-K rely on such interactions for accurate reconstruction of the neutrino energies, and all neutrino experiments have relied on the quasielastic cross section for detailed studies of their neutrino flux due to the theoretical reliability of the cross section calculation. The cross section in momentum transfer q^2 can be written in terms of nucleon form factors[16]

$$\langle N'|J_\mu|N\rangle = \overline{u}(N')\left[\gamma_\mu F_V'(q^2) + \frac{i\sigma_{\mu\nu}q^\nu \xi F_V^2(q^2)}{2M} + \gamma_5\gamma_\mu F_A(q^2)\right]u(N),$$

where the vector form factor $F_V(q^2)$ has been well-measured in electron-nucleon scattering [17], and the axial form factor $F_A(q^2)$ must be measured in neutrino scattering experiments. When expressed as a dipole form factor, $F_A(q^2) = g_A/(1+(q/M_A)^2)^2$, is parameterized by the effective axial mass M_A. Of interest, the world-average [18] for this parameter prior to 2002, $M_A = 1.03 \pm 0.02$ GeV, is in moderate disagreement with recent measurements from K2K [19], 1.20±0.12 GeV, and MiniBooNE [20], 1.25±0.12 GeV. While MINERvA will make excellent measurements of the QE cross section above 1-2 GeV, it would be desirable to have measurements in the $E_\nu < 1$ GeV region. The low energy threshold and excellent track reconstruction possible in the LArTPC should provide for very good measurements in MicroBoone. Approximately 30,000 events could be recorded from the NuMI beam, and approximately 40,000 events from the BNB.

Single pion production is also of particular interest. As seen in Figure 2.3, it begins to dominate the cross section channels at the $E_\nu \sim (1-2)$ GeV region of interest to long-baseline experiments like NOvA and T2K in order to properly model neutrino showers in the NOvA detector. For T2K, such single pion data is valuable because the CC single pion reaction is a background to the CC QE events used in the disappearance analysis for oscillations and measurement of Δm^2_{23} and $\sin^2(2\theta_{23})$. Measurements are now available on charged-current single pion production from K2K and MiniBooNE, and should be available as well from the MINERvA experiment.

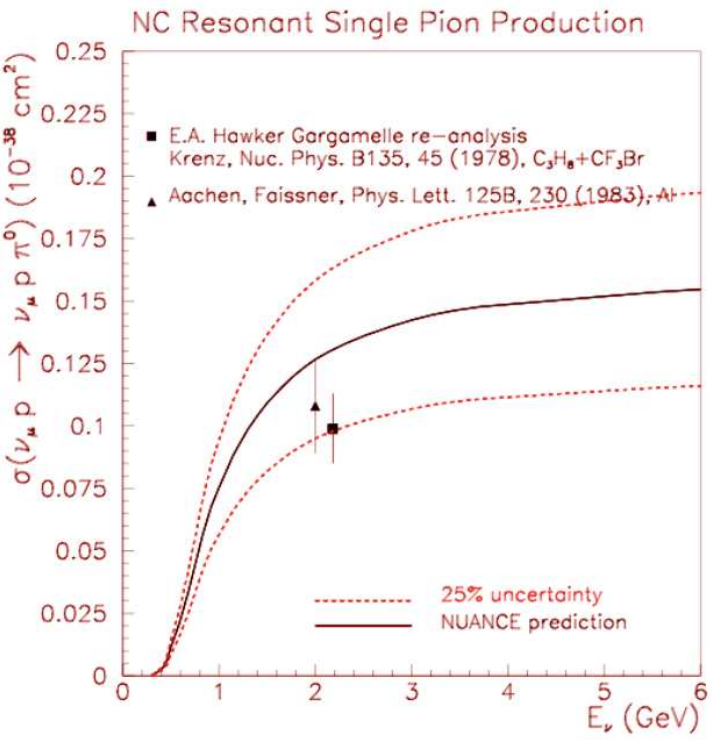

Figure 2.4: Compilation of previous measurements of neutral-current π^0 production, taken from [15]. A more recent measurement from K2K [21] is not plotted, but corresponds to $\sigma \sim 0.048 \times 10^{-38}$ cm^2 at $\langle E_\nu \rangle$ ~1.5 GeV.

The corresponding single pion cross section for NC π^0 production, namely $\nu_\mu + N \rightarrow \nu_\mu + N + \pi^0$, where the neutral pion might be produced, for example, through a resonance excitation, is rather poorly measured (see Figure 2.4). Such NC π^0 production is of interest in $\nu_\mu \rightarrow \nu_e$ oscillation searches because of the electromagnetic energy deposited in neutrino detectors which can mimic an electron shower(see Section 2.3). To date, only a couple measurements exist for this process [15]. Recently, K2K [21] has measured $\sigma(NC\pi^0)/\sigma(CC) = 0.064 \pm 0.07$ at $\langle E_\nu \rangle$ ~1.5 GeV. MiniBooNE has measured, furthermore, that approximately 18% of NC π^0 production happens through coherent scattering off the entire nucleus [22]. While MINERvA will have excellent π^0 detection for an NC π^0, it will be in the wide-band NuMI on-axis beam, with a less well-defined energy $\langle E_\nu \rangle$ at the NC scattering took place. For oscillation searches, it would be advan-

tageous to measure this cross section at approximately (1-2) GeV. MicroBooNE should record ∼8,000 NC π^0 events from the BNB ($\langle E_\nu \rangle \sim 0.8$ GeV), and approximately 1750 events from the NuMI off-axis beam.

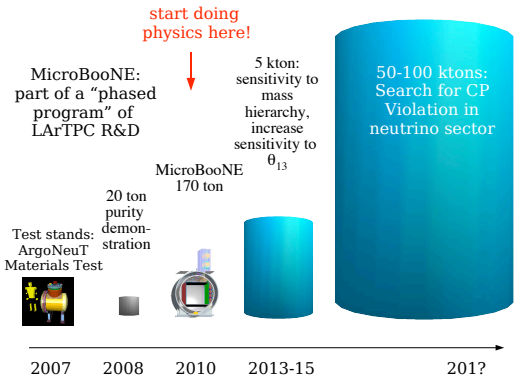

Figure 2.5: MicroBooNE is part of a staged program for scaling LArTPCs to the 50-100kton size necessary for CP Violation searches. As ArgoNeuT serves as a test bed for MicroBooNE, MicroBooNE serves as a test bed for the 5kton detector.

2.3 Synergy with Long Baseline Oscillation Experiments

Liquid Argon TPCs are ideal detectors for long baseline ν_e appearance physics because of their high efficiency for ν_e "signal" events and low backgrounds from misidentified ν_μs. However, very large detectors are needed to mitigate the low statistics of these experiments. As recommended by the NuSAG committee, a "phased R&D program with milestones and using a technology suitable for a 50-100kton detector" is necessary for LArTPC detector technology.

MicroBooNE fits perfectly in this phased program both in collecting neutrino interactions to do "Physics R&D" and in advancing the technology in hardware R&D.

2.3.1 LArTPC Physics R&D

By collecting a large class of neutrino interactions at low neutrino energy MicroBooNE will both develop tools for measuring, simulating, and reconstructing neutrino interac-

tions, and perform cross section measurements. These cross section measurements are important not only for the next step in LArTPC detectors, but also for the existing program, including the NOvA experiment.

Physics Tools for LArTPCs

MicroBooNE will produce the first published physics result from a LArTPC experiment. Along with this, tools will be developed to fully simulated the detector and reconstruct events in the detector. While there has been extensive work with LArTPCs over the last several decades, no fully automated reconstruction program for LArTPC detectors has been implemented. Developing this is an important step towards massive LArTPCs. Finally, reconstrucing events in a background of cosmic rays present in a surface detector must be understood if next generation massive LArTPCs are to be cited on the surface. The MicroBooNE data set will provide the sample to test cosmic ray rejection.

Cross Section Measurements for NOνA and Beyond

Fermilab, through the NOvA experiment and possible extensions using Liquid Argon TPC's, will study $\nu_\mu \rightarrow \nu_e$ oscillations beginning in 2012. The program will make use of the NuMI beam, operated in the "Medium Energy" Configuration, and will be situated approximately 14 mrad off the central axis of the beam so as to soften the neutrino spectrum (see Figure 2.6). The softened spectrum in the off-axis beam peaks at $E_\nu \sim$ 1.9 GeV, which may be compared to the maximum oscillation probability occuring at 1.8 GeV for $\Delta m^2_{23} = 2.5 \times 10^{-3}$ eV^2 and the NOvA experiment baseline of 810 km. As can be seen in Figure 2.6, the appearance of ν_e in the ν_μ beam occurs with highest event rate just above the energy corresponding to the maximum oscillation probability, due to the rising CC ν_e cross section. In addition, the NOvA experiment will improve the measurement of Δm^2_{23} through the "disappearance" of charged-current ν_μ interactions at the Far Detector.

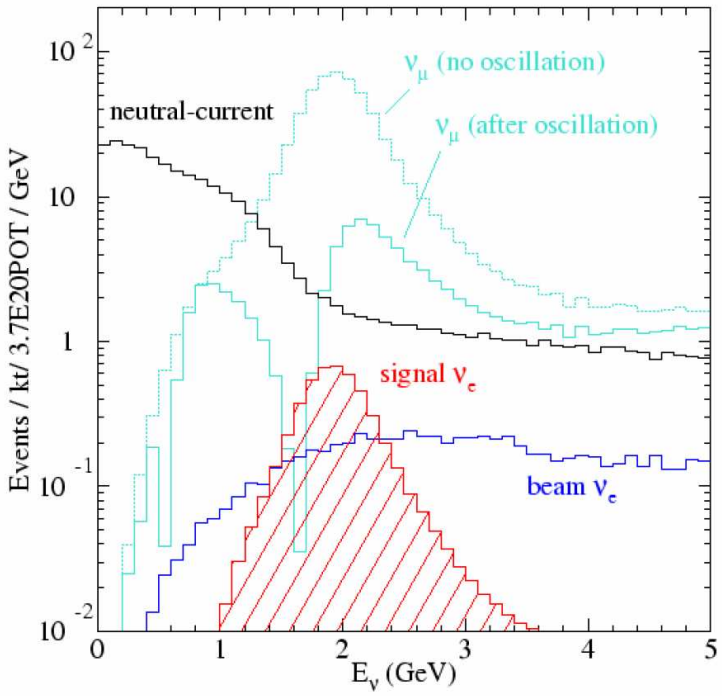

Figure 2.6: Visible energy distribution of events expected at the NOvA Far Detector in Ash River, MN. Shown are the total event rates expected from charged-current ν_μ, neutral-current $\nu_\mu + \nu_\tau$, charged-current ν_e from intrinsic ν_e in the beam, and charged-current ν_e expected from oscillations if $\sin^2(\theta_{13}) = 0.1$.

The NOvA experiment faces several backgrounds for the search for ν_e appearance in a ν_μ beam. First, there is a contamination of $\sim 1\%$ ν_e flux in the NuMI beam due primarily to $\pi \rightarrow \mu \rightarrow e\nu_e\nu_\mu$ decays as well as $K \rightarrow \pi e\nu_e$ decays. This intrinsic ν_e content in the beam (ν_e's not arising from oscillations) are fortunately spread out in energy, unlike the strongly peaking ν_e which might arise from oscillations.

NOvA also faces backgrounds from Neutral Current (NC) interactions of ν_μ which can be misidentified as charged current ν_e interactions. Processes such as $\nu_\mu + N \rightarrow \nu_\mu + \pi^0 X$ leave an electromagnetic shower from the $\pi^0 \rightarrow \gamma\gamma$ decay, as well as a hadronic shower X from the breakup of the nucleus N. Such a signature can mimic a CC ν_e interaction if the two photons in the π^0 decay are not resolved. Such NC interactions do not deposit the

full neutrino energy in the NOvA detector, so neutrinos of all energies above the energy of interest can contribute to the region of low visible energy where the oscillation signal might be observed. As can be seen in Figure 2.6, the NC interactions will exceed the oscillation signal, even if the most optimistic value for $\sin^2(2\theta_{13})$ is observed. Therefore, detailed understanding of this background, and a rejection of over 99% is usually required.

The MicroBooNE experiment could significantly improve our understanding of NC interaction rates, as well as assist in separating NC and CC-ν_e topologies, at the critical $\langle E_\nu \rangle \sim 2$ GeV region. As seen in Figure 3.3, the NuMI beam at ~ 110 mrad off-axis angle produces a prominent peak at 2 GeV from kaon decays [23], thus providing an ample source of NC π^0 interactions from such neutrinos. Furthermore, the off-axis beam produces a reasonable signal of 1-2 GeV ν_e's, so the experiment can hope to perform detailed studies of CC ν_e interactions. With the superior imaging capabilities of the LAr detector, one could hope to obtain clean separation of these two event categories, rather than just make a statistical statement. Indeed, a ν_μ and ν_e signal were already extracted from the NuMI off-axis beam using the MiniBooNE experiment [24].

With such samples from the NuMI off-axis beam, detailed kinematical information can be reconstructed for both of these topologies which would be quite valuable in tuning Monte Carlos for the NOvA experiment. A Monte Carlo study [25] of NC and ν_e separation in a Liquid Argon detector has already been made as part of the FNAL-BNL long-baseline study. In this study, it was found that NC events could be rejected with $99 \pm 1\%$ efficiency from a ν_e search. It was also found that the efficiency for finding ν_e CC interactions from oscillations (thus at $\langle E_\nu \rangle \sim$2 GeV) was approximately 81%, which is quite good when compared to the reconstruction efficiency of either the MINOS or NOvA detectors ($\sim$40% within the fiducial volume).

These cross section measurements will not only benefit the NOvA experimentm but also LArTPC experiments beyond NOvA. Measuring how well NCπ^0 and single γ rejection matches predictions in LArTPCs will help to validate sensitivity of future experi-

ments.

The ability of the MicroBooNE experiment to provide such useful information for the long baseline neutrino program was seen by the Fermilab Steering Group as a central motivation for the LArTPC R&D program [26].

2.3.2 LArTPC Hardware R& D

The phased program shown in Figure 2.3 begins with a series of ongoing small tests that build build on experience from smaller TPCs such as a prototype TPC constructed and operated in Fleming's lab at Yale. In April 2007, first cosmic ray tracks were observed in this small prototype [27]. These are the first tracks ever observed in a LArTPC in the US. Figure 2.7 shows the readout of one of these events.

The next phase in this program includes the ArgoNeuT project [28], and the Materials Test Stand [29] program at Fermilab. Beyond this, a 20 ton purity demonstration test, combined with what we learn from MicroBooNE will walk us towards the next step, a 5kton device for long baseline physics with larger devices beyond this.

In particular, the ArgoNeuT project will serve as a test bed for the MicroBooNE project both in testing hardware and developing tools to analyze neutrino interactions on Argon. In this same way, MicroBooNE serves as a test bed for the next generation device. With MicroBooNE, we will gain experience:

- Achieving and maintaining purity in a large vessel
- Implementing cold electronics
- Collecting a large sample of neutrino interactions at low energies
- Designing, constructing, and installing wire chambers, feedthroughs, PMTs, etc.
- Studying the effects of cosmic ray backgrounds for a surface detector.

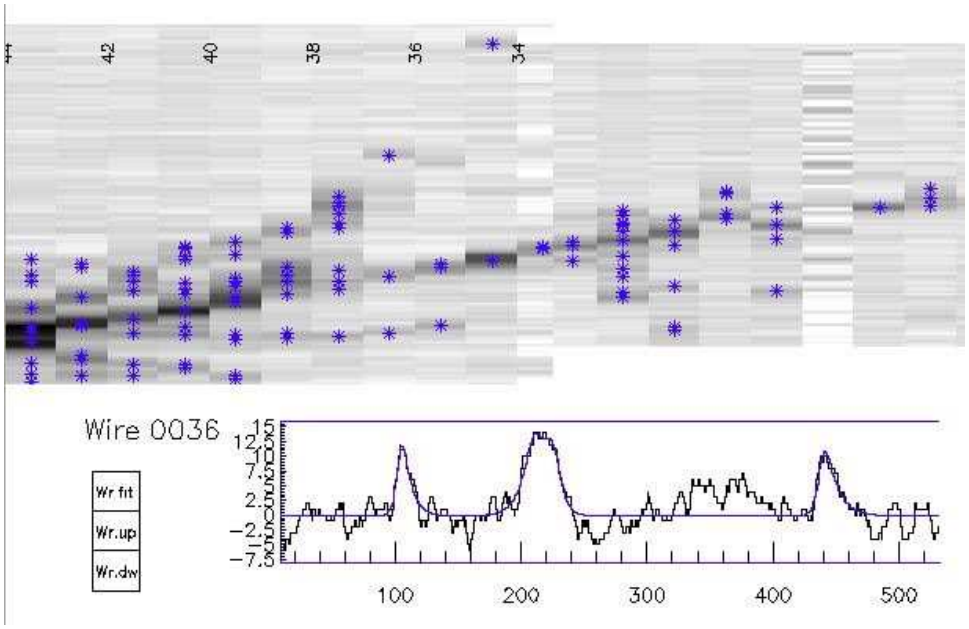

Figure 2.7: Readout of a cosmic ray event in a small prototype at Yale. This is the first LArTPC in the US to see cosmic ray tracks.

While these advances are important steps for scaling the technology to massive detectors, as R&D, they do not endanger the success of the experiment. Rather, MicroBooNE will teach us how to make the next step in scaling the detectors towards long baseline physics, but with a design that ensures the physics goals of the experiment are met.

Chapter 3

The Neutrino Beams

MicroBooNE will be exposed to both the Booster Neutrino Beam (BNB) and the Neutrinos at the Main Injector (NuMI) beamlines. The MicroBooNE detector will be located near the MiniBooNE detector, and the distance from the BNB target to MicroBooNE will be about 450 m, as shown in Figure 3.1.

At present there are no plans to significantly change the design of the BNB beamline. Therefore, the physics discussion presented in this proposal assumes the BNB neutrino-mode neutrino flux, with the 50 m decay line configuration. Running of this beam line in the post-2010 era was endorsed by the Fermilab Steering Group [26].

MicroBooNE will also see events from the NuMI beamline. The analysis of NuMI events in the MiniBooNE beam is underway, and results are expected in late autumn, 2007. The discussion in this proposal is based on preliminary results on the ν_μ flux from NuMI [30]. We plan to update the MicroBooNE proposal to include the NuMI beam expectations in an addendum which will be presented at the spring, 2008 PAC.

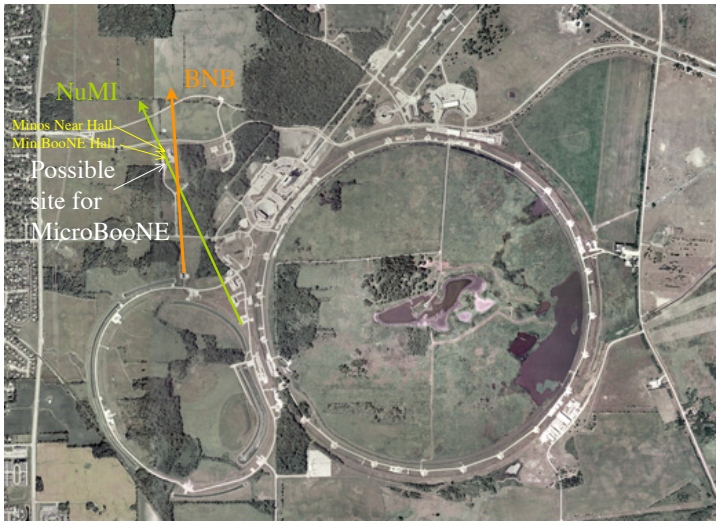

Figure 3.1: Schematic of the location of the MicroBooNE detector on site. MicroBooNE will be located right next to MiniBooNE, exposed to the on-axis BNB and an off-axis component of the NuMI beam.

3.1 The Booster Neutrino Beam

MicroBooNE has developed this request for proton delivery in consultation with the Fermilab Booster Department [31]. We request a base goal of 2×10^{20} protons per year and a stretch goal of 3×10^{20} protons per year delivered to the BNB line from from 2010 to 2012. Our total request is for 6×10^{20} POT.

The BNB is produced via 8 GeV protons impinging on a Be target. A magnetic focussing horn will be run in the polarity which focusses π^+ and K^+ mesons toward the detector. The decay line can have a length of 25 or 50 m. We propose that the line be run with the 50 m decay length. MicroBooNE proposes no changes to the existing design. We see only two issues to note: the spare horn and the spare target.

MicroBooNE requests that a spare horn be available at the start of the 2010 run. The first horn in the BNB line reached 1 million pulses over 3 years before failing. The flaw was understood and corrected for the present horn, which has now exceed 1 million pulses. There is no way to estimate the expected lifetime for this horn. One spare horn has been constructed and tested. Most likely, between now and 2010, the present horn will reach its lifetime and be replaced by the spare. Thus it is likely that we will need at least one more horn. We would prefer to run with Be target slugs which are identical to MiniBooNE running.

Substantial effort is going into a precise understanding of this neutrino beam. Results from the HARP experiment on secondary meson production on replicas of the MiniBooNE target slugs have been published [32] and incorporated into the beam Monte Carlo. Further HARP analysis is under way. MicroBooNE directly benefits from this work if the beam design remains unchanged.

To date, the Be targets have been provided by LANL. There is one existing spare target. The system is designed to allow targets to be removed and re-used if a horn breaks. The first target was not removed from the first horn before storage for simplicity.

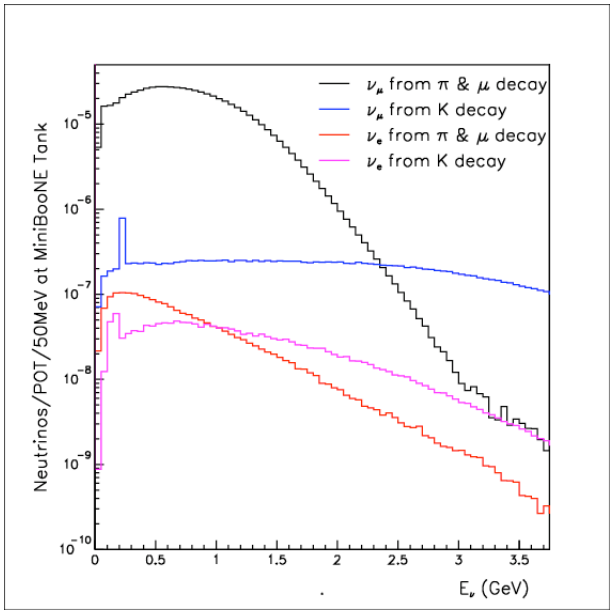

Figure 3.2: The contributions from pion and kaon production to the total predicted ν_μ flux in the MiniBooNE experiment. [1]

By 2010, this first horn, which is stored in the Target Service Building, will be cool enough that this target could be salvaged. The plan is to salvage the target for the second horn, prior to storing the horn when it needs to be replaced.

This proposal makes use of the GEANT-based Monte Carlo flux as well as the flux errors provided by the MiniBooNE Collaboration [33]. The flavor, energy and angle of neutrinos at the MiniBooNE detector site are simulated. The BNB neutrino beam is dominated by ν_μ from π^+ decays up to 2.2 GeV. Beyond this, the neutrinos from K^+ decay are the majority contribution. Fig. 3.2 shows the contributions of pion and kaon decays to the ν_μ flux in the MiniBooNE experiment, which uses an 8 GeV primary proton beam. The spikes at low energy in the K-produced fluxes are due to decays of stopped kaons in the beam dump. The average ν_μ flux energy is about 700 MeV.

Electron neutrinos are produced in the beam through through the $\pi \rightarrow \mu \rightarrow \nu_e$ decay chain and $K \rightarrow \pi\nu_e e$ ("Ke3") decay. The ν_e energy distribution is well constrained by measurements of related ν_μ events in the MiniBooNE detector.

Source	Fractions of BNB Beam Neutrino Flux
$\pi^+ \rightarrow \nu_\mu$	95.3 % of total ν_μ
$K^+ \rightarrow \nu_\mu$	2.8 % of total ν_μ
Antineutrino content	6% of total flux
ν_e and $\bar{\nu}_e$ content	0.5% of total flux
$\mu^+ \rightarrow e^+ \bar{\nu}_\mu \nu_e$	52% of total $\nu_e + \bar{\nu}_e$
$K^+ \rightarrow e^+ \bar{\pi}^0 \nu_e$	29% of total $\nu_e + \bar{\nu}_e$
$K^0 \rightarrow e^+ \bar{\pi}(\nu_e or \bar{\nu}_e)$	14% of total $\nu_e + \bar{\nu}_e$
All other sources of ν_e and $\bar{\nu}_e$	5% of total $\nu_e + \bar{\nu}_e$

Table 3.1: Summary of the BNB Neutrino Flux [34]

The neutrino beam content is summarized in Tab. 3.1.

3.2 The NuMI Beam

The NuMI beam provides an excellent source of off-axis neutrinos for MicroBooNE. If the MicroBooNE detector is situated near the MiniBooNE hall, it would be approximately 110 mrad from the NuMI target. If it were located in the MINOS surface building, it would be at a slightly smaller angle of 108 mrad, much like the NOvA "Intermediate Prototype Near Detector (IPND)." Simulations of the fluxes at the MiniBooNE detector site from the NuMI "Low-Energy Configuration," for example, are shown in Figure 3.3.

As can be seen the off-axis NuMI beam provides two narrow peaks at ∼0.25 GeV and ∼1.9 GeV, from pion and kaon decays, respectively. As is well-known [23], the peaks in the off-axis beam arise because essentially every pion, regardless of its energy, decays to the same energy neutrino when the beam is viewed at a large angle. As a result of the neutrino energy being insensitive to the parent hadron energy, the beam is in a narrow-band.

The expected spectrum from the narrow-band off-axis beam is relatively easy to calculate. Indeed, the large uncertainties typically encountered in calculating the flux from a wide-band beam are reduced to "scale factors" for the overall pion and kaon yields off the meson production target. Figure 3.3 provides an example based upon existing data. The calculation of the flux from the NuMI beam MC uses a calculation of particle yields off the target from the Fluka [35] code, and these particles are then tracked through the NuMI beam MC. For the MINOS experiment, this flux calculation was seen to under- or over-estimate the data by 10-40%, depending upon the neutrino energy and NuMI beam configuration [36]. Only by running the NuMI beam in a variety of configurations (target position and horn currents) was it possible to obtain effective (x_F, p_T) of hadrons in order to describe the MINOS data. The effect of these kinematical fits, however, results only in scale factor adjustments to the pion and kaon peaks in Figure 3.3.

Assuming a 70 ton fiducial volume for MicroBooNE, and a $4{\times}10^{20}$ POT/year exposure to the NuMI beam, we would expect approximately $21,000$ CC ν_μ events, $7,000$ NC events, and approximately 1700 CC ν_e events each year of operation in the low energy beam configuration. These rate expectations have already been validated using data acquired by the MiniBooNE [24] experiment,[1] which is also exposed to the off-axis NuMI beam, as seen in Figure 3.4

[1]The MiniBooNE data underscore the need for a "muon catcher" or range stack for MicroBooNE.

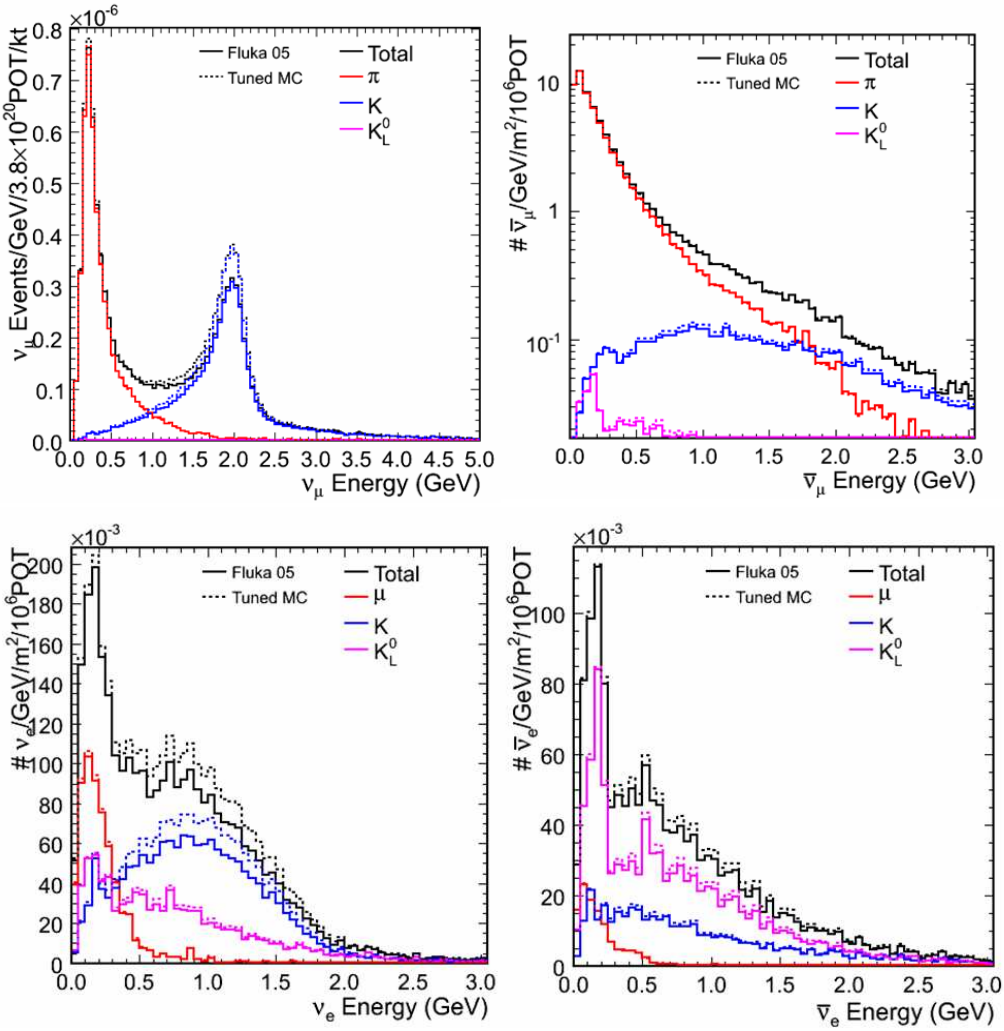

Figure 3.3: Calculated event rates of ν_μ, $\overline{\nu}_\mu$, ν_e, and $\overline{\nu}_e$ from the NuMI beam when operated in the "Low Energy" Configuration at the location of the MiniBooNE detector hall. The contributions from $\pi^\pm$, $K^\pm$, $\mu^\pm$, and K_L decays are indicated. The solid lines are calculated using the yields of particles off the NuMI target as simulated by the Fluka2005 [35] code. The dashed lines use the fit to target particle yields which were derived using the MINOS data [36]. Fluxes have been multiplied by cross-sections from `NUANCE` [37].

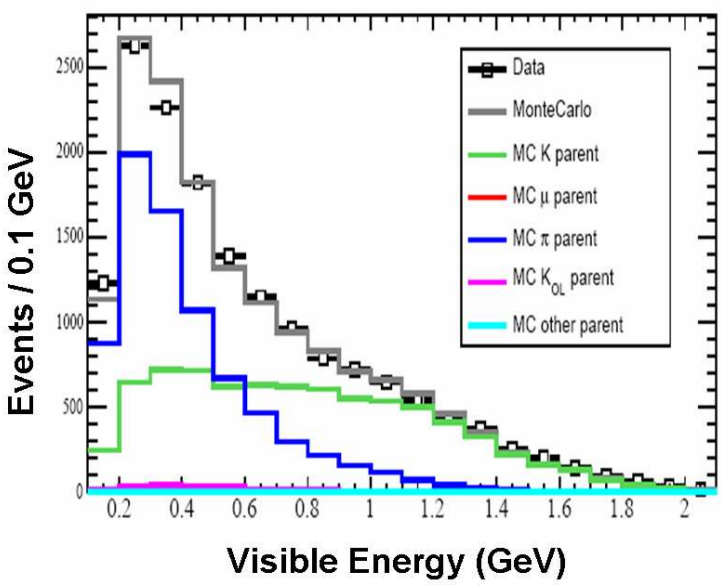

Figure 3.4: Data/Monte Carlo comparison of energy spectrum of CC ν_μ interactions in the MiniBooNE Detector from the NuMI beam [24]. The relative contributions from pion, charged and neutral kaons is shown. Because of the finite size of MiniBooNE, some muons from very high energy neutrinos escape their detector, but the pion and kaon contributions can be seen clearly.

Chapter 4

The MicroBooNE Detector

4.1 Overview of the Detector

A LArTPC detector is well suited for identifying and measuring the properties of neutrino interactions and rejecting background events. The proposed detector will give uniform imaging with good spatial resolution and will measure $\frac{dE}{dx}$ over a large volume. For these reasons this technology was selected to investigate the anomalous result observed in the MiniBooNE experiment.

LArTPC technology has been under development for many years [40]. The operation principle is that in pure LAr the ionization produced can be transported along uniform electric field lines over many meters. The diffusion of the charge is small and thus preserves the spatial accuracy of the track. The charge can be measured using various techniques. In our case we will measure the charge using three planes of wires that will continuously sense and record the signals induced by drifting electrons.

Figure 4.1 shows a cross section of the proposed detector. The main components of the detector are:

- Cryostat and Cryogenics system:

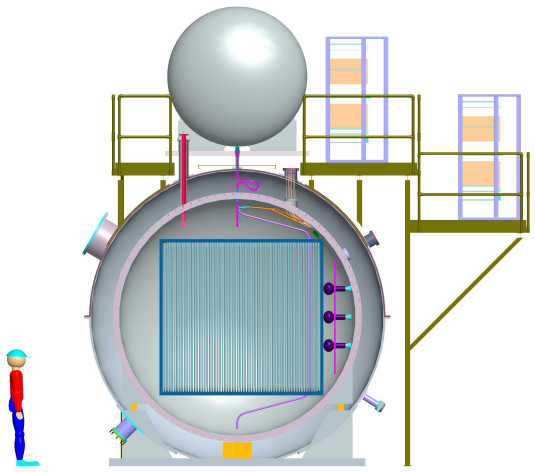

Figure 4.1: Cross section of the detector. The main components shown are the expansion vessel, cryostat, feed-throughs, on-detector electronics, wire chambers and field cage, pmts, and cold electronics location.

  - Large cryostat with a inner diameter of ∼4 m and a length of 12 m. The cryostat needs to be well insulated to minimize heat loss and allow for stable operation of the detector.
  - Cryogenics system – to keep the detector cold and stable.
  - Purification system – to keep the LAr pure enough to allow for a long drift and minimize recombination.

- Detectors: The active detector is composed of a HV "cage" that generates a uniform field of 500 V/cm along the drift direction, giving an electron drift velocity of about 1.6 mm/μs. The electrons are read on large area wire chambers that give Y, U and V projections. The timing information allows us to measure the X direction and the reconstruction of the signals on the wires give the YZ coordinates.

- Cold electronics:

  - To maximize the signal-to-noise ratio we chose to use pre-amps located in the cold as close as possible to the readout wires.
  - In addition to the preamps, there are HV decoupling capacitors to compensate for the fact that the sense wires are at HV.

- Feedthroughs:
  - The signals, calibration lines, PA power, HV bias for the chambers and monitoring lines are all channeled through Hermetic feethroughs that allow signals to come out from the cryostat and the supply of High Voltage (HV) and power the inside.
  - The HV for the field cage is channeled through a special feed-through.

- On detector electronics: These digitize the signals and do the initial analysis. The DAQ does the event building and prepares the data for off line analysis.

- Photo-multiplier tubes(PMTs): An array of PMTs located in the lunes of the detector reduce background by providing a T_0 for events.

There are several key systems which deserve special attention. The critical issues to address are:

- Cryostat and feed-through: The temperature stability and the cleanliness needed for the long drift distances in LAr means that the cryogenics system and feed-throughs need to be designed with great care to allow for stable operation of the detector.

- LAr purification: To achieve the required purity it is important to monitor the materials that come in contact with the liquid, ensure a hermetic system with no leaks, and maintain an active purification system that continuously purifies the liquid.

- TPC construction: The wire construction has a number of challenges not the least of which is the large size of the detector.

- Cold electronics and readout: The signal-to-noise ratio we aim for is quite ambitious and the ∼10K channels of cold electronics and readout needs to have a very high reliability.

In the following we describe in some detail the proposed construction of the experiment. The cryostat, cryogenics, feed-through and purification system are described in Section 4.2. The LArTPC system that is composed of the HV cage and the large wire readout system is given in Sections 4.3.3 and 4.3.4, respectively. The photomultiplier system is described in Section 4.3.6. In section 4.4 we discuss the readout architecture including: mapping and cabling of the detector, cold electronics, and on-detector electronics. In section 4.4.9 the DAQ system is discussed.

4.2 Cryostat and Cryogenics

The Cryostat, feed-throughs, cryogenics and vacuum systems are designed to keep the LArTPC at a constant and stable temperature and keep the LAr pure to allow LAr ionization to have a long enough lifetime. In the following section we describe the conceptual design of the systems.

4.2.1 Detector Cryostat

The LAr cryostat is composed of cold and warm vessels. The vessel's flanges on one end are welded shut and at the other end the flange is bolted. There are a series of feed-throughs along the top of the cryostat to allow for signal, calibration, and high voltage connections between the detector, immersed in LAr, and the external data acquisition electronics and power supplies. In Fig 4.2 we show an end view of the cryostat with the warm flange removed.

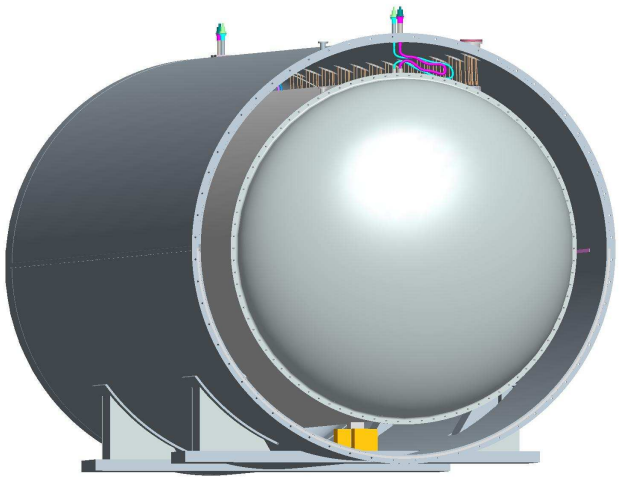

Figure 4.2: View of the cryostat with the warm flange removed.

Cold Vessel (CV)

The 304 Stainless Steel (SS) cold vessel design and its construction will equal or exceed ASME Boiler & Pressure Vessel Code requirements. The CV is classified as an internally pressurized but one of low total internal energy. It has an outside diameter of 3.8 m and a cylindrical length of 13.2 meters including the length of its dished ends. To meet the usual safety factor of 4, the required the wall thickness is less than 25 mm. The cold vessel's internal volume is 125 cubic meters (175 metric tons of LAr) of which 70 cubic meters is the active fiducial volume. CV weight is 37 metric tons.

Warm Vessel (WV)

The warm vessel is an externally pressurized vacuum vessel limited to less than a 15 psi differential pressure and, as such, does not have to meet Code requirements, although FNAL standards say that the design should be according to appropriate rules in the Code revision at time of design. Unlike the cold vessel, the WV will be made of 836 steel, having an outside diameter of 4.72 m and an overall length of 13.47 meters giving ample room to maneuver in the connection space between the cold and warm vessel. Two large 1 meter diameter clapper type safety relief valves are welded through the warm cylinder wall. These large valves vent gas and liquid, keeping the pressure to 1 atm. in case of a dump of cold vessel contents into the vacuum tank space. The weight of the WV is 46 metric tons.

Cold Vessel Support

Because the wall of the cold vessel is thick and its L/D ratio is $\sim$3, it is very stiff. Calculations show that when fully loaded with 175 tons of LAr plus its own weight of 46 tons, the maximum axial sag of the vessel between its supports is 7 mm. Four triangular shaped support pieces are welded to the CV cylinder at both ends to provide load bearing

surfaces. At these positions in the warm vessel the cylinder is cut away to make room for stands that receive the load of the cold vessel and transfer it directly to ground through a thick load distribution plate. The stands are enclosed into the vacuum space by welded face plates. Between the load bearing surfaces are stationary bearing blocks of Ultem plastic, each 150x100x100 mm. Each support is loaded to a maximum of 55 tons stressing the plastic to 34 MPa complying with a Code safety factor of 4. The CV is held in both axial and lateral directions at one end while the other end is free to contract 25 mm axially but guided laterally to keep the centerline alignment of the detector. Sliding shear forces are reduced by low friction DU material between the plastic and cold vessel sliding surfaces.

Assembly of the Cryostat

The design of the entire system has been carried out with ease of assembly being a major requirement. The cold and warm vessel can be looked at as separate subsystems where construction work can go on in parallel with the two coming together for completion. In this case, this feature is advantageous because the CV together with the fiducial box, its electronics, wiring, etc. can be manufactured, installed, tested, and closed in a clean room environment. Then, forty layers of super-insulation are applied to all exposed outer CV surfaces. In parallel, the warm vessel is manufactured split along its horizontal centerline. Figure 4.3 shown below is an exploded view of the major cryostat parts to be assembled. The bottom half of the WV is put into position and anchored. The CV is positioned in the warm vessel lower half on its four load bearing/insulating surfaces. At one end, X lateral stops are bolted in place. At the other end X Y stops are installed. Many signal and instrumentation leads are connected to the CV feed-throughs along with cryogenic flex hoses. The warm vessel top half is put in place and prepared lips are seam welded along the entire vessel length, both sides, and around the circumferential end dished heads. Data, instrumentation and cryogenic lines are connected to the vacuum

side of WV conflat flanges. Conflats are closed after which pump down of the warm vessel commences in preparation for WV leak checking. If the cryostat has to be opened the lip seal can be ground off. The lip length is large enough for a series of three openings and closures.

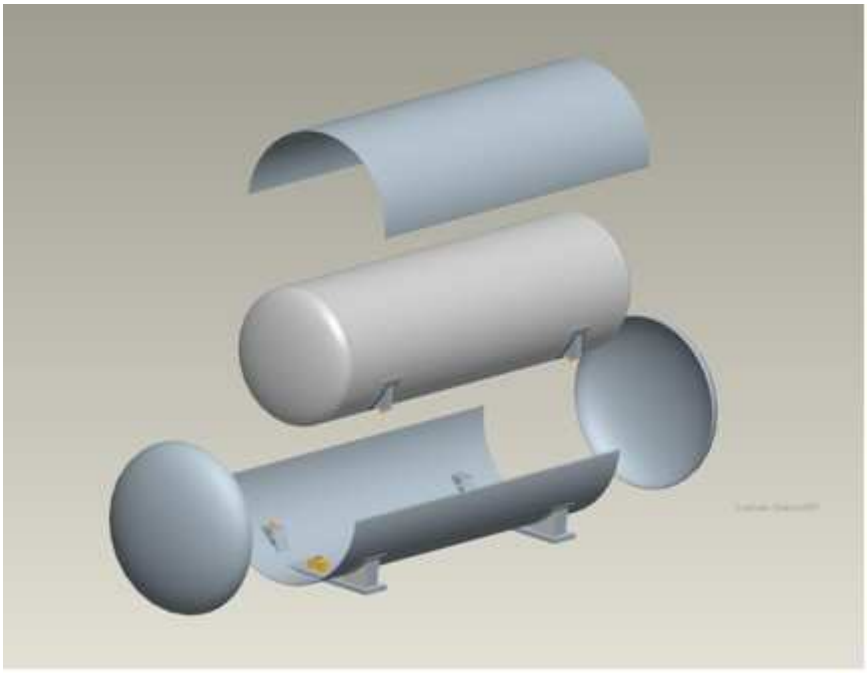

Figure 4.3: Exploded view of the warm, cold vessel and their support.

4.2.2 Cryogenics

The cryogenic system is designed to keep the LArTPC at a constant and stable temperature and keep the LAr pure so as to allow the ionization to have a long enough lifetime. A pump continually circulates the LAr in a closed loop through a 0.1 part per billion purification system through the detector and back to the pump to remove oxygen content. The LN2 supply Dewar is the source of all refrigeration, re-condensing argon gas boil off from the heat load of the system, controlling the operating temperature and pressure of the Detector assuring stable operating conditions.

Table 4.1: Summary of Heat Load Estimate.

5000 gallon LN2 Dewar	200 Watts
Two cryogenic liquid pumps	100 Watts
50,000 gallon LAr Dewar	500 Watts
Dual LAr Purifier	100 Watts
Cryo valves and transfer lines	200 Watts
Detector Head Vessel	100 Watts
Detector Vessel	250 Watts
Cold Electronics and Conduction Heat	250 Watts
Total	2850 Watts

System Heat Load

40 layers of super insulation will cover all surfaces of the cold vessel to reduce radiative heat from the warm vessel to below 1 Watt per square meter. However, the total heat load that must be absorbed by the refrigerant includes all heat. Heat input such as pump work, storage Dewar losses, transfer line losses and probably the largest load of all, Joule heating from the cold electronics including heat conduction losses of the 12,000 data and instrumentation channels.

However a distinction has to be made between heat that goes directly into the detector liquid and heat that can be shunted into the refrigerant flow and only adds to the system load. Special care will be taken to manage the detector liquid heat load by bypassing as much heat as possible away from the sensitive fiducial volume. A simplified layout diagram of the cryogenic system is shown to help understand the distribution of the heat loads shown in the estimate.

Cooling Scheme

This proven design, shown in Figure 4.4, has been used to cool many LAr detector systems, both past and present. It is made up of a detector vessel full of liquid and a head vessel filled to 20%. An LN2 cooling loop placed at the top of the head vessel controls pressure of the liquid/gas interface to 1.25 bar. Its equilibrium saturated vapor temperature is 89.3K. Some 5 meters below, the bottom of the detector sees a pressure of almost 2 bar and if left alone would be boiling at a temperature of 93.6K. In order to minimize detection errors, the sensitive volume should be quiet, have no boiling, and be as near to isothermal as possible. Liquid nitrogen cooling loops sub-cool the LAr which stops all boiling as computer control holds the detector temperature at 87.3K. Of the total system heat load about half comes from the cold electronics positioned along the top of the fiducial volume. Therefore, an LN2 cooling loop is placed to intercept the Joule and feed-through heat to counter its thermal effect. One or two additional cooling loops will be added to the detector after ANSYS modeling.

The dual purifier in Figure 4.4 is the heart of a circulating system that continually removes oxygen from CV LAr. Flow will be sized to provide about 38 liters, or 10 gallons of argon per minute, which will take 2 days to pump an equivalent CV volume through the purifier. Filling the detector can be from a truck or from the 50k gallon storage Dewar. A large storage Dewar is expensive but provides enhanced flexibility in a number of ways. For instance, early in construction of the MicroBooNE system the storage Dewar could be filled getting a head start on the purification process. Or if the detector had to be emptied all the argon would be transferred to the storage Dewar where it would be continually refrigerated and purified. When ready to go back on line, detector cool down and refill would only take a few days. All of these large Dewar advantages carry cost factors which will be studied in detail.

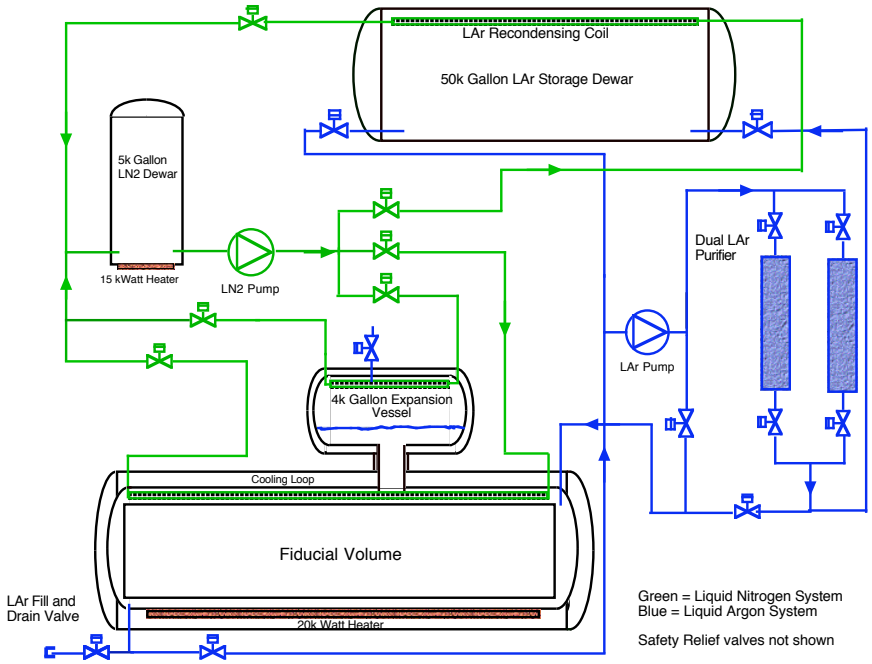

Figure 4.4: Cryogenic System Basic Layout

Vacuum Systems

Proper preparation of vacuum spaces, pump down and purging of all super-insulation is of primary importance during construction and operations. At least three vacuum pumping systems, along with proper gauging, will be needed to keep storage vessels, detector and transfer lines at or less than an operating pressure of E-5 milli bar to minimize conductive heat loads. One pumping station will be small and portable to move from one transfer line section to another while the large vacuum space vessels will require two, two stage systems with mid to high pumping capacities.

Process Controls

The detector system, while reasonably large in volume of LAr, is small when one speaks of its process control system. Use of purchased LN2 for the refrigerant is most economical

through a 10 year running period so a refrigerator will not be used. Lack of a refrigerator also reduces the control system I/O count by 60%. So a control system for this level of complexity will need about 150 I/O points, two operator interface displays and a few computers. The cryogenic system will programmed to operate in an unattended, automatic mode managing temperatures, pumps and purifiers with status and alarm information available locally and on the WWW. Control settings and alarm acknowledgement/resets will be pass word protected. Many suppliers of these kind of commercial process systems are available today.

Purification System

While the scheme to achieve clean argon in MicroBooNE has been adopted from ICARUS [10, 41], the system deviates from the ICARUS implementation in the use of the oxygen filter material used and the ability to regenerate the filter in place. This filter system has been designed and implemented at Fermilab. Tests at Fermilab and at Yale University have demonstrated these filters are easy to construct and regenerate and can achieve the required purity for LArTPC experiments as described below. ArgoNeuT will also use these filters and therefore serve as a test bed for the MicroBooNE system.

Filter design: The oxygen filter material, a copper aluminum catalyst aquired from the Trigon corporation, removes Oxygen from Liquid Argon passing through the filter, trapping it in the Trigon granules. As Oxygen is captured in the Trigon, the filter material becomes depleted. Once depleted, the filter can be regenerated in situ [42].

The filters for MicroBooNE will be larger versions of the filters constructed for the test systems at FNAL and Yale. The filters used at FNAL and Yale are constructed of $2\frac{3}{8}$ inch outer diameter pipe filled with Trigon granules and capped off with sintered metal shown in Figure 4.5. The sintered metal provides some flow resistance which helps spread fluid flow from the $\frac{3}{8}$ inch outer diameter input tube through the volume of the filter. As

well, the sintered metal helps to prevent dust from the Trigon from exiting the filter. A thermocouple installed in a tube at the center of the filter monitors temperature during the regeneration process. Figure 4.6 shows the inside of a filter with the thermocouple tube visible inside the pipe.

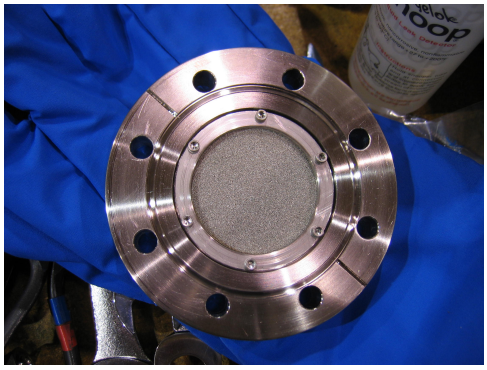

Figure 4.5: Sintered metal filter endcaps.

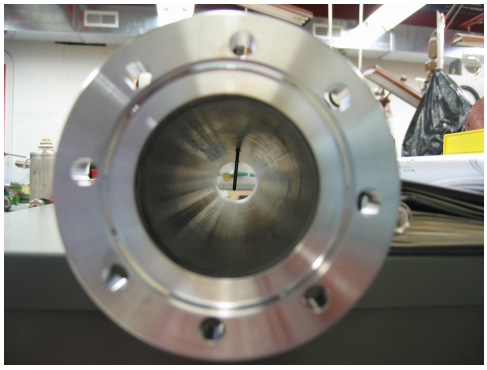

Figure 4.6: Inside of filter with thermocouple tube visible.

The filters are regenerated following the manufacturer's instructions. They are heated to 250 C and purged with a 95/5 flow of Argon/Hydrogen. A dew point monitor in the exhaust stream from the filter indicates when regeneration is complete, nominally after 9,000 volume changes through the filter. After baking and regeneration, the input argon system was maintained under argon. Filters have been regularly regenerated successfully at Fermilab and Yale.

Purity Testing: The effectiveness of the filters is demonstrated by testing the purity of argon that has passed through the filter. Standard ICARUS style purity monitors will be used to test purity. These purity monitors, shown in Figure 4.7 work as follows: a photocathode is illuminated using a Xenon flashlamp and ejected photoelectrons are drifted from the purity monitor's cathode to anode. The electron drift life-time can be determined from the size of the cathode signal, the size of the anode signal, and the time between the two signals. Figure 4.8 shows the cathode and anode signal separated by a 5.7ms drift measured in a test setup at Fermilab.

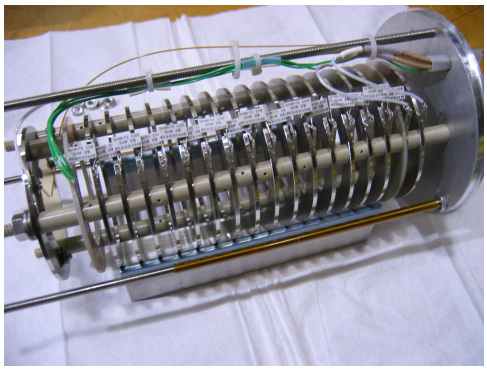

Figure 4.7: An ICARUS style purity monitor, constructed at Fermilab.

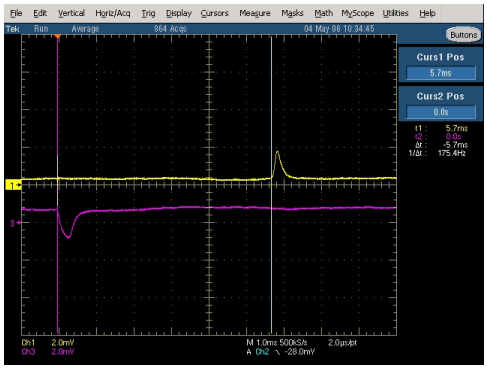

Figure 4.8: Signal from cathode and anode from FNAL purity measurements using an ICARUS style purity monitor. Test indicates 5.7ms electron lifetime.

In addition to demonstrating purity using a purity monitor, seeing tracks in a liquid argon TPC is strong verification of good purity. Tracks from passing cosmic rays, shown

in Section 2.3.2 were observed for the first time in the US using a small prototype TPC at Yale, demonstrating good purity can be achieved with these filters.

The MicroBooNE purification system: As in ArgoNeuT, the MicroBooNE purification system is comprised of two filters which can each be regenerated in situ. When one is under regeneration, the other is used for purification. Figure 4.4 shows the two filters and associated plumbing. Several purity monitors will be installed in the MicroBooNE detector to measure purity.

4.2.3 Vacuum Feed-throughs

To operate the detector feed-throughs between the cold and the warm vessels get preamplifier signals and monitoring signals out and preamplifier power and calibration signals in. In addition, a feed-through brings in the HV needed for the wire chambers. These are described below.

- Signal/Calibration and monitoring feed-throughs: High density pin carriers for a cold feed-through design based on the ATLAS design developed at BNL [10] will be used. 180,000 channels have been installed in ATLAS and have been operating for over a year in the experiment. There has been no failure of any of the pin carriers. In Fig 4.9 the top view of one of the feed-through flanges is shown.

- Wire bias feed-throughs: The readout chambers will need to be supplied with +200, -400 Volts. These HV will be supplied through the same feed-through as the signals. The feed-throughs have been certified to 500 Volts in the ATLAS experiment where they are used to supply the HV for the forward calorimeter.

- HV feed-through: The HV feed-through design is a challenge as we need to carry up to 200 kV in order to bias the field cage. A possible solution is to use a warm feed-through as used in the ICARUS detector [10]. This is still under study.

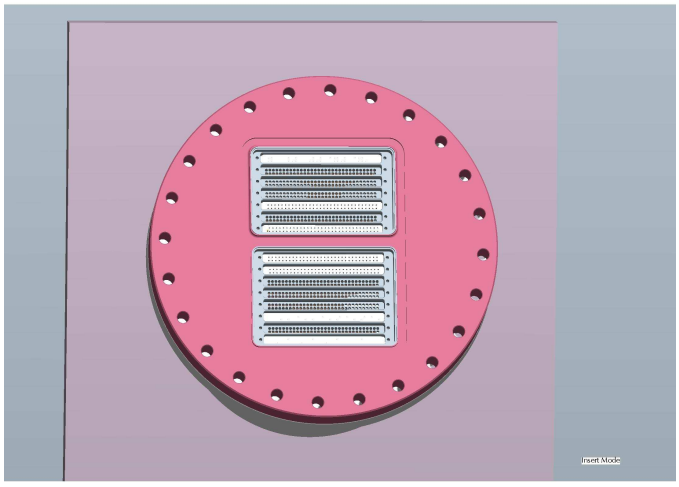

Figure 4.9: Feed-through flange with 7 and 8 row pin carriers. Each carrier row has 64 pins.

4.3 Detectors

In this section we describe the proposed implementation of the active parts of the detector that are composed of LArTPC and photomultipliers used to give us timing information of when energy is deposited.

4.3.1 Overview of LAr Properties for Time Projection Chambers

Liquid Argon as an active medium in TPC detectors is a technology very attractive due to the high ionization rates (i.e. high density), relatively low electron attachment and high drift velocity allowing for long drift distances as well as limited costs (despite requiring cryogenic systems). Table 4.3.1 summarizes the main properties of LAr as a detection medium.

The intrinsic performances of a LAr detector are intimately connected to the transport properties of the charge carriers in LAr. In the following sections we will review the parameters that must be considered for the design of a LAr TPC: drift velocity, diffusion, recombination and attachment are key elements for the ultimate spatial and energy resolutions. They play an important role since practical considerations set limits to the electric field value inside the LAr fiducial volume where the ionization electrons are drifted toward the wire planes.

Drift of charge carriers in LAr

Ion mobility in liquid dielectrics is usually in the range of $10^{-2} - 10^{-4} cm^2 V^{-1} s^{-1}$, several order of magnitudes smaller than the electron mobility. Experimental measurements in LAr are found in [43] and shown in Fig 4.10.

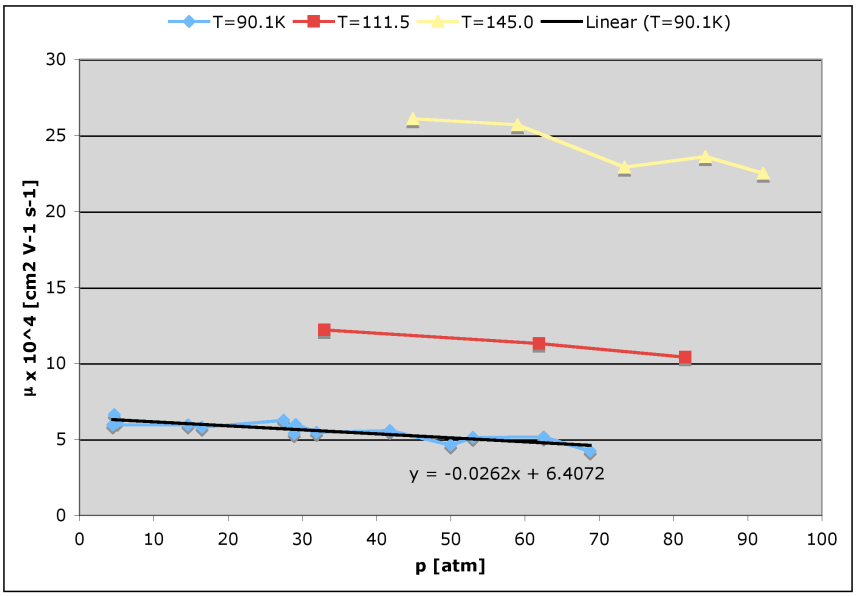

Figure 4.10: Ion mobility measurements in LAr vs. pressure at different temperatures (from Ref. [43]).

Effectively, only drifting electrons determine the signal generation mechanism in the detector. The transport properties of electrons in Liquid Argon have been extensively studied in the last few decades and accurately described near the triple point by the Cohen-Lekner theory [44], which extends the Landau, Davydov, Shockley [45] model to take into account the atomic structure of dense systems in the phonon emission and absorption mechanisms. Figure 4.11 summarizes some of the data available (Refs. [46, 47, 48, 49, 50]) on the electron drift velocity under the action of an external electrical field. In general it is possible to distinguish a region where the drift velocity depends linearly on the electric field from a region where such dependency weakens ($\sim \sqrt{E}$). The transition occurs approximately when the drift velocity becomes comparable to the LAr sound speed [200-400V/cm in LAr].

More practically, empirical functions have often been used (see Refs. [47, 51]) to fit the data. Ref. [47] uses a 5th-order polynomial and Ref. [51] interpolates data taken at

different temperature as well by

$$v_{Drift}(T,e) = (1 + P_1(T - T_0) * (P_3 E ln(1 + \frac{P_4}{E} + P_5 E^{P_6}) + P_2(T - T_0) \quad (4.1)$$

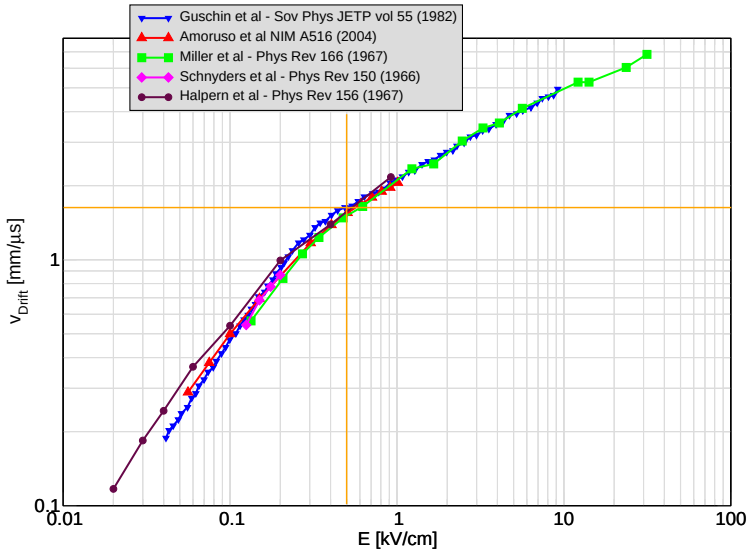

Figure 4.11: Electron drift velocity vs. drift electric field (T=89 K).

The parametrization in Eq. 4.1 represents quite accurately the above data starting from a field of 0.4 kV/cm. It describes as well as the dependency on the LAr temperature in the range 85K-95K (Ref. [51]).

Let's consider as an example an electric field of 0.5 kV/cm. The drift velocity is about ∼1.6 mm/μs. The relative change in velocity is:

$$\alpha = \frac{1}{\nu_{Drift}} \frac{\delta \nu_{Drift}}{\delta T} \approx -1.97\%/K \quad (4.2)$$

Eq. 4.2 can be used to settle a requirement on the maximum temperature gradient and stability in the fiducial volume or alternatively on the monitoring operations of such a detector: in the former case let's assume the resolution Δx in the drift direction to be comparable to the pitch of the wires that determines the remaining 2 coordinates over

the full fiducial volume (2.5m max. drift):

$$\delta T = \frac{\delta x}{L_{max}} \frac{1}{\alpha} = \frac{0.003}{2.5} \frac{1}{0.0197} \approx 0.06K \tag{4.3}$$

which is an extremely tight tolerance and it is not clear can be achievable even with a very sophisticated cooling circuit. On the other extreme one could envision detector operation with a much looser local tolerance ΔT and correct the data offline by monitoring the LAr T in different positions. Let's consider a LAr volume where:

1. The hydrostatic pressure drop over 2.5 m (fiducial volume height) is Δp$\sim$0.36 atm.

2. For a free boiling surface at the top of the cryostat kept at T=89 K,

$$\delta T = 1K \Longleftrightarrow \delta\rho = 0.118atm \tag{4.4}$$

3. Yielding a gradient of ΔT=3.3 K

4. Along the vertical direction in the fiducial volume we can position temperature sensors so as to effectively segment the detector into smaller volumes in which a looser tolerance on the temperature gradient can still allow for the desired spatial resolution. It is easy to verify that the optimal number of sensors is simply:

$$N_{opt} = \sqrt{\frac{L_{max}\alpha\Delta T}{\delta x}} \approx 7 \div 8 \tag{4.5}$$

5. The expected maximum temperature gradient, the height of such a smaller volume and the spatial resolution achievable would become respectively:

$$\delta T = \frac{\Delta T}{N_{opt}} = 0.41K \tag{4.6}$$

$$\delta L = \frac{L_{max}}{N_{opt}} = 0.31m \tag{4.7}$$

$$\delta x = \delta T \delta L \alpha = 0.0025m \tag{4.8}$$

6. Alternatively or additionally an offline correction on muon tracks can be envisioned.

Diffusion

There is little data available in the literature for condensed noble gases. Liquid Argon measurements of the ratio of the diffusion coefficient to the electron mobility can be found in [52]. Electrons drifting under the action of an electric field diffuse with time following Gaussian distributions:

$$n = \frac{N_0}{4\pi D_\tau t\sqrt{4\pi D_L t}} exp(-\frac{\rho^2}{4D_T t}) exp(-\frac{(z+v_{drift}t)^2}{4D_L t} \tag{4.9}$$

The maximal spread is:

$$\sigma = \sqrt{2DT_{drift}} = \sqrt{2\frac{DL}{4D_T t}} \approx \sqrt{2\frac{D}{\mu}\frac{L}{E}} \tag{4.10}$$

Figure 4.12 shows the ratio $\frac{D}{\mu}$ as a function of the drifting field. Data points are a measurement set (for a LAr gap between the electron source and the ion chamber collecting electrode of d=1.7mm) from [52] fitted with a power-function of the electric field.

The spread due to diffusion results in a weak function of the electric field, which if extrapolated at the the proposed field value (i.e. 0.5 kV/cm) yields:

$$\sigma = \sqrt{2\frac{D}{\mu}\frac{L}{E}} \sim E^{-0.1284} \approx 2.1mm(@0.5kV/cm) \tag{4.11}$$

Doke ([53, 54]) analyzes the measurements in [52] plotting directly the dependency of the diffusion coefficient vs. the density-normalized electric field (see Fig. 4.13). Assuming a constant diffusion ($\sim$15.5 cm^{2}s^{-1}) coefficient the calculation of the spread from Eq. 4.10 would provide $\sim$2.2 mm, consistent with the estimate above.

Recombination

Recombination in LAr has been extensively studied in the literature. Theoretical models have been developed to fit the data based on Jaffe and Onsager theories modified to take into account δ-electrons and non-uniform charge distribution along their tracks.

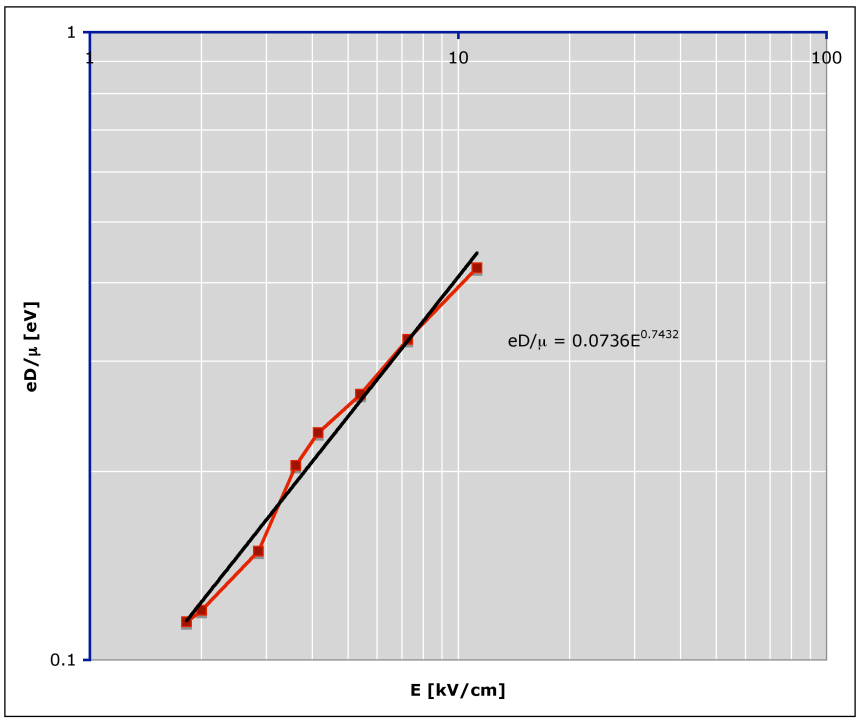

Figure 4.12: Diffusion coefficient to electron mobility ratio vs. electric field (from Ref [52]).

An excellent summary can be found in [55]. Recent measurements by the ICARUS collaboration with both the 3ton and the T600 prototypes can be found in [56] together with a critical review and analysis of the recombination data in [57, 58] with β-sources previously published.

Nonetheless there is no theory yet that can successfully describe the recombination processes in LAr. Here we adopt an effective phenomenological parameterization (Eq. 4.12) that fits the data in a limited range of stopping power and electric fields (∼0.2-10 kV/cm) and that is sufficient for an estimate of the charge losses due to recombination and to predict consequently the S/N ratio on the readout wires.

$$Q = A\frac{Q_0}{1 + k_1(\frac{1}{\Im}\frac{dE}{dx}) + k_2(\frac{1}{\Im}\frac{dE}{dx})^2 + k_3(\frac{1}{\Im}\frac{dE}{dx})^3} \tag{4.12}$$

ICARUS fits on muon and proton power losses in the 3t-prototype technical run (with

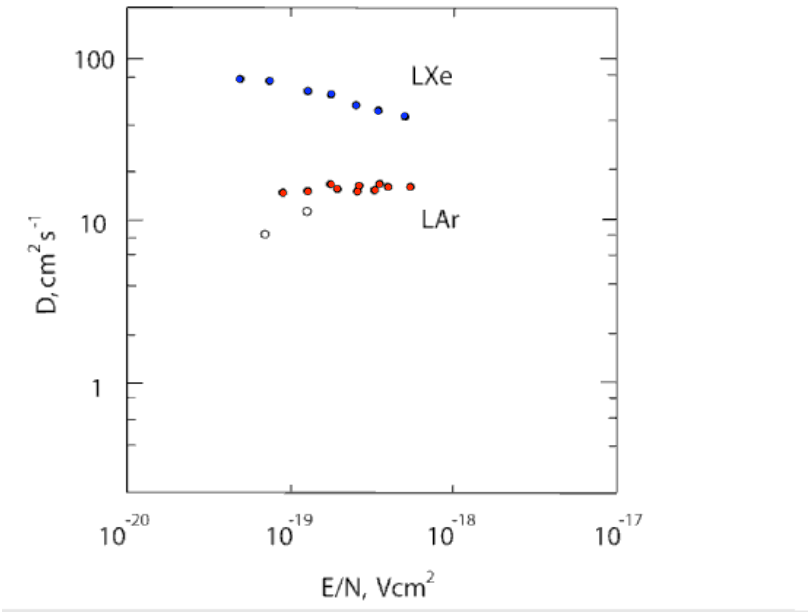

Figure 4.13: Diffusion coefficient vs. density normalized electric field (Redrawn from [53, 54]).

the power series in the denominator truncated to the first order) gives:

$$A = 0.08 \tag{4.13}$$

$$k_1 = 0.0347 kV/MeV \tag{4.14}$$

$$R = \frac{Q}{Q_0} \sim 0.70(@0.5 kV/cm) \tag{4.15}$$

Higher order terms are needed to fit 207Bi conversion electrons (976 keV) data in [58] yielding:

$$k_1 = 0.254 kV/MeV \tag{4.16}$$

$$k_2 = -0.072(kV/MeV)^2 \tag{4.17}$$

$$k_3 = 0.010(kV/MeV)^3 \tag{4.18}$$

$$R = \frac{Q}{Q_0} \sim 0.65(@0.5 kV/cm) \tag{4.19}$$

as shown in Fig. 4.14.

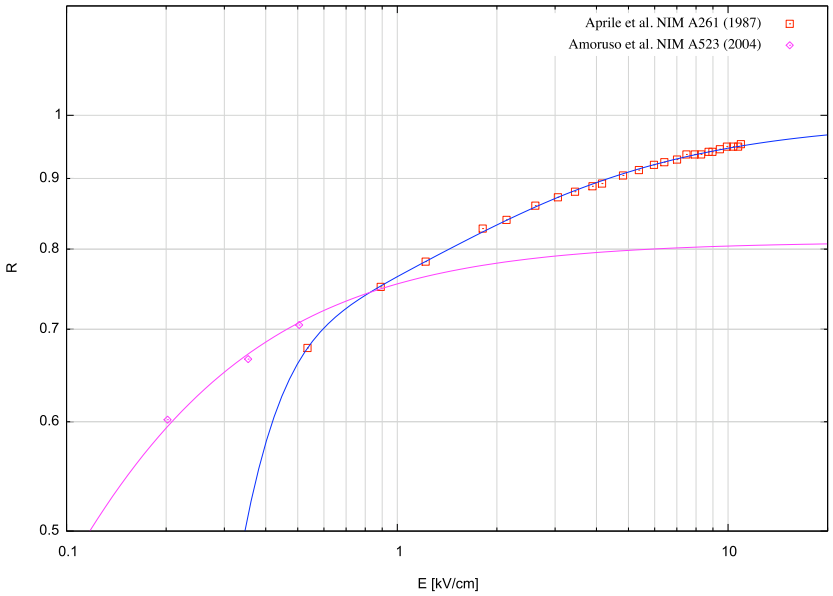

Figure 4.14: Recombination factor vs. Electric Field (from [56, 58]). □ Measurements (Ref. [58]) A 207Bi b-source (976keV conversion line) fitted with Eq. 4.12 [blue curve]. ◊ Measurements on the ICARUS 3t prototype with muons and protons. The fit line is what is used in Ref. [56], corresponding to Eq. 4.12 with the denominator power series truncated to k_1.

Purity, Attachement, and Electron Lifetime

Attachment to electronegative impurities in LAr causes a charge loss following the known exponential law where the lifetime τ_e is related to the different concentration of impurities in:

$$N(t) = N_0 exp(-\frac{t}{\tau_e}) \tag{4.20}$$

$$\tau_e = (\Sigma k_i n_i)^{-1} \tag{4.21}$$

Electron lifetime has to be kept as high as possible (same order of magnitude as the total drift time inside the fiducial volume). Fig. 4.15 shows on the left the charge collection fraction as a function of the electron lifetime for events far from the collection plane (near the cathode), half-way through and of the drift distance. On the right, the

collected charge as a function of the drift distance for a fixed electron lifetime (in this example taken equal to the drift time of the electrons).

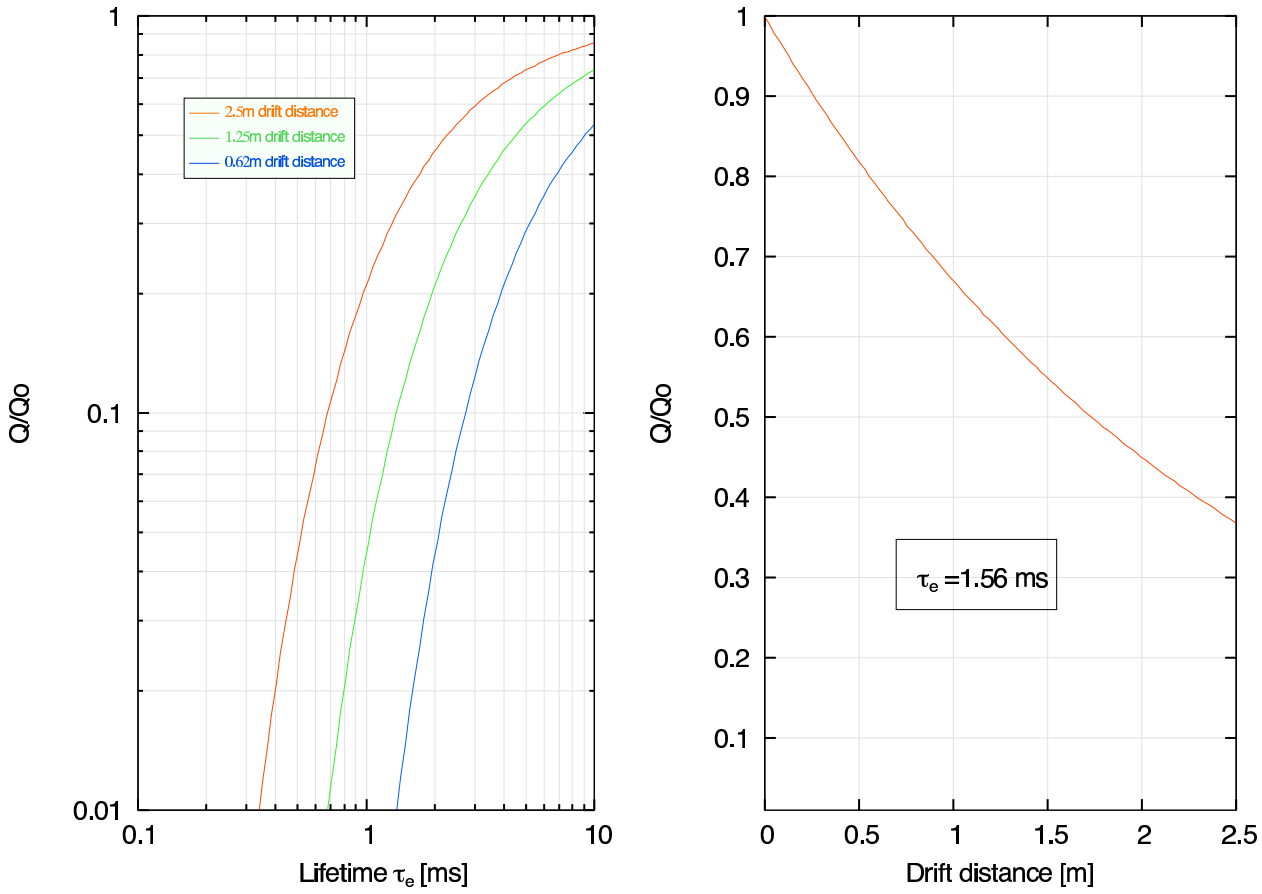

Figure 4.15: Left - charge collection fraction as a function of the electron lifetimes for tracks at different distances. Right - charge collection fraction as a function of the drift distance for a fixed electron lifetime. We are aiming for drift-lifetimes of better than 5 ms.

Offline corrections have to be taken to compensate for the charge losses as described in [59] provided T_0 of the event is known.

It is clear that purification for large drift applications is one of the most critical components of the detector. A continuous circulation of the liquid through a purifier is required as well as purity monitor detectors inside the LAr detector.

The ICARUS collaboration [59] studied in detail the lifetime effects on their T600 prototype performance. Measurements of lifetime both through purity monitor detectors and offline analysis of muon tracks allowed the collaboration to monitor the electron lifetime evolution during the technical run as shown in Fig. 4.16. Interestingly, they were able to estimate the rate of impurities diffusing in LAr by the lifetime drop during a shutdown of the LAr-recirculation system.

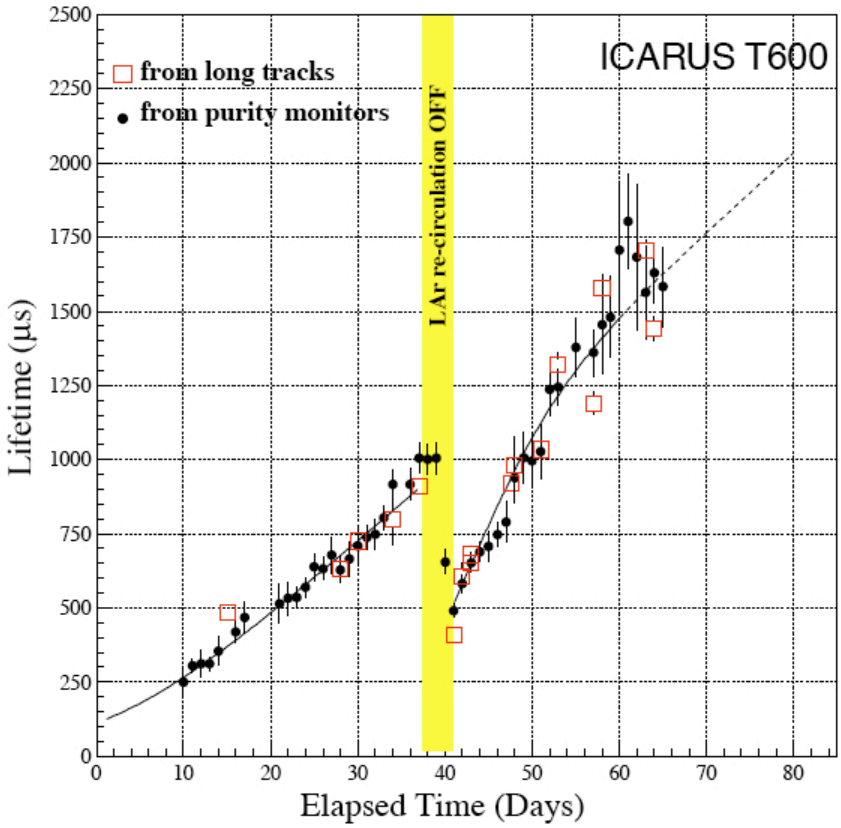

Figure 4.16: Electron lifetime evolution during the ICARUS T600 prototype technical run (from Ref. [5]).

4.3.2 Detector Conceptual Layout

The conceptual layout of the detector is depicted in Fig. 4.17:

- A cold vessel with ID 3.8 m, the LAr active volume in a rectangular box of approximately 2.6x2.56 square meters, slightly offset from the center of the vessel to give 130 mm clearance of the HV-cathode plane from the vessel walls (left bottom corner). The structure is approximately 12 m long.

- The cathode plane on the left is biased at 130 kV to provide an uniform drifting electric field of 500 V/cm, left-right horizontally in the picture (defining conventionally the x-axis).

- To guarantee uniformity all around the top and bottom side of the cage, tubes of 25 mm OD with 40mm pitch are biased with decreasing voltages at 2 kV steps.

- On the right side of the cage 3 readout planes with wires spaced 3mm respectively in the U,V,Y directions. The Y wires are vertical and the U,V wires are at +/- 60^o from the Y wires.

- The U-V planes will be induction planes. The Y-wires will collect the charges produced in LAr. A ground grid 10 mm behind the Y-plane is installed to shield field irregularities from any metallic structure supporting the wire frame.

- 3 rows of PMTs sensitive to VUV light from LAr scintillation are installed behind the grid. They will determine the T_0 of the event required for background suppression.

- The readout front-end will be housed on PCB mounted on the top right corner of the cage. Output signals will be driven to the signal feed-throughs and to readout electronics mounted in racks directly above (see Sec.).

- Cryogenic, vacuum and LAr services are mounted on the top of the vessel. These are described in detail in Sec. 4.2.

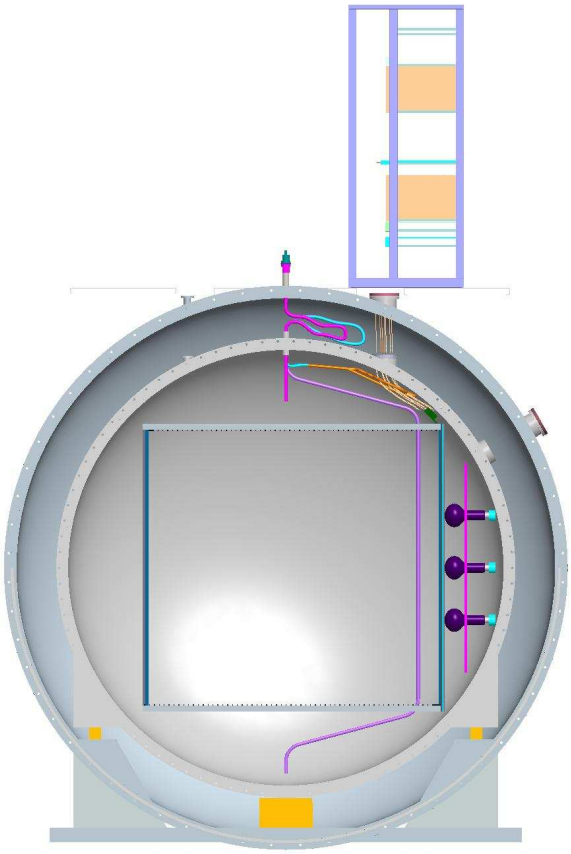

Figure 4.17: Conceptual Layout of the Detector.

4.3.3 HV Drift Cage

The HV drift cage must provide a uniform electric field for the electrons to drift to the wire planes without significant distortion. The nominal drift field for this TPC is 500 V/cm. 130 kV is required on the cathode end to cover the 2.6 m long total drift distance. To maintain mechanical strength and simplify construction, arrays of stainless steel tubes will be used as the drift electrode. Tubes with diameters of 2.5 cm, at a 4 cm center-to-center distance biased with decreased voltages at 2 kV steps will guarantee adequate uniformity of the drifting field.

The top and bottom planes of the drift cage span the 12 m length of the TPC. It is

difficult to keep the tubes from sagging due to their own weight without any intermediate support. We plan to install PEEK or Ultem beams with holes to hold the field grids at periodic intervals. These support structures not only carry the weight of the field grids, but also tie the HV cathode plane together with the heavy wire frame.

The drift cage electric field has been simulated in a 2D electro-static field simulator, Maxwell-2D v.9 [59]. The results appear to be satisfactory for this application. The model used for these simulations is based on an earlier preliminary layout of the detector: cold vessel ID: 3800 mm, a rectangular region of 2600x2560 mm is offset slightly from the center of the vessel to give 130 mm clearance between the HV end of the two corners. Only the top half of the structure is used in the model due to its symmetry. Two solid conductor plates are placed at the left and right edges of this rectangle, a row of 25 mm diameter conductor rods are placed at the top of the rectangle at a 40 cm pitch. The cathode is biased at 130 kV (opposite polarity but it is irrelevant for the purpose of this particular study) and the rods are biased with decreasing voltages at 2 kV steps. An anode full plate is used to terminate the field since it is not possible to simulate the wires in this model.

Figure 4.18 shows the uniformity of the electric field inside the drift volume. The uniformity calculated is remarkably good. It deteriorates slightly at the corners, which will be used as a veto region. A detail of the corner at the cathode side is shown in Figure 4.19. An additional rod is placed to shape the field better and preserve uniformity. Indeed, notice that on the last shaping rod the maximum field reaches a value of 34 kV/cm on a 25 mm OD conductor.

As a quantitative estimate of the uniformity of the field along the lines of drift, we calculated the field variation along straight lines in the x-direction at 5, 10, 25 cm from the edge. Results are summarized in Figure 4.20: 20% maximum variation at 5 cm where the effects of the rods are clear (red curve in the figure), already 0.5% at 10 cm (blue curve), and less than 0.05% at 25 cm from the edge (green curve).

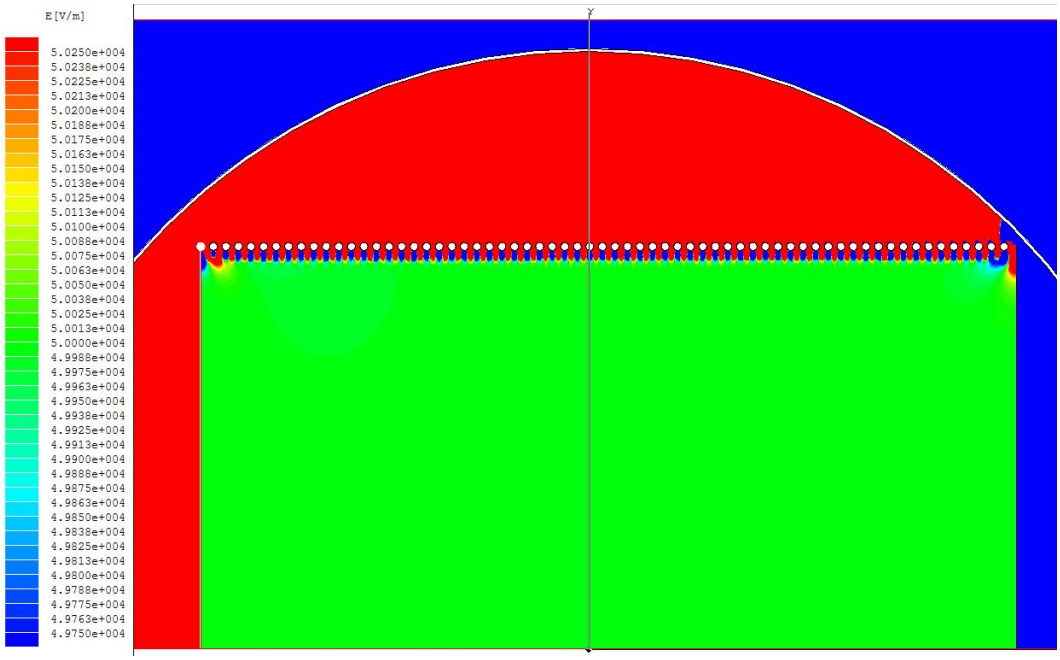

Figure 4.18: Uniformity of the electric field inside the drift volume.

A resistor chain is needed to provide the potential gradient on the field grids. The resistors must be rated at 5 kV at a minimum. To reduce the field distortion caused by a resistor failure, 4 equal value (∼100 M) resistors will be connected in parallel between any two grids. Holes will be drilled on the sides of the field grids, and gold plated brass sockets (MillMax type) will be pressed into the holes. The resistors will be plugged directly into the sockets. This resistor chain will dissipate about 10 W of heat inside the cryostat, so the resistors will be mounted on the upper edge of the end cap grids to avoid bubbles entering the drift volume.

4.3.4 Readout Wires

Wire Properties

The wire proposed for the readout plane is a gold plated 150 μm diameter stainless steel 304V. Some of the SS-304 specifications can be found on the Fort Wayne Metals Inc.

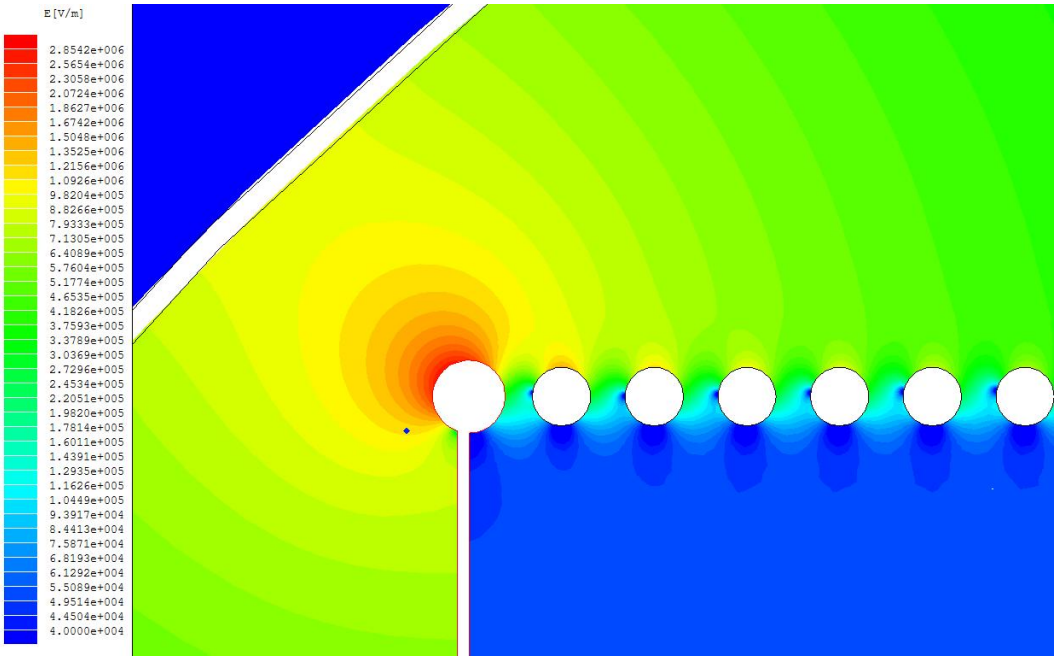

Figure 4.19: Contour plot of the electric field around the corner at the cathode side of the TPC. The maximum field is about 34 kV/cm on a conductor of 25 mm diameter.

website [60] and are summarized in Table 4.3:

The DL/L from 293 K to 90 K for SS 304 is quoted as 2.71×10^{-3} [61]. This number is smaller than that obtained from CTE at room temperature (18×10^{-6}/K), possibly due to reduced CTE at lower temperatures.

If we apply a 10 N tension on the wire, the amount of elongation on a 2.5 m wire is about 7 mm, which is almost identical to the amount of shrinkage on the same length of wire cooled to 90 K (6.8 mm). This implies that even if the wires were suddenly cooled down to 90 K, with the rest of the support structure remaining at room temperature, the additional tension on the wire caused by the shrinkage is only another 10 N. The total tension of 20 N is still only about half of the yield load of 38.5 N. From this point of view, the elaborate spring loaded tensioning structure ICARUS used is not necessary.

At 10 N tension, a horizontal wire 150 μm diameter spanning 5 m would have a sag in the middle of the order of 430 microns (see for example [62]). This represents a

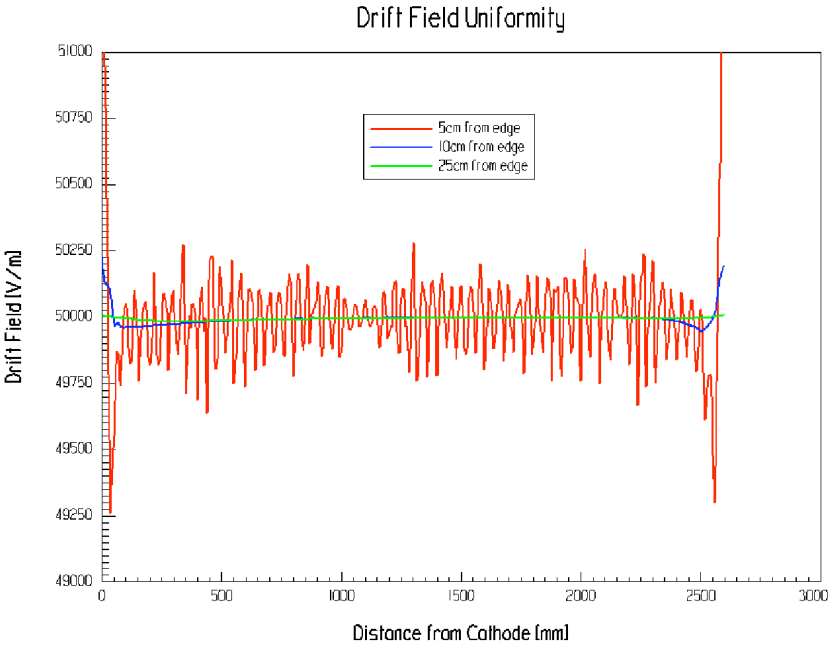

Figure 4.20: Variations in the drift field along lines of drift.

systematic error on all U and V wire planes, which is negligible compared with the 3 mm wire pitch and can be corrected. The slope of the maximum sagging versus tension relationship at a tension of 10 N is about 50 μm/N. So a $\pm$10% variation on the wire tension will result in $\pm 50\mu$m variations on the deflections.

Wire Holder

The wires will be installed in a modular fashion to streamline the production. Each wire holder module (32 wires in Y, 16 wires each in U & V) will be constructed from two printed circuit boards, with a total thickness of 3 mm. Each wire is stretched at the correct tension and crimped to two small stainless steel discs at both ends. These discs are encapsulated in rows of circular cavities in the wire holder. A row of gold plated press-in pins defines the location of the wires as they come out of the holder. These pins are connected to the connector at the top edge of the board through copper traces on the underside of the board. These connectors send the wire signal to the preamp boards.

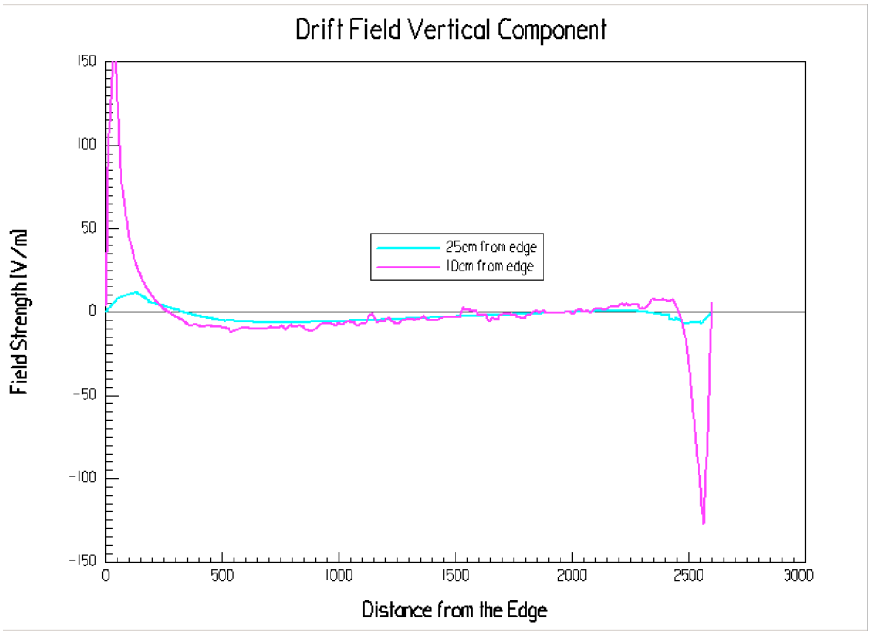

Figure 4.21: Vertical component of the drift field, along two lines of drift, 10 cm and 25 cm away from the centers of the field shaping rods (simulations by Maxwell-2D [60]).

Wire Plane Bias

In order to prevent collection of electrons on a plane of wires, one must maintain a proper ratio of electric field on both sides of the wire plane. Based on [63] the transparency condition is guaranteed by Eq. 4.22:

$$\frac{E_2}{E_1} \geq \frac{1+\rho}{1-\rho} \tag{4.22}$$

where $\rho = \frac{2\pi r}{d}$, d is the wire pitch and r is the wire radius.

The field ratio needs to be greater than 1.37 for a grid with 150 μm wires at 3 mm pitch.

A 2D simulation is made to estimate the voltages required on each wire plane to avoid charge collection. The middle wire plane is set at ground potential and a ground plane is placed 1 cm behind the Y wire plane to shield field irregularities from any metallic structure supporting the wire frame. The voltages on other electrodes are adjusted so

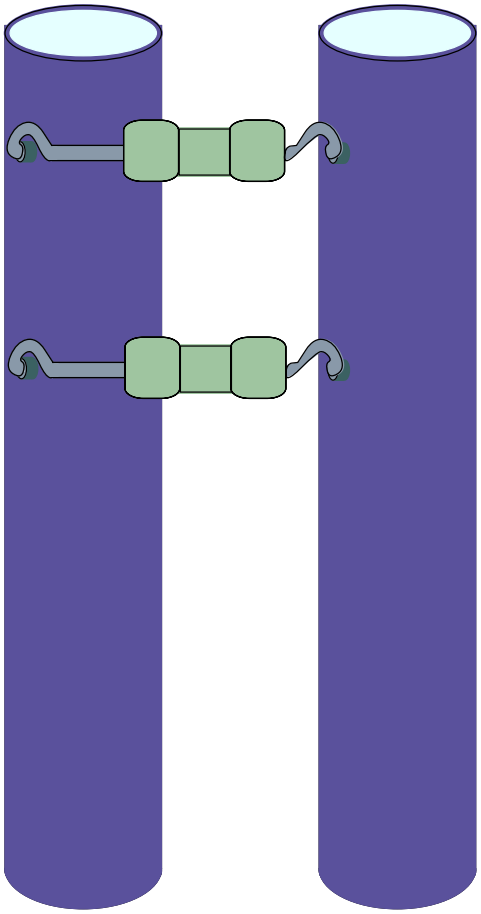

Figure 4.22: Conceptual layout of the HV resistor assembly.

that the first two planes of wires just begin to become non-collecting.

The voltages on the wire planes are: -204 V, 0 V, 440 V. The 440 V can be reduced to about 400 V by increasing the bias of the shielding plane to ∼300 V. However, the electron arrival time in places just between two Y wires will be increased due to a weaker field.

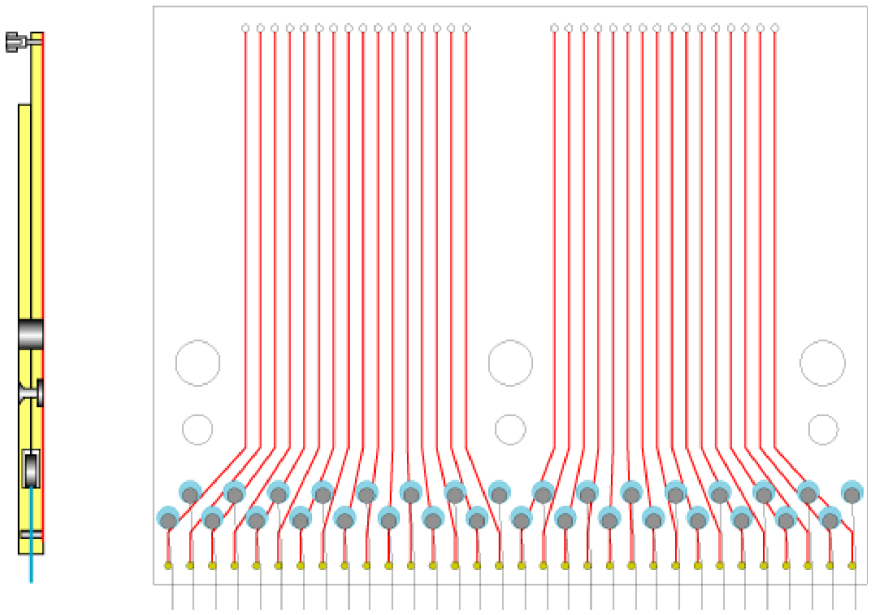

Figure 4.23: Wire holder conceptual design.

Table 4.2: General Properties of LAr

PROPERTY	**VALUE**	
Atomic Number	18	
Atomic weight [u]	39.94	
Atomic diameter [A]	3.42	
Radiation length [cm]	14.2	
Absorption length [cm]	83.6	
Moliere radius [cm]	10.1	
Critical Energy [MeV]	30.5	
$\langle \Delta\, E_{mip}(1\text{cm}) \rangle$ [MeV]	2.1	
W-values (1MeV electrons) [eV/ion-pair]	23.6	
Fano factor	0.107	
Electron mobility at bp [$m^2V^{-1}s^{-1}$]	0.048	
Ion mobility at bp ($\times 10^5$) [$m^2V^{-1}s^{-1}$]	0.016	
Oxygen trapping constant ($\times 10^5$) [m^2V^{-1}]	1.5	
Dielectric constant	1.6	
Heat capacity (C_P) [cal mol^{-1} K^{-1}]	10.05	
Thermal conductivity ($\times 10^3$) [cal s^{-1} cm^{-1} K^{-1}]	30.0	
Triple point temperature [K]	83.78	
Triple point pressure [atm]	0.679	
Triple point density [g cm^{-3}]	1.14	
Critical point temperature [K]	150.85	
Normal boiling point (bp) [K]	87.27	
Liquid density at bp [g cm^{-3}]	1.40	
Heat of vaporization at bp [cal mol^{-1}]	1557.5	
Gas/liquid ratio	784	
Temperature [K]	**Pressure** [bars]	**Density** [g/cm^3]
87.15	1.0	1.395
89.3	1.25	1.381
91.8	1.6	1.365
94.2	2.0	1.350
96.8	2.5	1.333

Table 4.3: SS 304-V specifications (from [60])

Yield Load	38.5N(8.65lb)
Modulus of elasticity	195 GPa(28.5Mpsi)
Resistivity	7.2 $\times 10-7\Sigma$ m
Density	7.9 g/cc

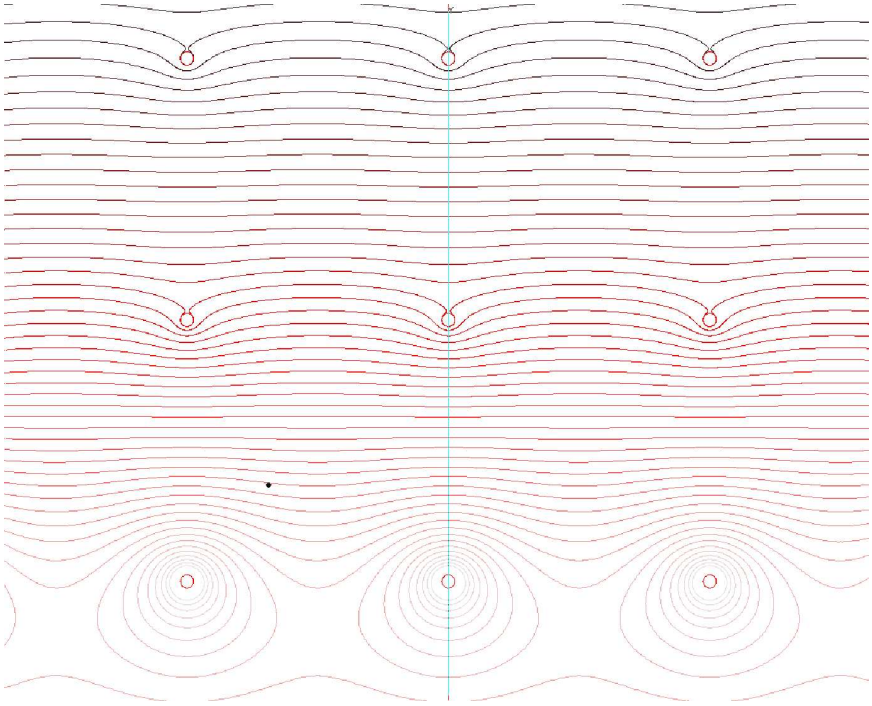

Figure 4.24: Equipotential contours of a section of the wire planes (simulations by Maxwell-2D [59]).

Results of the simulation are shown in Figure 4.24. Electrons drift downward and land on the bottom plane of wires. The potential along the blue line is shown in Figure 4.25 (around the wire on the 2nd induction plane). The slight upward bump to the right of the wire is the signature for a tiny non-collection.

The transparency condition has been verified independently by simulation with Garfield v.9 [64]. When the full transparency condition is met all the ionization electrons along the track will drift toward and will be collected by the Y-plane wires.

An example is shown in Figure 4.26: a horizontal (at y=0.5, red straight line parallel to the x-axis in the left plot's top side) track produces a constant ionization density "row". The geometry of the detector is what has been analyzed and proposed previously: 3 parallel wire planes (Garfield does not simulate 3D-geometries), 2 induction at y=0.3, 0 respectively and 1 collection plane at y=-0.3. The wire bias is respectively V=-205, 0,

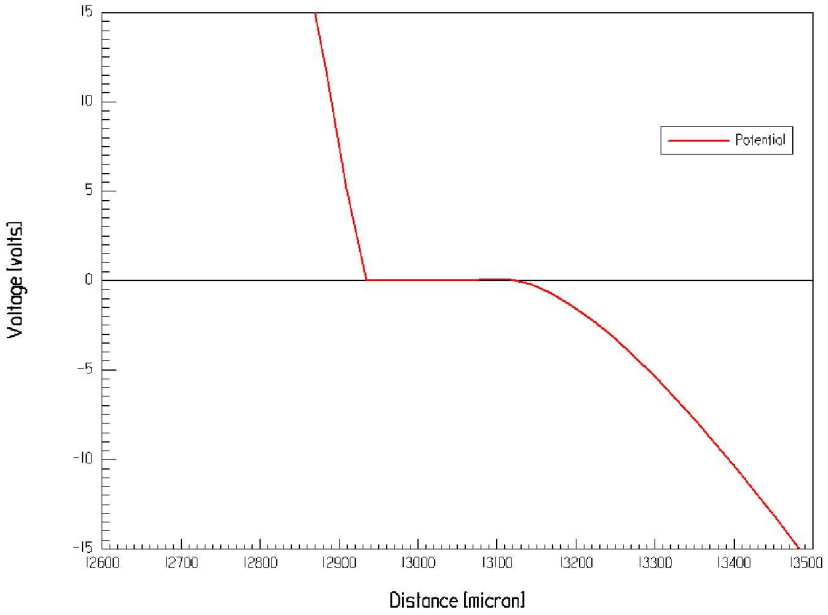

Figure 4.25: Expanded view around the second wire (simulations by Maxwell 2-D [59]).

440 V, while the drift electric field in the fiducial volume is 500 V/cm. Also, the grounded solid plane at y=-1.0 has been added in the geometry to guarantee the field-lines to close around the collecting wires. The left plot shows the drift of the ionization electrons generated along the track (orange curves), and the isochrones lines plotted every 0.1μs.

On the right plot the arrival time distribution of the ionization electrons is shown. The track's start represents the top-leftmost point of the "red" track in the left plot. The calculations have been carried out with CERN Garfield v. 9 [65]. It is interesting to notice that for these particular values of the fields the arrival times span over an interval of 600 ns.

$$\delta t = 600ns \Longleftrightarrow \delta x = 0.6/1.6 \approx 0.38mm \tag{4.23}$$

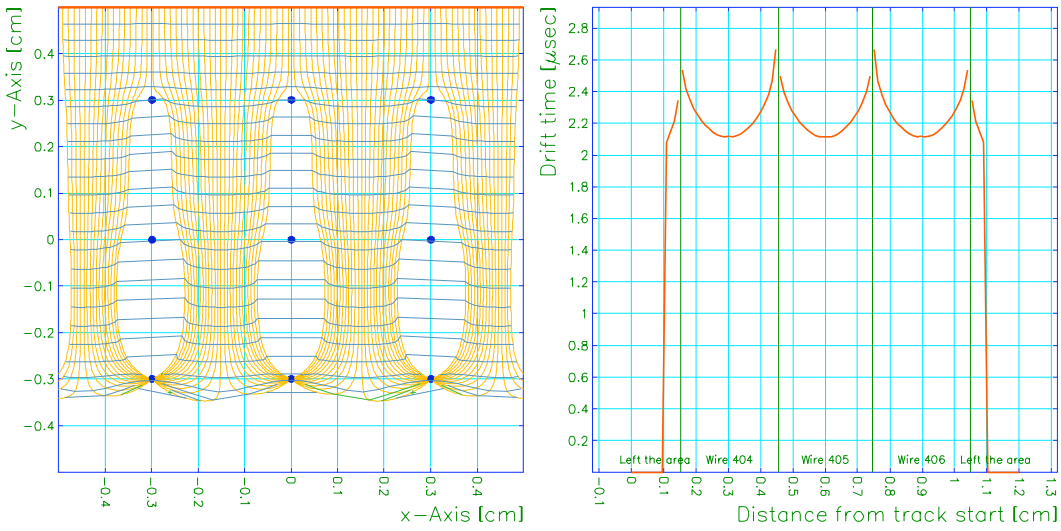

Figure 4.26: Drift Lines and Isochrones (left) for a constant ionization density track. Arrival times (right) for ionization electrons along the track to arrive on the collecting wires. Simulations made with Garfield-9.

4.3.5 Mechanical Support: Frame

The wire planes at 10 N tension per wire will exert 18 tons of force on the wire frame over 12 m. The frame must be stiff enough so that its deflection will not cause excess reduction in wire tension, and consequently wire sagging.

Fortunately, the Y wires that are directly impacted by the frame deflection are vertical, insensitive to tension change. The U and V wires are also less sensitive to the frame deflection due to their orientations and longer lengths. For example, a 1 mm deflection on the frame will give 1mm $\cdot$ cos(60)=0.5 mm reduction in wire elongation. This translates to a 10N $\cdot$ 0.5mm/14mm=0.36 N change in wire tension, and less than 20 micron additional sagging. As an example, a 5 cm wide, 10 cm tall, 6 mm wall thickness SS box beam supported at 2 m intervals has a 0.5 mm deflection under a uniform load of 5 kN/m [66].

Figures 4.27 and 4.28 illustrate a schematic of the wire frame structure. The top and bottom moveable wire frames are first retracted. Each 32-wire-module is attached to the

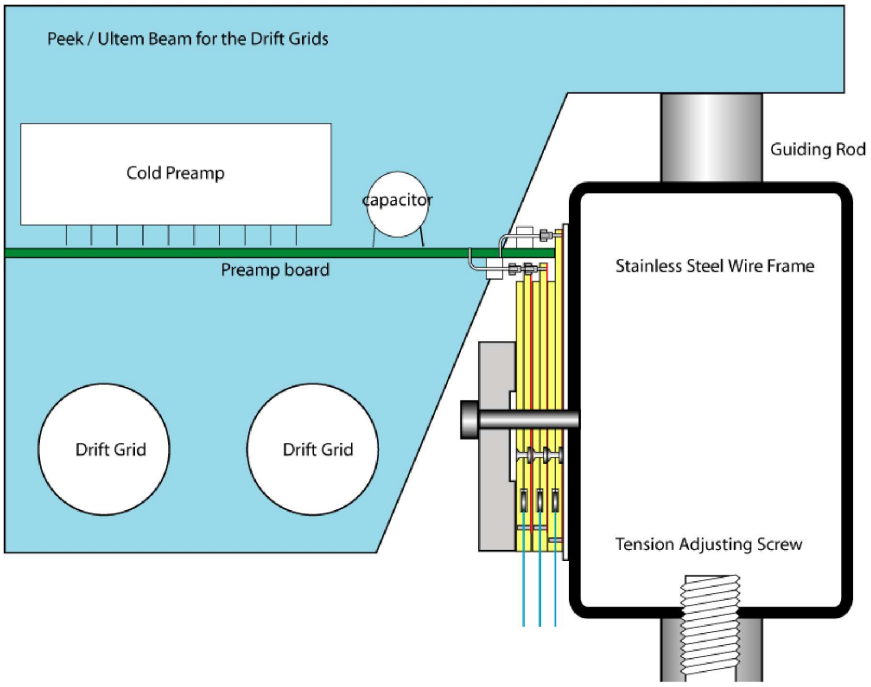

Figure 4.27: Artist's view of the mechanical support of the wire holder on the frame.

frames. The two frames are then extended using the tension adjusting screws distributed along their length, while the wire tension is monitored by a tension measuring device.

4.3.6 Trigger Detectors

Since an average rate of 3 cosmics/ms is expected in MicroBooNE with its 3m dirt equivalent overburden, the capability of reconstructing T_0 will allow us to suppress further backgrounds. Several options have been considered:

- Cover a fraction of detectors with PMTs sensitive to the VUV scintillation light from LAr and have them operating at cryogenic temperatures (ala ICARUS).
- Optical fiber grids with wavelength shifter running through the LAr detector. The fibers would go through special feed-throughs to PD outside the cryostat.
- Cathode readout of ionization signals

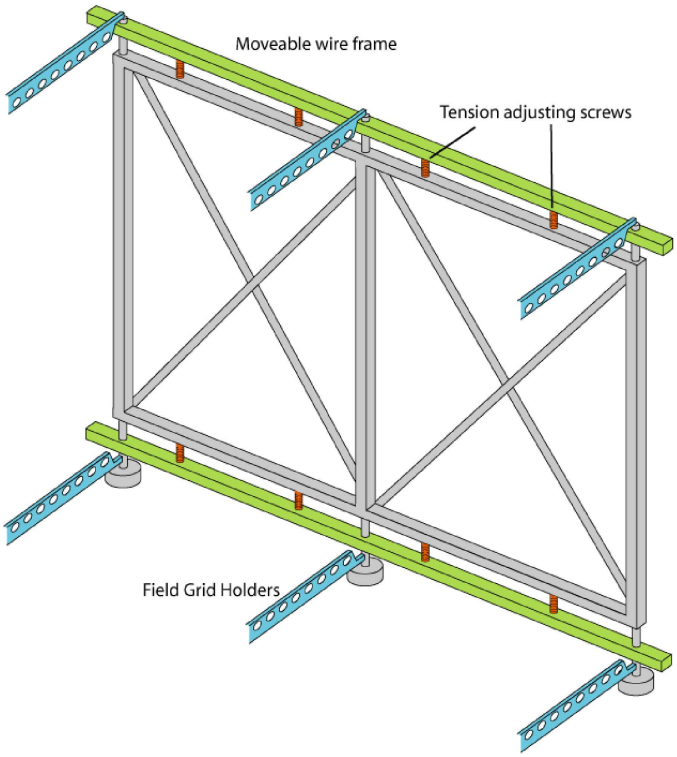

Figure 4.28: Schematic view of the supporting frame.

In considering each option, a cathode readout with large pads will have to address the question of S/N on relatively large input capacitance (in our geometry the capacitance to the cryostat wall could be much larger than the one to the anodic plane) and tiny signals. The readout through fibers and wavelength shifters has the drawback of presumably low light collection efficiency. As for the PMT readout, the main issues are related to photocatode response at low temperatures due mainly to a dramatic drop in quantum efficiency because of an increase of resistivity (charge restore takes longer times introducing dead-times even at very low event rates) and to change as a function of the light wavelength (see for example [64]).

While each option presents issues to be studied in more detail, the baseline design employs a photomultiplier array. This choice takes advantage of the many years of R&D by the ICARUS collaboration. The baseline design is described in detail below.

Figure 4.29 shows the array of PMTs in the MicroBooNE detector.

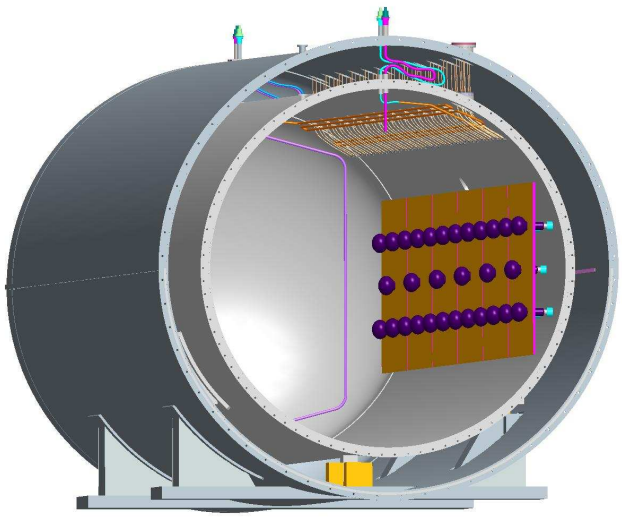

Figure 4.29: Artist's view of the PMT array in the cold vessel behind the readout wire planes.

Many studies have demonstrated that scintillation light from ionizing tracks in LAr provides a precise method of determining the time, T_0, of an event [10, 67, 68]. At this point, scintillation light in LAr is widely used in triggering various non-accelerator LAr experiments [69, 70, 71]. The decay time of the scintillation light is such that T_0 can be determined to the order of 10 ns.

In MicroBooNE, seeing light in coincidence with the $\sim$2 μs spill will indicate, most likely, that there is a neutrino interaction in the $\sim$2ms of readout. The overwhelming majority of spills without a neutrino interaction and therefore without this light tag will then be rejected as background.

Furthermore, for calibration, MicroBooNE will use non-accelerator sources. In particular, cosmic rays which stop in the detector and decay to produce Michel electrons, form a very valuable calibration sample, since the Michel electron spectrum is well known. Scintillation light can be used to determine a precise T_0 for reconstructing these events.

In designing this feature of the detector, we have used several criteria to guarantee that this is low-risk and low-impact to the project.

- The default design requires no R&D. It uses technology which has been demonstrated in the ICARUS T600 detector [10].
- The tubes which operate at cryogenic temperatures, and which are appropriate for this detector, are commercially available from two sources, Hamamatsu and Electron Tubes.
- The tubes are read out, along with the detector, on a continuous basis. They are not part of a triggering system. Information from the tubes will be incorporated offline.
- The tubes are positioned so as to not interfere with any other aspect of the design. They are located in the east and west "lunes" between the inner cylinder and the wires, which is an area not used for cabling.
- The number of feed-throughs for the tubes is minimized by ganging the signals from the tubes within the detector.

Below, we provide more information on scintillation light production and detection and our preliminary design.

Scintillation Light in LAr

Ionizing tracks produce scintillation light in argon at 128 nm. The light is produced through ionized and excited Ar states which then radiate during the recombination and de-excitation processes. There is a prompt and slow component to the light which is 7 ns and 1.8 μs, respectively, in a ratio of about 0.5:1 for electrons. The light yield is

high, $\sim 10^4$ photons/MeV [10]. Once the light is produced, the pure-argon mixture is transparent to the light.

The scintillation light from LAr is at a remarkably short wavelength and studies have shown that Xenon can be added to the LAr detector in order to shift the light from 128 to 175 nm. Xenon shifts the light by transferring the primary excitation from the argon to the xenon atoms though both radiative and non-radiative (collisional) processes. When Xenon is added at the few percent level, this produces a decay time of ~ 10 ns. In fact, if Xenon is added at the ~ 100 ppm level, the shift in wavelength can still be observed [72].

Doping with Xenon is being considered as an option for MicroBooNE. However, the design presented here assumes that pure LAr will be used, as was used in the ICARUS T600 Module.

The T600 PMT Design

Prior to the construction of the ICARUS T600 test module, extensive studies were performed on photon detectors for scintillation light from LAr [67, 73]. There are two issues: operation in the cryogenic environment and detection of the UV photons.

ICARUS used the ETL 9375FLA PMT which is specifically manufactured for cryogenic use and has a K_2CsSb+Pt photocathode. Because of the semiconductor nature of photosensitive material, most PMTs demonstrate a rapid increase in resistivity at low temperature, making them unusable at LAr temperatures. Depositing a platinum undercoating below the standard biakali cathode improves the sensitivity substantially. At $T = 77$ K, the sensitivity is only 20% lower than at room temperature [73].

The PMT glass is not transparent to 128 nm light. Therefore, the tubes were coated with TetraPhenyl-Butadiene (TBP) fluorescent waveshifter. An alternative material, Sodium Salicylate (SS), was also considered but found to have a lower conversion effi-

ciency. The materials are applied by dissolving them in a solvent and then applying them to the glass surface with a nebulizer to obtain a fine-grained uniform surface. Some care must be taken to avoid thicknesses larger than 100 μg/cm^2 in order to assure the best adhesion and performance. The total quantum efficency with the optimal thickness at cryogenic temperatures is 8% [10].

Photocathode coverage was chosen to assure sensitivity down to 5 MeV. The apparatus consisted of two half-modules, called T300, which had dimensions of 3.6 m $\times$ 3.9 m $\times$ 19.6 m each, and only one was fully instrumented with 54 tubes, while the other had 20 tubes. This represents remarkably low photocathode coverage compared to a typical unsegmented scintillator-based neutrino detector. Each PMT is $\sim$ 0.03m^2 and the total surface area of a T300 module is 333 m^2. This emphasizes that the number of scintillation photons per MeV is very high. The PMTs were mounted along the long side of the detector, looking through the wire plane of the TPC.

The Proposed MicroBooNE Tube Layout

We propose to use 8 inch tubes purchased from either Electron Tubes (ETL 9357FLA) or Hamamatsu (R5912-02MOD). The former has 12 stages and the latter 14 stages. Both use a K_2CsSb+Pt photocathode and CsSb dynode. Detailed comparison of the performance of these two tubes at $T = 77$ K can be found in reference [**?**]. These tubes run at 1200 to 1500 V. The bases will be purchased with the tubes.

Prior to installation, tubes will be tested in air using an existing test station. They will be tested with a blue Picoquant light source and will be sorted according to criteria developed by T600: narrow, fast anode pulse, good single electron resolution, narrow time resolution, low dark noise rate and low after-pulsing rate. Our expectation, based on the T600 experience, is that 75% of the tubes will pass the quality checks. Thus we propose to purchase 40 tubes, with the plan of identifying 30 good tubes for installation in the detector.

In the baseline design, 30 PMTs will be located on the east lune of the MicroBooNE detector, behind the wire chamber planes and along the 10 m distance of the fiducial volume. This provides twice the photocathode coverage of the T300 module, and therefore may be reduced on further study. The curved wall of the cylinder is an advantage for assuring full coverage of the fiducial region. The maximum depth of each lune is 0.58 m, thus there is room for two rows of tubes with MiniBooNE-style mountings.

The signals from sets of tubes will be multiplexed to minimize the number of feedthroughs. The multiplexed signal will be taken to a readout card which has been developed and debugged for the VLAND experiment [74]. The electronics digitize the charge as a function of time at a rate a 20-30 times faster than past electronics such as those used at LSND/MiniBooNE, and are more than suitable for the needs of MicroBooNE.

4.4 Readout Electronics and DAQ

4.4.1 Requirements and General Considerations

The readout electronics has to process signals for a total of about 10k channels. The readout channels are distributed on 2 induction planes (i.e. U, V planes) with wires running at 30^o, 150^o with respect to the beam direction (z-axis) and 1 collecting plane (Y-plane) with wires running perpendicular to the beam as detailed in Section 4.3.

The main requirements can be summarized as follows:

- The dynamic range is determined on the high-end by the ionization losses of recoil protons as well as by the losses of electromagnetic showers up to ∼3 GeV in the central core at the maximum of the shower development.
- On the lower end the readout must allow, with a good S/N ratio, the detection of MIPs tracks on induction wire planes at the maximum distance between two consecutive wires. Noise will thus be kept as low as possible.
- Reconstruction of shower imaging and energy may lead to the analysis of up to approximately 1-4 k wires. Coherent noise over many wires should be kept at the minimum.
- Signals should be sampled at a rate at least equal to $4\tau^{-1} \sim$ 2-5 MHz, τ being the shaper peaking time. Over-sampling is highly desirable for noise filtering and monitoring purposes provided no deadtime is introduced.
- The readout architecture should cope with multiple operation modes:
  - Spill synchronous data taken with data processing during the off-spill benefiting from the spills' low repetition rate.

  - Continuous data-taking (possibly at a lower sampling rate) with real-time zero suppression and lossless data compression on-the-fly.
  - Calibration mode with real-time averaging and histograms
  - "Scope" mode with a reduced data-set sampled at high-frequency for debugging operations

- To enhance the signal-to-noise ratio one should keep the interconnection lengths as short as possible to minimize the total capacitance seen at the preamplifier's input. To accomplish such a goal we propose to install the preamplifiers inside the LAr cryostat as well as the wire bias distribution system and the calibration network. High reliability of these components is a critical factor of the readout.

- The power consumption of the active components in cold operation has to be kept as low as possible to prevent (for example, boiling) compromising the performances of the detector.

The following sections will provide more details on the requirements mentioned above and will show possible implementations that address the related issues. The design proposed has roots in already existing projects (e.g. ICARUS, ILC-CALICE) with the aim of implemention with the latest, more cost effective technology that would allow at the same time more flexibility and better performance.

We want to emphasize hereafter that the readout architecture, while optimized for the experiment of this proposal, features flexibility in operation, versatility, easy adaptability and intrinsic scalability so to make it an attractive and cost effective possibility for larger scale R&D programs and experiments.

4.4.2 LAr TPC Signals

When the full transparency condition is met – see Eq. 4.22 – all the ionization electrons along the track will drift toward and will be collected by the Y-plane wires.

The electron drift induces on each wire (including the ones in the collection plane) a current signal given by 4.24 and 4.25:

$$i = -eE_w \bullet v_{drift} \tag{4.24}$$

where E_w and v_{Drift} are the weighting field and the drift-velocity of the electrons. Equation 4.24 is a direct consequence of the reciprocal theorem [75]. The total charge induced on the wires is the integral of Eq. 4.24. For collecting wires this corresponds to the charge effectively collected by the wires i.e. for the configuration represented in Fig. 4.26 (i.e. 100% transparency), the total charged produced by the ionizing track in the interval (-d/2, d/2) around the x-coordinate of the collecting wire (d being the wire pitch).

These considerations drive us to define the "signal standard" to be used as a reference. By signal we mean the total charge generated and fully collected on a sensing wire (assuming recombination but not attachment which will be considered separately, nor diffusion) by a minimum ionizing particle traveling on a plane parallel to the one defined by the sensing wires and perpendicular to the direction of the collecting wire itself.

$$Q_{generated} = \langle \frac{dE}{dx} \rangle d \frac{1}{W} \approx 2.1 \times 10^6 \frac{.3}{23.6} \approx 27ke^- \tag{4.25}$$

$$Q_{collected} = Q_{generated} R_{recomb} \approx 0.727ke^- \approx 18ke^- \tag{4.26}$$

where d is the wire pitch, R_{recomb} is the recombination factor as in Eq. 4.13.

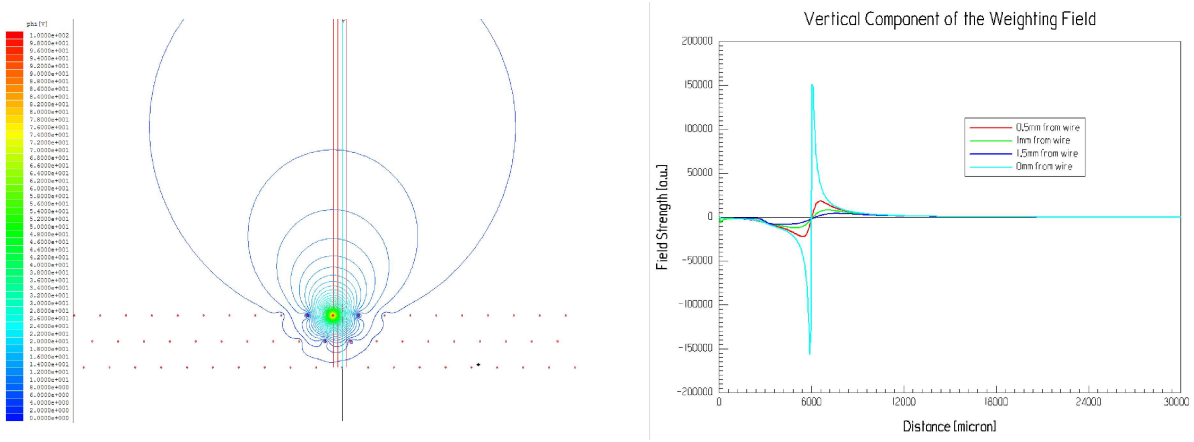

Figure 4.30: Left – Weighting field on the wire of the 1st induction plane. Right – Projection of the weighting field on the straight lines shown at left. The voltages on the wires are set to 100V.

Signal Simulations by Maxwell-2D

The weighting field is calculated by setting a unit voltage on the wire of interest and shorting to ground all the others. Maxwell-2D maps the weighting field and the current induced can be calculated by projecting the field on the drifting direction which in this analysis is approximated by straight lines (as well as by the fact that the drift velocity is kept constant). Figures 4.30 through 4.32 show the weighting fields (left plots) and their component along the drift direction (right plots). The latter ones are equivalent to the induced currents: the horizontal axis corresponds to the drift time with a scale factor of the drift velocity. The vertical scale is actually in unit of V/m (again with the same scale factor).

Figure 4.33 shows the maximum induced current on the induction planes as a function of the distance beween a point charge drifting toward the collecting wires and its perigee from the wire.

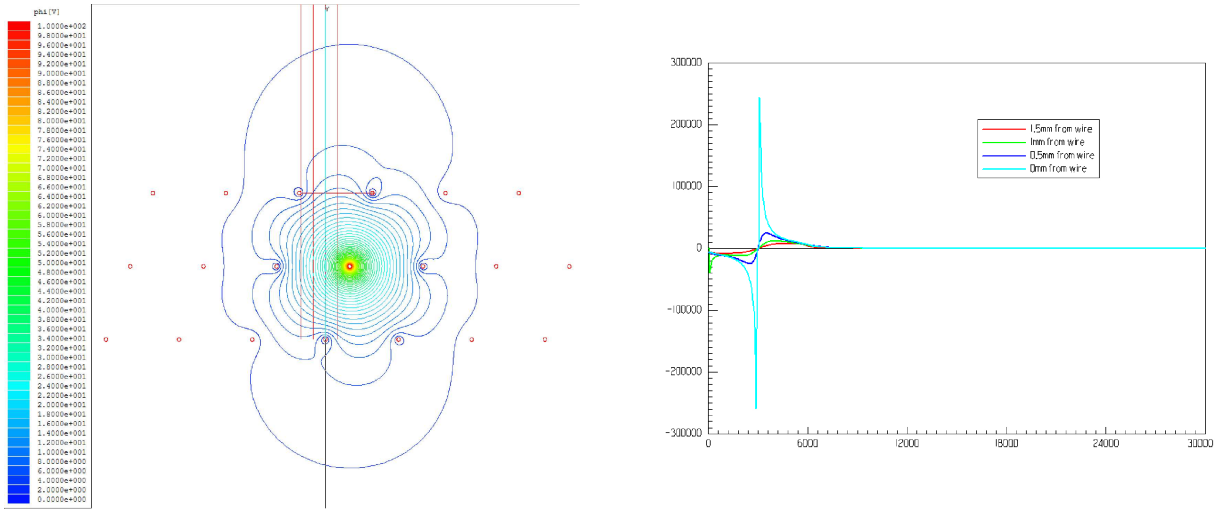

Figure 4.31: Left – Weighting field on the wire of the 2nd induction plane. Right – Projection of the weighting field on the straight lines shown at left.

Signal Simulations by Garfield: Effects of the Electronics

To simulate a realistic detector response we used Garfield specifying a drift-velocity table as function of the drifting electric field from [76]. Garfield is only a 2D-simulator. It cannot simulate wire planes at an angle. Therefore we used two geometries: one with the wires on the 3 planes aligned and one where the 2nd induction plane wires are offset by half the wire pitch with respect to the other 2 planes. To simulate the electronics readout we numerically convoluted the current signals computed by Garfield with a transfer function given by a charge-preamplifier with response in the frequency domain:

$$H_{preampl}(s) = \frac{1}{s}\frac{1}{1+s\tau_0}\frac{s\tau_1}{1+s\tau_1} \tag{4.27}$$

and by a shaper being a simple (RC)-(CR) with time constant τ=1μs.

The time constants of the charge preamplifiers are respectively τ_0=50 ns, the rising time of the preamplifier (detector capacitance and preamplifier input impedance), and τ_1=50μs, its decay time given by a resistive term on the feedback.

Figures 4.34 and 4.35 show the shaper output signals for the 2 simulated geometries:

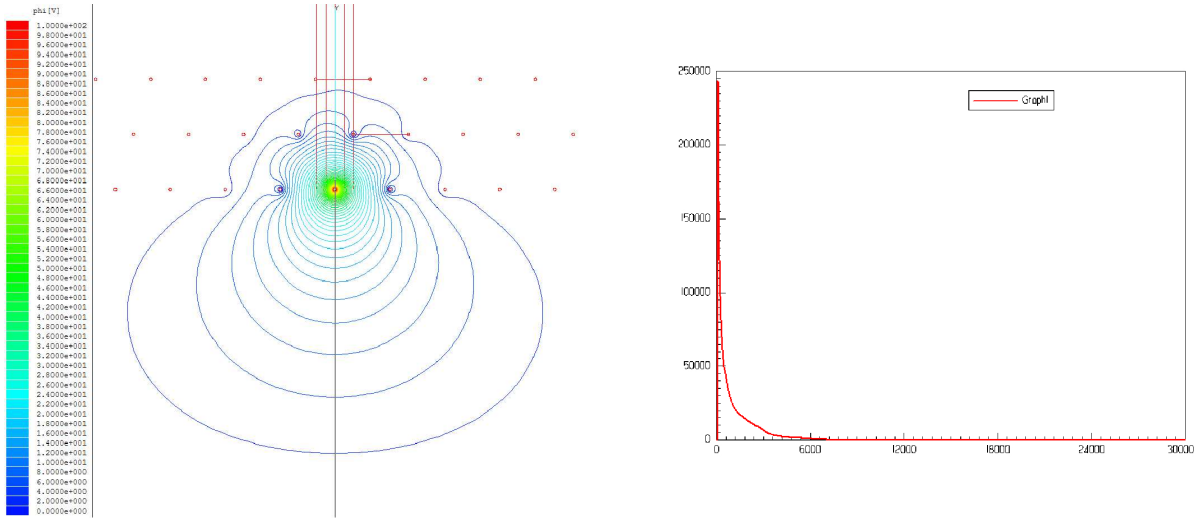

Figure 4.32: Left – Weighting field on the wire of the collection plane. Right – Projection of the weighting field on the straight lines shown at left.

5x5 sense wires on 3 planes, wire 13 being the collecting wire, wires 3 and 8 on the two induction planes being the wires directly above the collecting one as shown in the Figures.

In both Figures the track simulated is a uniformly ionizing horizontal straight line segment (-d/2, d/2), d being the wire pitch. The waveforms are normalized to the amplitude of the signal on the collecting wires so as to have a direct comparison with the 18k electron signal assumed as convention in Eq. 4.25. As it will be shown in the following section a S/N ratio of about 20-30 can be achieved with analog front-end at cryogenic temperatures. On the induction planes the signal is approximately $\times$ 5-7 above the noise while already the first neighbor wires are at approximately the same level.

4.4.3 Electronics Noise

The signal to noise ratio of the detector is determined by:

- Random noise sources associated with the readout electronics.
- Detector (wire) capacitance.

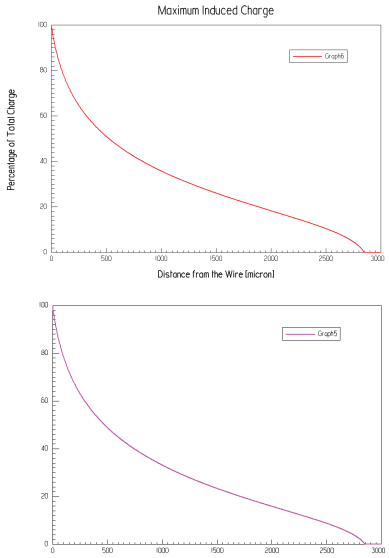

Figure 4.33: Maximum induced charge as a function of the distance between a point charge and its perigee from the wire in the 1st induction plane (top plot) and the 2nd one (bottom plot).

- Capacitance of the connections between the detecting wire and readout electronics.
- Noise sources associated with the detecting wire resistance and the resistance of the connections.

Wire Capacitance

The capacitance of a single wire of radius a, part of a plane of wire pitch h and separated by a distance s from the other wire planes can be approximated by [77]:

$$C = \frac{2\pi\epsilon_0\epsilon_r}{\pi h/s - log(2\pi a/s)} \tag{4.28}$$

For 3 mm spacing, 3 mm separation and 150 micron diameter C=18 pF/m. This result is consistent with results from ICARUS which measured C=20 pF/m for the first

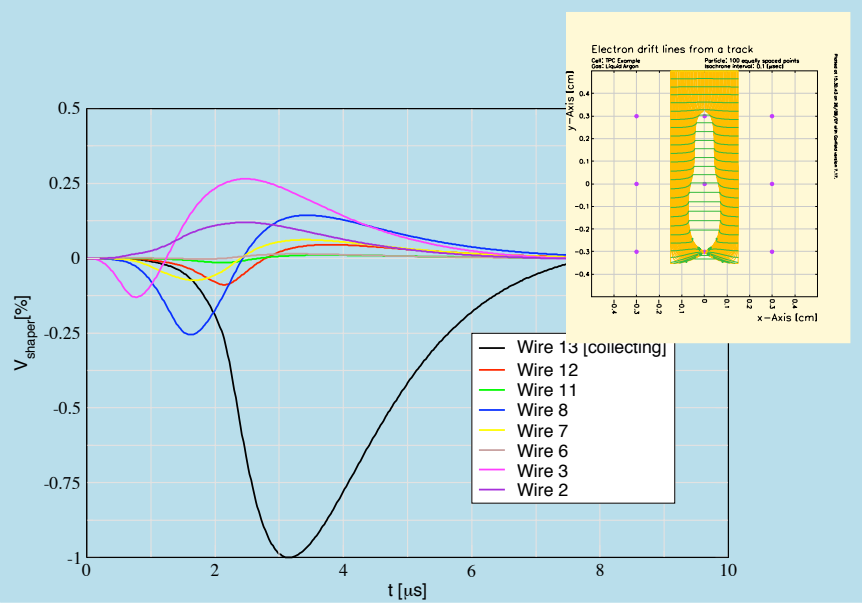

Figure 4.34: Detector response to track segment with a uniform distribution of ionization charges measured at the output of a (RC)-(CR) shaper with 1μs time constant. Detector geometry simulated is 3 wire planes with all the wires aligned vertically. Simulation by Garfield v.9.

and last plane and 21 pF/m for the middle induction plane. For a 5 m wire length the wire capacitance will amount to 100 pF.

Connection Capacitance

For Kapton-insulated cable (ϵ_r=3.6 which yields a propagation time of t_d=6.6 ns/m) the capacitance per unit length is C=t_d/Z_0 =132 pF/m for 50 Ω cable.

Assuming a 2 m length from the wire to the top of a feed-through, the connection capacitance will amount to 260 pF, considerably larger than the detector capacitance.

This contribution can be reduced by shortening the length of the connection. By placing the readout electronics inside the cryostat as near as possible to the readout wire, the connection capacitance could be reduced to as little as 20-30 pF.

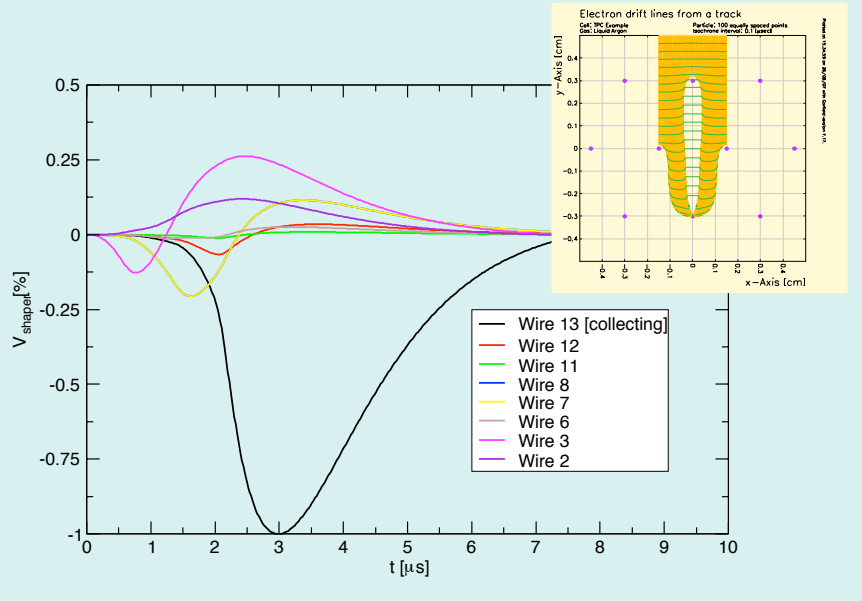

Figure 4.35: Same as Figure 4.34 with a slightly different geometry: wires on the 2nd plane are offset by half the wire pitch. Minor difference in the output signal amplitudes.

Total Detector Capacitance

The total capacitance as seen by the readout electronics is the sum of the wire and connection capacitance. For the case of external readout electronics:

- Wire Length: 5 m →100 pF
- Connection: ∼2m → 260 pF

which yields a total, capacitance C_{total} ≈400 pF including strays due to connectors. For the case of readout electronics placed inside the cryostat within the LAr:

- Wire Length: 5 m →100 pF
- Connection: <30 cm → 50pF including connector stray capacitance

which yields a total, capacitance $C_{total} \cong$ 150 pF including strays due to connectors.

Equivalent Noise Charge

The noise-to-signal ratio associated with random noise sources in the readout electronics can be expressed as an *"Equivalent Noise Charge"* (ENC).

There are two main noise sources: a series one (represented by the equivalent noise voltage source e_n) and a parallel one (represented by the equivalent current noise source i_n).

$$ENC = \frac{1}{q}\sqrt{\frac{1}{2}e_n^2 C_T^2 \frac{A_s}{t_p} + \frac{1}{2}i_n^2 A_p^2 t_p + C_{\frac{1}{f}} A_{\frac{1}{f}} C_T^2}(r.m.s.electrons) \qquad (4.29)$$

Figure 4.36 is a schematic diagram of the electronics readout chain showing the noise sources associated with the amplification process.

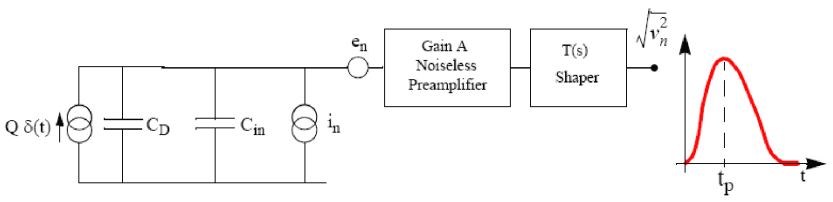

Figure 4.36: Schematic diagram of the electronics readout chain with associated noise sources.

A (noiseless) Dirac delta of detector charge would be amplified and shaped (to limit the bandwidth and improve the S/N ratio). At the measurement time t_p the noise added by the amplification would cause an error in the measurement which can be described by its probability distribution. Calculation shows that it has a gaussian distribution with variance $s(e_n, i_n)$. This variance can be referred to the input as the equivalent noise charge (ENC), defined as the *current that, delivered as an impulse at the preamplifier input, will generate at the output a signal of amplitude* s.

$$ENC = \frac{1}{q}[\frac{1}{2} \cdot e_n^2 \cdot C_T^2 \cdot \frac{A_s}{t_p} + \frac{1}{2} \cdot i_n^2 \cdot A_p \cdot t_p + C_{\frac{1}{f}} \cdot A_{\frac{1}{f}} \cdot C_T^2]^{\frac{1}{2}} \tag{4.30}$$

From Equation 4.30 it is apparent that the series noise gives a contribution proportional to the total capacitance. To minimize the noise it is therefore important to minimize the detector and connection capacitance. As depicted in Figure 4.37 the white series noise gives a contribution which decreases with longer measurement time, while the white parallel noise contribution increases. The 1/f series noise contribution is independent of shaping time, and this remains an accurate approximation also for "pink" noise sources which are not strictly inversely proportional to frequency.

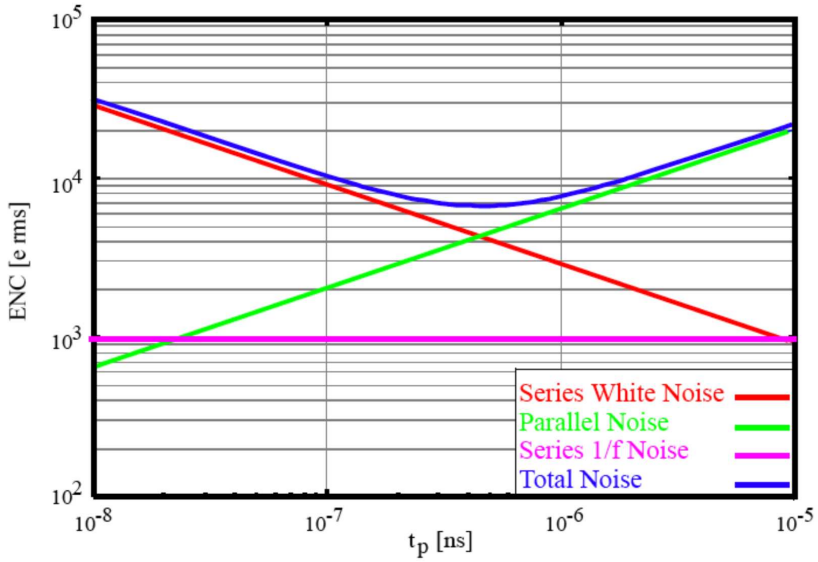

Figure 4.37: Series white, parallel white and series 1/f noise vs. measurement time. The white series noise decreases for longer measurement time, while the white parallel noise increases. The 1/f series noise is independent of measurement time. The parameters used are: e_n=0.5 nV/$\sqrt{Hz}$, i_n=$\sqrt{4K_BT/R_F}$, C_{TOT}=1 nF, e_n=1kΩ and the filter is CR-RC^2

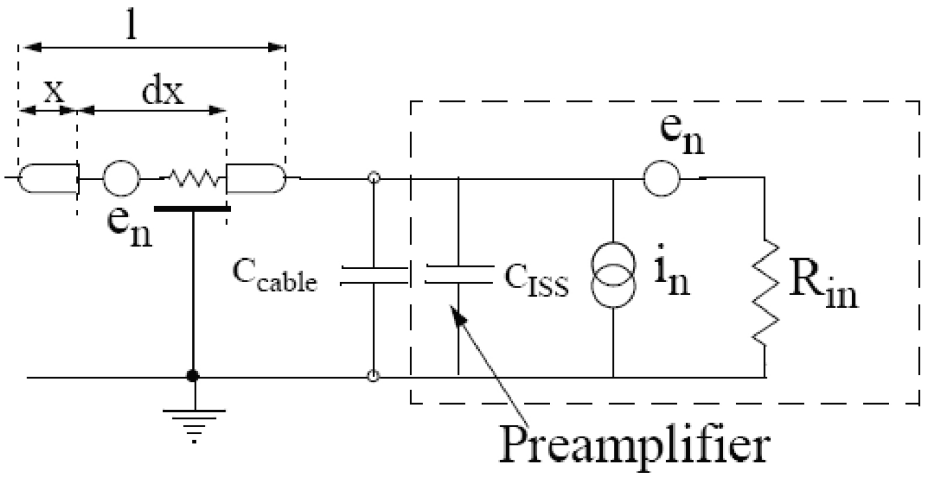

Figure 4.38: Schematic diagram of the R-C diffusive wire

Other Noise Sources: Wire "Diffusive Line" Noise

The equivalent noise resistance of a low noise device with e_n = 0.4 nV/$\sqrt{\text{Hz}}$ is only 10Ω: any resistance in series with the input increases the noise. The stainless steel wire has a resistivity ρ= 720 $\mu\Omega$·mm at 20^o C, AISI 304 SS, which drops to ρ=640$\mu\Omega$·mm at 90K [78]. Along with the capacitance to ground (i.e. "low impedance" nodes) this resistance constitutes an R-C diffusive line as shown in Figure 4.38.

For a 150μm wire the DC resistance amounts to about 40Ω/m which would add too much noise. Fortunately gold, which can be easily plated onto the stainless steel has a resistivity of less than 1% than stainless steel at 90K (5.6 $\mu\Omega$mm at 90K), and a relatively thin plating can easily reduce the wire resistance. For example a 1μm Au plating on a 150μm stainless steel wire would reduce the resistance to about 9Ω/m, and a 3μm Au plating to about 2Ω/m.

Figure 4.39 shows the wire noise contribution assuming a wire resistance of 8Ω/m and a capacitance of 20pF/m (red trace), along with the preamplifier noise (blue trace) and total noise (green) for the Microboone cryogenic electronic case. The wire noise contribution is less than 5% of the preamplifier noise.

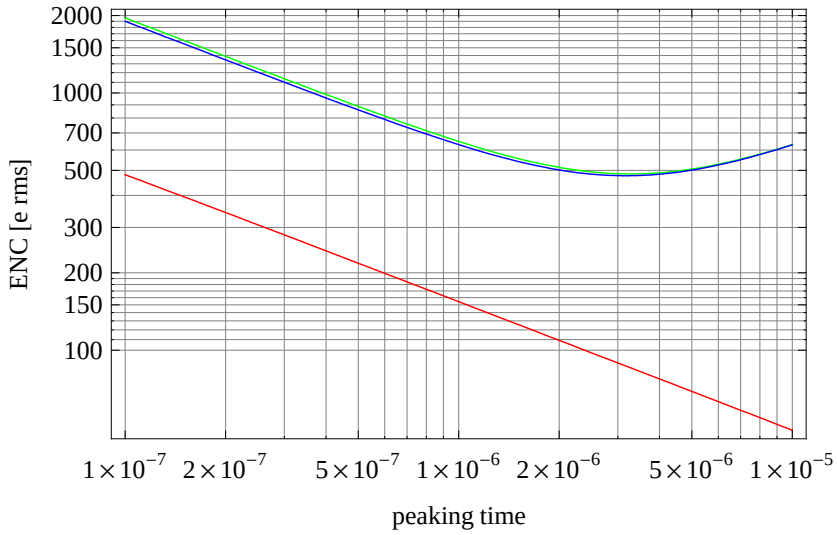

Figure 4.39: Wire noise contribution assuming a wire resistance of 8Ω/m and a capacitance of 20pF/m (red trace), along with the preamplifier noise (blue trace) and total noise (green) for the Microboone cryogenic electronic case. The Au plated SS wire length is 5m, and its noise contribution is less than 5% than the preamplifier noise.

Other Noise Sources: Microphonics

At long shaping time microphonism introduces additional noise:

- Wires vibrate, causing variation in capacitance.
- Piezoelectricity of ceramic capacitors.
- Vibrations in connections changes capacitance and inductance.
- Changes in resistance in imperfect or degraded connections.

Noise comparison for External and Internal Electronics

Let us compare the following two cases:

1. "Warm" electronics located at the feed-through.

2. "Cold" electronics located as near as possible to the readout wire.

Let us assume the case described in Sec. 4.4.3:

- Cable capacitance: 130 pF/m (50 Ω characteristic. impedance line) → 260 pF for 2 m cable run.

- C_D 100 pF (5 m wire @ 20 pF/m).

- C_{stray} 40-50 pF (due to connectors, backplanes etc...).

In case of external electronics, the total input capacitance contributing to noise would amount to 400 pF, while eliminating the long cable run connecting the wire to the feedthroughs the input capacitance could be reduced to about 150 pF.

Figure 4.40 shows the comparison of electronics noise for "cold" and "warm" electronics. At 1 μs peaking time the ENC for the "warm" case is 1200e r.m.s., which could be reduced to about 600e r.m.s. for the "cold" case.

Other advantages of a cryogenic amplifier are:

- Avoids transmission of very low level signals (better "Faraday cage")

- At the cost of complicating the electronics (MORE POWER!), could reduce the number of feed-throughs by data reduction ("sparsification") in hardware

- Reliability (if properly designed and built)

Disadvantages include:

- Bubbling

- Cryogenic load due to preamplifier heat dissipation

- Careful manufacturing necessary to insure LAr purity

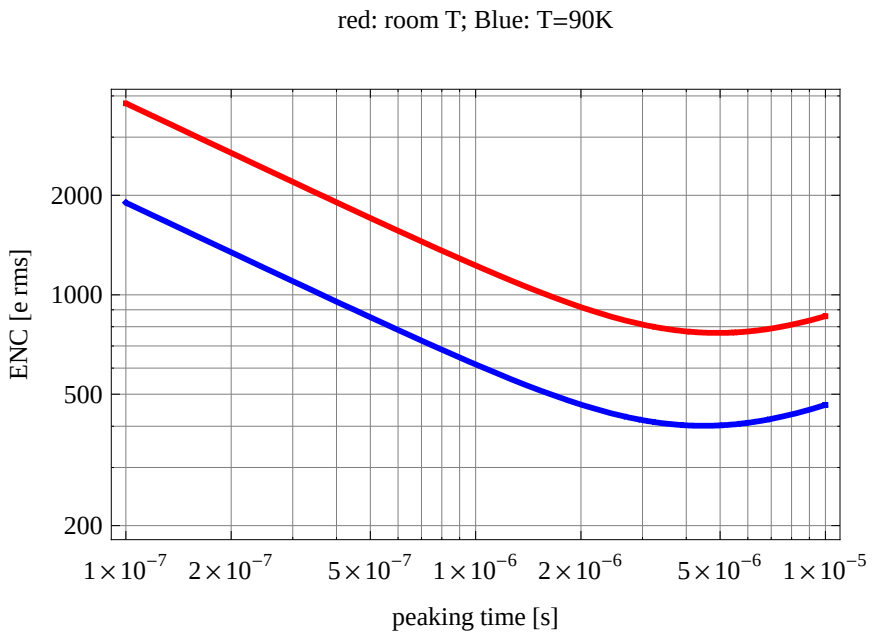

Figure 4.40: ENC vs. peaking time comparison between "warm" and "cold" Front-End.

4.4.4 Dynamic Range Considerations

The dynamic range is determined on the low side by the electronics noise. On the high side there are no strong requirements from physics. The ionization density in an electromagnetic shower is relatively low even in the shower core at the peak of the longitudinal development. Also the low energy recoil proton – whose detection could ease the e/π^0 identification by vertexing – dE/dx is limited as shown in Figure 4.41. The energy loss, the range and the maximum energy released in 3 mm of LAr is shown in the picture. The maximum energy released by a slow proton in 3 mm is about x15 above the signal. Protons traveling parallel to the wires would release higher ionization charges. The proton spectrum from 500 MeV neutrinos, for example, is shown in Figure 4.41.

The combination of maximum signal size and charge loss across the detector imply a required dynamic range of ∼150. With a minimum signal/noise ratio of 10, a 12 bit readout is needed.

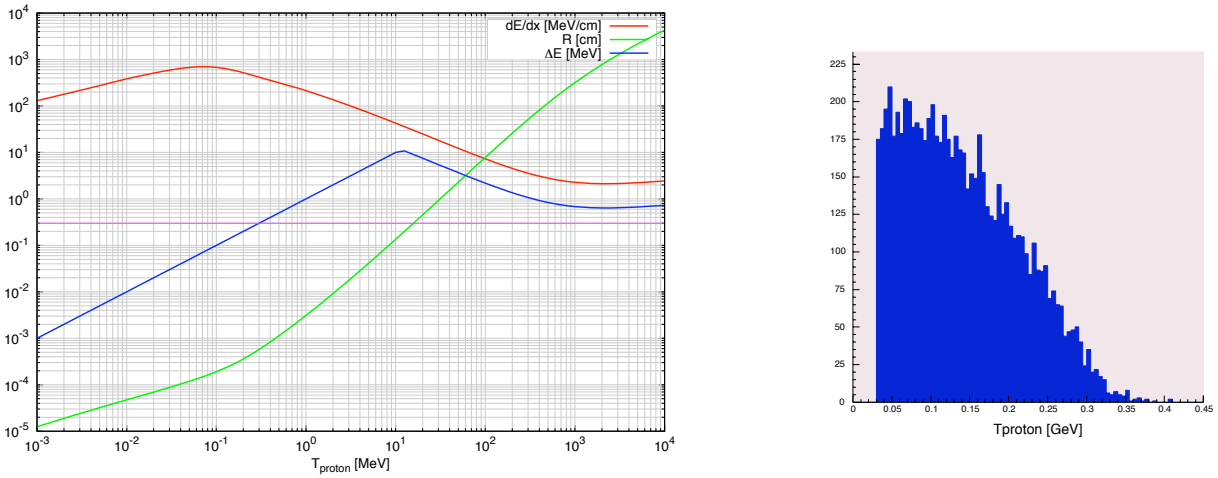

Figure 4.41: Energy loss, range and energy released in 3 mm of LAr by protons (left). Proton energy spectrum from a 500 MeV neutrino (right).

4.4.5 Sampling Rate Considerations

Figure 4.42 represents the spectrum of the signals shown in Figure 4.34. Only 1% of the signal spectrum is above 2 MHz. To keep aliasing below that level a sampling rate of 4-5MSPS is desired. More sampling could be usefull to suppress further noise.

4.4.6 Cryogenic Preamplifiers

Cryogenic preamplifiers capable of working at LAr temperature were first employed in the Helios-NA34 experiment in the late 1980's. They have been extensively studied during the RD phase of the GEM SSC detector and ATLAS LAr calorimeter.

To date, the two major installations have been the NA48 experiment, which uses a JFET based preamplifier initially developed for GEM (13,000 channel, ceramic hybrid) and the ATLAS ENDCAP calorimeter which uses a GaAs based monolithic circuit.

Figure 4.43 depicts a JFET based preamplifier developed at BNL for the GEM de-

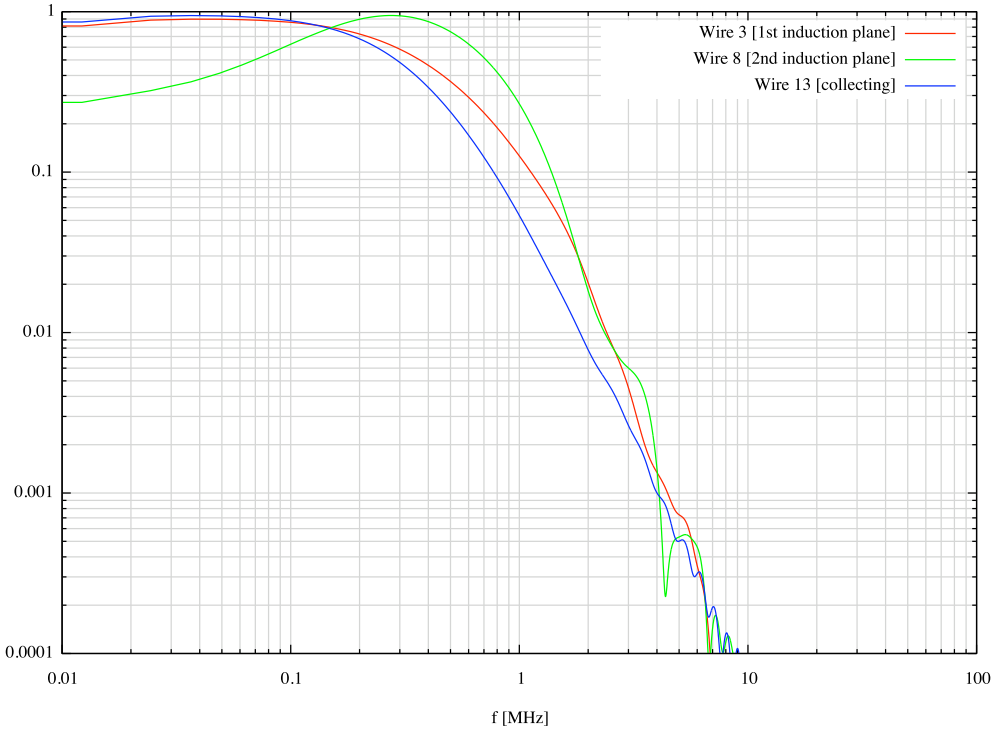

Figure 4.42: Signal spectrum (see Figure 4.34).

tector. The bottom plot of the figure shows SPICE simulations of preamplifier gains at different nodes.

Figure 4.45 shows measurements of ENC as a function of temperature for IPA3 L and H preamplifiers. The measurements - at the peaking time value needed for the SSC-GEM LKr calorimeter - have been carried out with CD = 500 pF detector capacitance and bipolar shaping obtained from an (RC)2 -(CR)2 filter.

Table 4.4 summarizes the characteristics of the IPA3 preamplifier for fast calorimetry applications.

Reliability: Previous Experience

The reliability for the two major installations of cryogenic preamplifiers which have operated for an extended time (ATLAS Hadronic Endcap calorimeter is not operational yet)

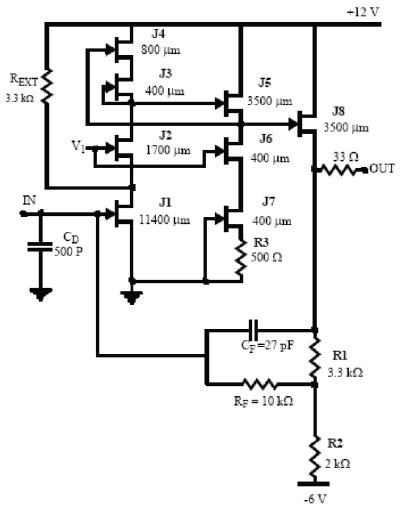

Figure 4.43: Schematic of JFET based preamplifier capable of cryogenic operation.

is summarized below:

- Helios-NA34
  - Preamplifiers in LAr: 576
  - Dead preamps: 1 in 4 years, multiple cooldowns
- NA48
  - Preamplifiers in LAr: 13,000
  - Operated at very high voltage
  - Dead preamplifiers: @ 50, in a HV accident in 1998. Negligible failures after that.
  - Always kept at cryogenic temperature

While requiring a careful choice of component and high-reliability assembly (a ceramic hybrid with co-fired traces and surface mount components is the preferred configuration for discrete-based cryogenic preamplifiers), the reliability could be very good indeed.

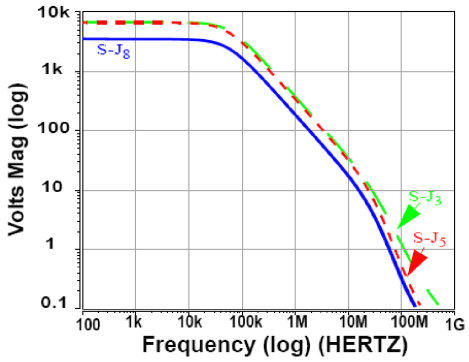

Figure 4.44: Performance of JFET based preamplifier. The SPICE plot is the gain of the preamplifier at various nodes. The input-output gain is the one measured on the source of J8.

This is partly due to the cryogenic environment which slows components aging processes and of course, effectively cools the electronics. Past experience shows that the major failure cause, especially in the development stage, are thermal stresses which might break connections or components (especially during rapid cool-downs).

4.4.7 Readout Architecture

The read-out electronics are responsible for processing and temporary storage of the charge information collected by the approximately 12,000 wires during the electron drift time. The signal from each wire is pre-amplified, shaped and then continuously sampled at a programmable rate up to 20 MSPS. The digitized outputs from the analog to digital converters are passed to an FPGA for data processing and data reduction. The results are then stored in local memory until the DAQ system retrieves the information for that spill. A signal synchronous to the incoming beam spill starts the recording sequence, while a programmable fixed delay starts the DAQ transfer.

Figure 4.46 depicts the block diagram of a single readout channel as just outlined: the detector element is represented by its equivalent capacitance in parallel to the current

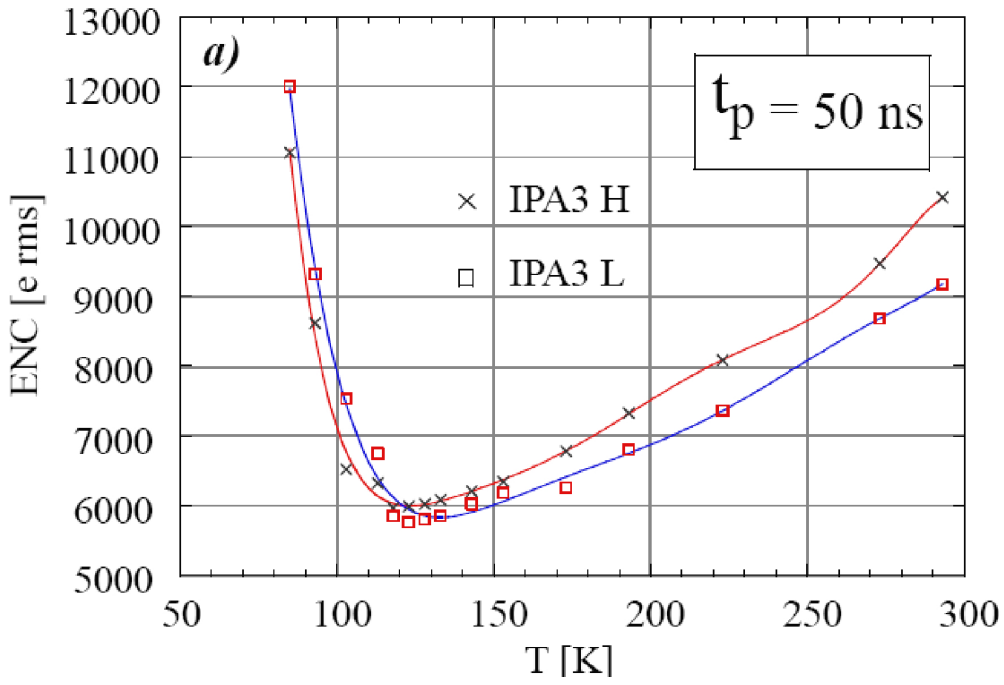

Figure 4.45: ENC vs. temperature for IPA3-L and IPA3-H preamplifiers.

source equivalent to the event generator. The detector is biased locally through a distribution network mounted in proximity of the preamplifier. The bias distribution network includes in-line decoupling ceramic capacitors to isolate the preamplifier inputs.

Figure 4.48 is a similar block diagram with highlighted details on the analog front-end: the detector elements are terminated to a short pigtail cable on a wire holder printed circuit board. The interconnection lengths are minimized to limit the contribution to the total capacitance seen at the preamplifier input. To enhance the signal-to-noise ratio the preamplifiers are mounted on printed circuit boards inside the cryostat. In proximity of the preamplifiers a calibration network will allow injection of precise signals into the preamplifier inputs. The calibration signals will be driven by external boards installed in the readout crates on the detector.

The readout electronics are then organized in readout crates mounted on racks installed in a platform built on the top of the cryostat as depicted in Figure 4.48, so as to

Table 4.4: IPA3 measured characteristics.

Parameter		L-Type	H-Type
Input Device		NJFET, W=11400μm, L=5μm	
Open-loop Input Capacitance		50 pF	40 pF
Power Dissipation		80mW	
DC gain A_o	Zout=10kΩ	82 dB	75 dB
	Zout=100Ω	76 dB	70 dB
Rise Time (C_D=500pF, C_F=33pF)		15ns	
Noise Voltage/ $\sqrt{Hz}$ (f>1kHz)	T=300K	0.6	0.7
	T=120K	0.4	0.4
ENC [e- r.m.s] with a bipolar shaping (RC)2-(CR)2 @ tp=50ns		ENC=1200+18 C_D	ENC=1100+21 C_D

have the cable lengths not exceeding 1-1.5 m approximately.

A single read-out crate accommodates 768 channels which is the number of wires that connect through a single feed-through flange. There are 12 flanges in total and therefore 12 readout crates for the entire detector. Within a single read-out crate, which is a standard Advanced TCA crate, there are 12 front-end boards which each process 64 channels. The front end boards consist of shaping amplifiers, digitizers, an FPGA for the data processing, memory for local storage and a gigabit ethernet link to connect to the DAQ system. A block diagram of a possible implementation of the readout board is shown in Figure 4.49.

Receiver, Shaper and ADC

At the receiving end, the output signals of the preamplifiers are fed into shaping amplifiers assembled on custom made PCBs installed on the rear side of the readout crates. The shaper topology could be simply a RC-CR stage with time-constant of $\sim 1\mu$s even though this has to be optimized. In particular, the induction plane readout may need a 2nd stage of integration to take into account the bipolar nature of their signals.

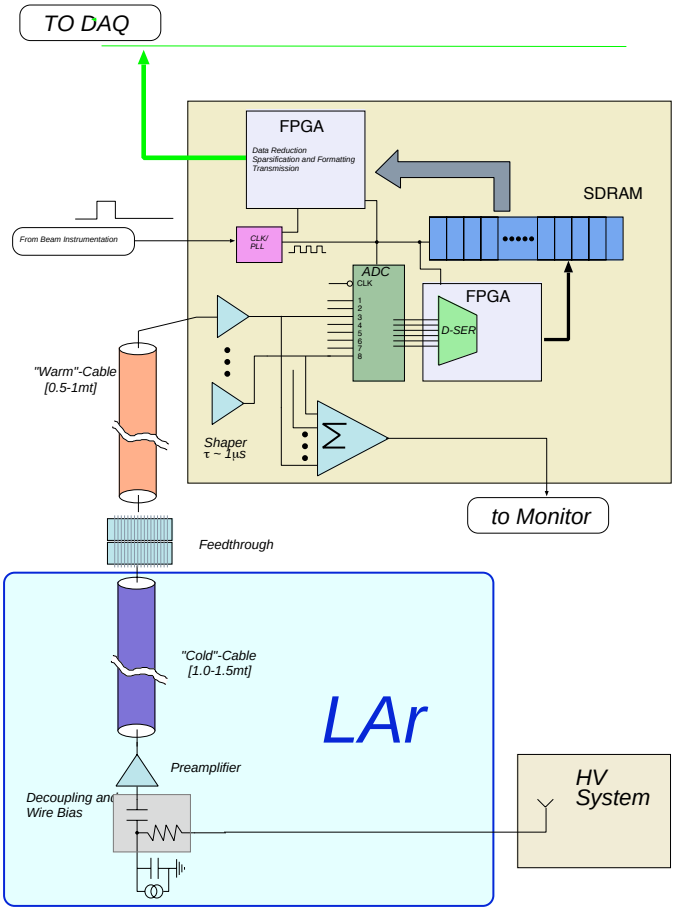

Figure 4.46: Single readout channel information flow

The availability of cheap, fast, multichannel analog-to-digital converters (ADC) will permit the use of a dedicated ADC per channel. This eliminates the need for analog multiplexers and all their inherit problems. A 14 bit, 10-50MSPS ADC will provide enough dynamic range and, by oversampling the signal, some process gain may also improve the signal-to-noise ratio. To increase the density of channels per front end board an multichannel ADC will be choosen. These multichannel ADCs also provide high speed LVDS serial output streams, which simplifies the number of connections needed to the FPGA.

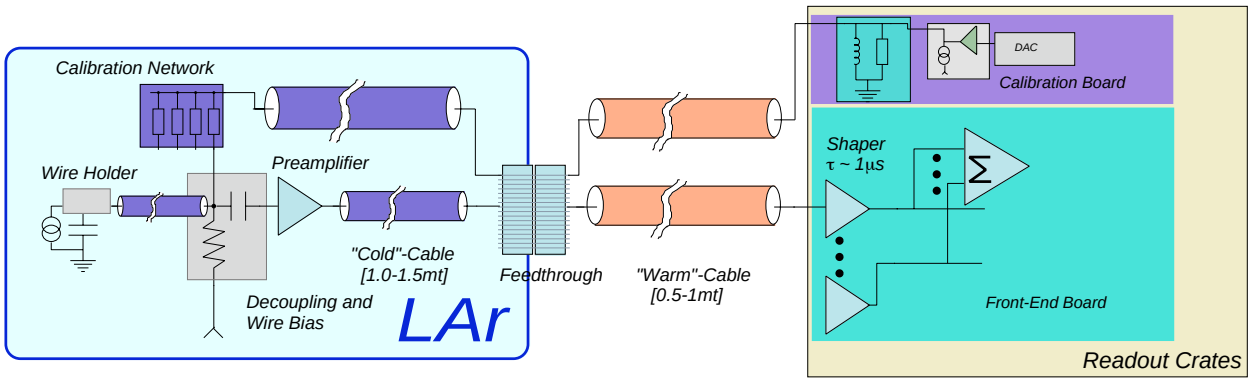

Figure 4.47: Analog Front-End Readout channel and calibration

Data Processing on board

After digitization, all the digital outputs from the ADC's are sent to an FPGA for further filtering, data processing and reduction, temporary buffering and finally interfacing with the DAQ system through a gigabit ethernet link. A single Xilinx Virtex FPGA with embedded PowerPC processor can accommodate this task for 64 channels.

The FPGA connects to the ADC's via high speed low voltage differential signaling (LVDS) serial links. Each serial link runs at 280 Mbits/sec for a total data input rate of 2.24 Gbytes/sec for the 64 channels. The LVDS serial link is preferred over a parallel interface because it lowers pin counts, eases routing density, increases noise immunity and lowers power consumption on the printed circuit board when compared to a parallel bus.

After the serial data has been received into the FPGA and converted to parallel words, the data is immediately passed to local DDR DRAM memory where it is temporerly buffered for the ∼2-3 ms drift time following the 1.6μs beam spill. The data is first stored and then processed from the local memory during the dead time between spills.

When the beam spill has completed, processing of the data can begin. It is during this large dead time that the data set for the beam spill will search for events; only the valid data will be forwarded on to the DAQ system. Without this data reduction, the total

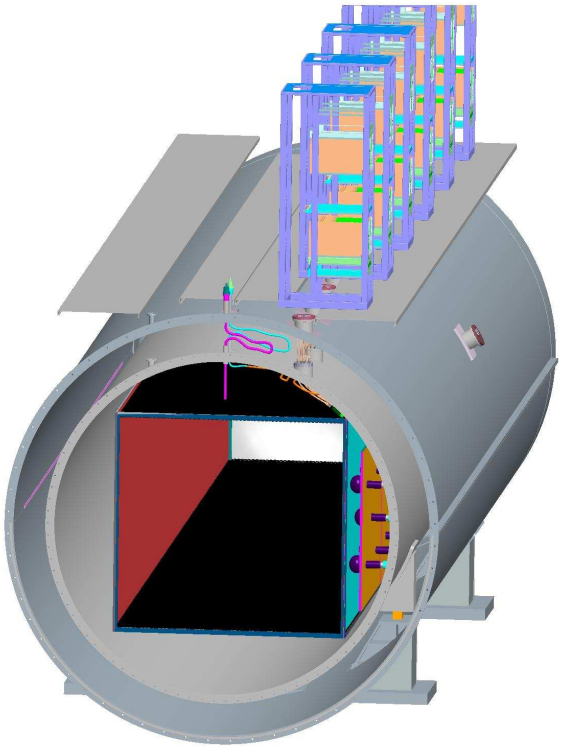

Figure 4.48: Isometric view of the cryostat showing on-detector readout crates next to the vacuum feed-through.

throughput required, conservatively assuming a 5 Hz spill rate and data recording time of 5 ms per spill, would be (20 MS/s · 5 ms · 14 bits · 5 Hz) = 875 kbytes/sec per channel. The total data rate per front end board (64 channels) would then be 56 Mbytes/sec and for the entire detector (12,000 channels) would be 10.5 Gbytes/sec. Clearly this would be hard to sustain for the DAQ system (and most of the data is uninteresting anyway). The job then of the FPGA is to reduce the bandwidth by only storing data whose value is above some threshold along with some pre-trigger and post-trigger data.

To achieve this data reduction a technique similar to that used by the DAEDALUS chip for the ICARUS experiment would be used. They define what is called a region of interest (ROI) as a time window around a rising edge (hit). To identify a rising slope (hit), one computes the sums and differences of consecutive samples inside a time sliding

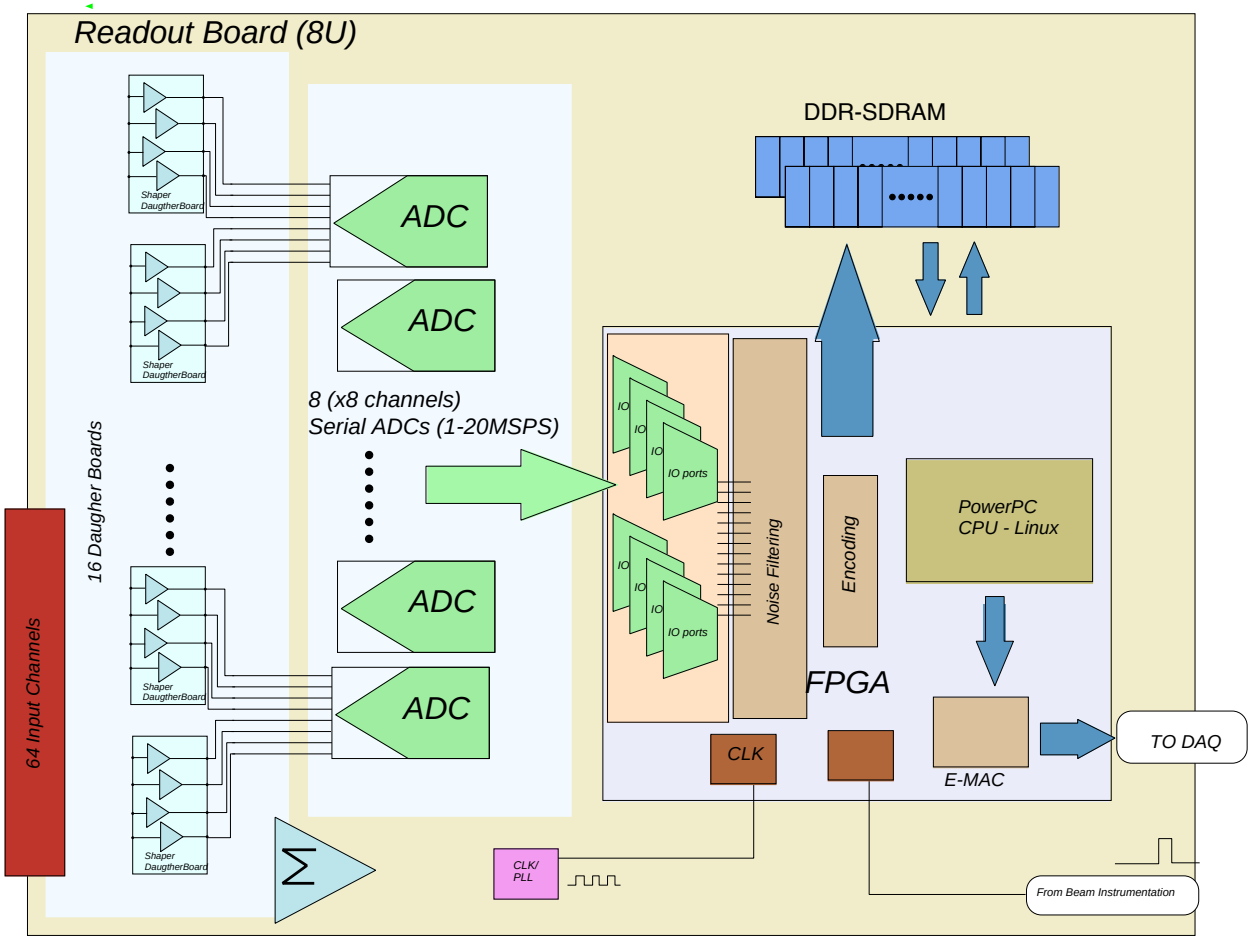

Figure 4.49: Block diagram of a possible readout board implementation

window. By using different programmable thresholds for these values, events can be found with near 100% efficiency. Once an event has been detected a programmable time window of samples around that event are tagged with a timestamp and forwarded to the DAQ system.

The FPGA can interface directly to the DAQ system because it includes an embedded PowerPC 405 processor and gigabit ethernet Media Access Controller (MAC). The only other external circuitry needed is an ethernet physical layer chip. The PowerPC chip can run a simple operating system which contains a TCP/IP stack. There are many choices for operating systems, from a very simple Xilinx MicroKernel all the way up to an embedded Linux system. The embedded processor interfaces directly with the FPGA

fabric to gather the data, create TCP/IP packets, and forward the information to the DAQ system.

Trigger and Clock interfaces

The readout board will house a high precision, low jitter oscillator that will be distributed over the different components for digitization, buffer and transfer to the DAQ. To synchronize with the other boards in the system it will have an external clock interface with a programming logic to switch from one to another.

In normal mode operation upon the arrival of a trigger signal, i.e. the start of spill, the data are digitized and buffered on the local memory. However, the board will be implemented so that it can be operated in free running mode. In this case an internal logic will define a trigger condition and an output signal will be generated and available on the front-panel of the board.

Trigger Detectors (PMT) Readout

The same readout board can be optimized to readout as well the PMTs. A trigger signal in this case should be taken in the order of $\sim 2\mu$s at the latest, which we believe is possible thanks to the high sampling rate of the ADCs proposed. The flexibility and the excellent performances of the recent FPGAs would render us likely to implement TDC locally in the FPGA as in [77] for example.

4.4.8 Readout Mapping

Signal Mapping

The actual wiring area on U, V and Y wire planes is 11660 mm (Z axis) x 2417.3 mm (Y axis), with 3.036 mm wire pitch. There are 3840 readout signal channels on the Y

Table 4.5: Readout channel mapping in the feed-throughs.

feed-through	Y Plane		U Plane		V Plane	
	64-pin Row	Channels	64-pin Row	Channels	64-pin Row	Channels
Standard feed-through (10)	6	384	3	192	3	192
Special feed-through 1	0	0	10	640	0	0
Special feed-through 2	0	0	0	0	10	640
Total	60	3840	40	2560	40	2560

plane and 2560 readout signal channels on each of U, V planes. On U and V planes, 1920 channels are read out along the Z direction, and 640 channels are read out along the Y direction. The total number of readout signal channels for the full detector is 8960.

There are 12 feed-throughs for signal readout, monitoring, calibration and power distribution. Each feed-through has flanges with two pin carriers (8+7 rows) and each pin carrier row has 64 pins. 10 standard feed-throughs have the same configuration to read out signals from the top of the three wire planes along the Z direction, and 2 special feed-throughs are used to read out signals from U and V plane along the Y direction respectively. Table 1 shows how readout signals are mapped in each feed-through.

In each standard feed-through, 384 channels on Y plane, 192 channels on each of U, V planes, total 768 channels of read out. This covers 1160 mm along the Z direction of the wire planes. There are 2 print circuit boards with cold preamplifiers mounted on for each standard feed-through. Each print circuit board houses wire connections and preamplifiers of 384 channels. A total of 12 64-pin carrier rows are used for signal readout.

In the special feed-throughs, a total of 64 channels are read out, which covers 2240 mm along the Y direction of the U or V plane. There are 4 print circuit boards for each special feed-through, each board houses wire connections and preamplifiers of 160

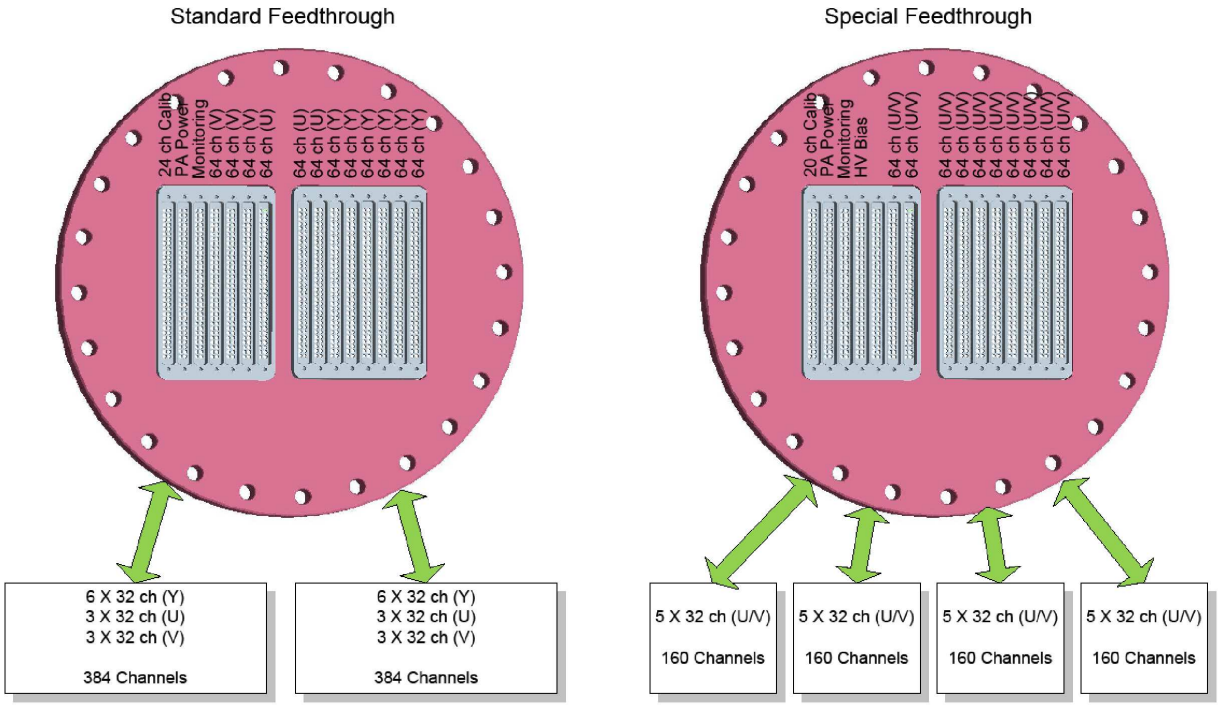

Figure 4.50: Channel mapping of both the Standard (left) and Special (right) feed-throughs.

channels. A total of 10 64-pin carrier rows are used for signal readout.

Preamplifier Power and Wire Bias

Preamplifier power (+10V, -3V) is supplied from an external power supply with the signal cables passing the feed-through to the print circuit board in detector. Each standard feed-through has 768 readout channels. The total current for 10 V is 100 mW/ch x 768ch / 10 V = 6.144 A, -3 V is for preamplifier biasing. It consumes a very limited current. Considering the current transmission capability of a signal cable, 24 pins are used for 10 V, 8 pins for -3 V, the other 32 pins for power return. The transmission of the preamplifier's power occupies a single 64-pin carrier row. In the special feed-through, there are less channels (640) to be read out. A single 64-pin carrier row, the same as the standard feed-through, is used to supply power to the preamplifiers. Since the special

feed-through is mapped to 4 print circuit boards, each board has 6 lines for 10 V and 2 lines for -3 V, which provides necessary redundancy.

200 V is used to bias the first induction plane and -440 V is used to bias the collection plane. Since both voltages consume very limited current, one dedicated 64-pin carrier row in each of the special feed-throughs is used to distribute the HV to the wire planes. Two 64-pin carrier rows for HV biasing provide necessary redundancy.

Calibration Lines

Each calibration signal is used to pulse 32 readout channels. In the standard feed-through, there are 24 calibration pulses for 768 readout channels. In the special feed-through, there are 20 calibration pulses for 640 readout channels. So, one 64-pin carrier row is used to distribute calibration signals to print circuit boards in detector. In the standard feed-through, each calibration line is connected to every 6th wire on the Y plane, and to every 3rd wire on the U and V planes. In the special feed-through, each calibration line is connected to every 5th wire on the U or V plane.

4.4.9 Data Acquisition System

The data-acquisition system (DAQ) is comprised of 14 processor blades, one blade in each of the readout crates, plus 1 or more event building computers. Each of the processor blades is a standard off-the-shelf Advanced TCA module which communicates with the readout cards over the ATCA backplane using a gigabit ethernet interface. The processing blades are responsible for merging the data from the 12 readout cards and then buffering this data until the event building computers can accept it. The 14 processor blades are connected to the event building computers via a 16 port gigabit ethernet switch and a standard TCP/IP protocol. The architecture is scalable so the number of

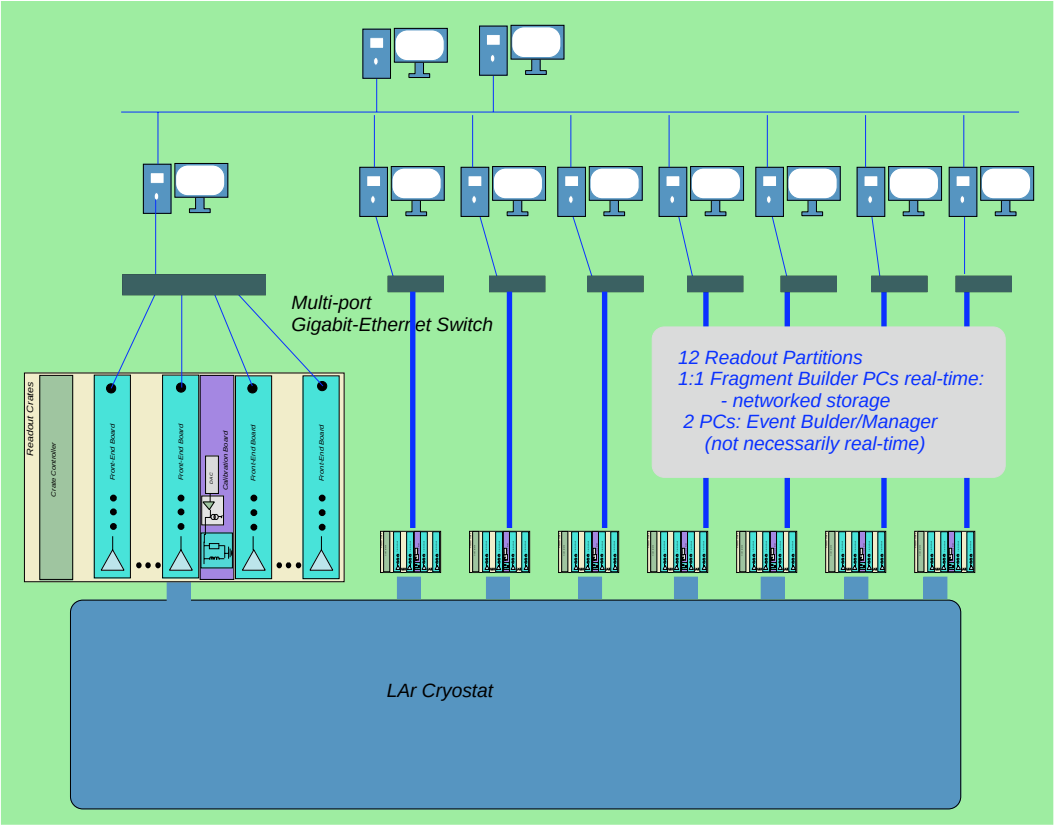

Figure 4.51: Possible implementation of DAQ based on G-bit ethernet point-to-point PC nodes as fragment/event builders.

event building computers can be increased depending on the time required to merge the fragments of the event and store them to disk or tape.

A possible implementation of the DAQ architecture is depicted in Figure 4.51. Point-to-point connections between the readout boards and the event building PCs are realized by G-bit Ethernet links. At a second level, few supervisory PCs regulate the I/O on storage media. For the software architecture, we are considering the adoption and adaptation of existing frameworks. A possibility could be the recent development within the ILC-CALICE collaboration [79].

4.5 Alternate Designs

The MicroBooNE detector described here is our baseline design. It both advances the R&D towards larger detectors while ensuring a design appropriate to achieve the physics goals. Other designs for the cryostat, field cage, and drift region are still under consideration. These options along with discussion of the relative merits of the designs, are listed below.

- "Soup Can" cryostat: A cryostat in the shape of a soup can sitting on its side, like the 5-100kton design, has been considered. In this design, the wire chamber would be hung inside the detector with a cylindrical field cage surrounding it. While this looks more like the 5-100 kton scale detectors, it is not clear what one can learn with this geometry beyond the baseline design. The open design questions for the large detector include chamber construction and feed-throughs, and purification system. All of these may be studied as easily in the baseline design as in the "soup can" cryostat. As well, with the "soup can" design, it is not clear where PMTs can be mounted.

- Wire Chamber planes: Hanging the wire chamber planes in the center of the drift region and drifting from both sides towards the wire planes has been considered. This configuration is like that in designs for the large detectors. While the drift length is shorter, easing purificaiton requirements, the number of channels doubles and therefore the cost increases. As cold electronics will also ease the purification requirements, the shorter drift and increase in channel count does not motivate this design. However, it may be useful to test the hanging mechanism for this double plane system as will be implemented in larger detectors.

- LAr storage vessels: In the baseline design, one LAr storage vessel hold the 170 tons of Liquid Argon prior to filling of the detector. In this vessel, the LAr can

be purified and therefore readied to fill the main detector. This saves $\sim$ 2 months of purification time in the main detector vessel. In addition, the Dewar serves as storage should the detector need to be emptied at some point during the run. Also considered was the option to fill the detector from temporary LAr vessels, purify in the main detector, and operate without the option of the storage Dewar. While this saves the cost of the storage Dewar, its not clear if there are overall cost savings considering the changes to the plumbing design this would incur.

- Cold Electronics Readout: In the baseline design the signal preamplifiers are sent through cable assemblies and custom feedthroughs to the outside Readout crates. To reduce the heat load due to the number of electrical connections we may envision a system where the signals are digitized and multiplexed in the LAr and the data are transmitted over optical links. This would reduce the number of signals out considerably (total of 100 fibers approximately) simplifing the feedthrough design as well. On the other hand, careful attention has to be paid to balance the heat load reduction due to the connection with the heat generation due to additional electronics inside. As well, the reliability of the system needs to be well understood. This particular architecture would be extremely attractive for larger scale detectors where the number of channels could be of the order of several hundred thousand channels. For MicroBooNE the advantages at this stage are not clear particularly due to the aggressive schedule.

Chapter 5

Events in the Detector

Liquid Argon Time Projection Chamber technology is ideal for addressing the MiniBooNE low energy excess because it is sensitive at low energies, capable of e/γ separation, and has excellent particle identification resulting in excellent signal efficiency and background rejection. In order to best understand the capability and sensitivity of the experiment, a detector Monte Carlo and reconstruction package are under development.

The following sections summarize first the status of the MicroBooNE simulation including a general description of the simulation setup and how events are produced, as well as some early results from studies of ν_e appearance efficiency and background rejection. Finally, sensitivity calculations based on this work and on results from MiniBooNE show that MicroBooNE's sensitivity to the MiniBooNE low energy excess will be $\sim 9\sigma$ with ~ 50 "signal" events.

5.1 Event Generation and GEANT4 Detector Simulation

Neutrino interactions in liquid argon are produced using the NUANCE v3 program, which has been suitably modified to have liquid argon as the detector medium [37]. Using the flux of the Fermilab BNB as input this program generates samples of neutrino interactions, properly normalized according to cross-section, which are then fed into a detector simulation. The modifications made to NUANCE to utilize liquid argon as the medium, as opposed to ^{16}O, will need to be further studied as the detector simulation evolves and data from liquid argon experiments become available.

GEANT4 is capable of taking these NUANCE generated neutrino interactions and propagating any final-state particles through a user-defined detector [80]. The simulation requires relevant physics processes (such as Bremsstrahlung, Compton scattering, ionization, etc...) to be specified. These processes are used to determine the step by step behavior of particles from the event generator and their subsequent products. Particles are tracked until they exit the detector volume, fall below some user-defined energy threshold, or cease to exist (via decay, absorption, etc...).

5.1.1 Physics Processes

The MicroBooNE simulation is aware of many physics processes, which are used in propagating the particles through the detector volume. Optical processes, such as Cerenkov radiation and scintillation, will also be simulated but at present have not yet been studied in detail.

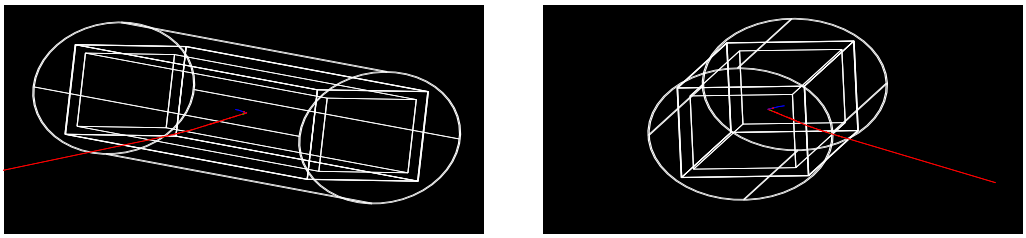

Figure 5.1: Example of a ν_μ CC-QE interaction inside a user-defined geometry. Left: The full detector consists of two concentric SS shells, surrounding a rectangular volume in which the TPC will be defined. Right: End view of the inner stainless steel shell and TPC volume.

5.1.2 Geometry

Materials such as LAr and stainless steel(SS) are defined in the simulation and assigned to the different components that are present in the detector. The initial MicroBooNE simulation can be run as either a large rectangular block of liquid argon, or as in Figure 5.1, a pair of concentric SS cylinders surrounding a volume of liquid argon. Work in defining geometry consistent with the MicroBooNE cryostat is ongoing, and details of the TPC will soon be added. The incoming Booster neutrino beam is arranged to point along the positive $\hat{z}$ axis.

Even with the simple simulation described above, much can be learned about the behavior of neutrino interactions in liquid argon. The output of the simulation can be plotted to give an estimate of the size and kinematics of typical events. Figure 5.2 depicts two CC-QE events, one for ν_e and one for ν_μ. The color scale in these events is reflective of the energy deposition in each step along a track.

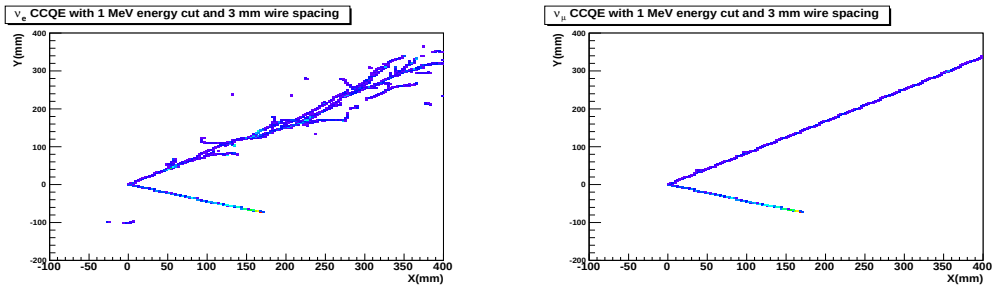

Figure 5.2: Example of a ν_e CC-QE event (Left) and a ν_μ CC-QE event (Right) in the GEANT4 LAr simulation.

In order to estimate the fiducial volume of the detector, the topology of each event class must be studied. In this vein, an initial study has been done to gauge the size of NC π^0 events. A sample of $\sim$5000 NC π^0 events was generated, and for each event the maximum shower spread along each coordinate was determined by looking for the two hits that were the furthest apart along that axis. Energy thresholds of $>$0, 5, and 20 MeV were applied to the hits considered in this study. Since the simulation does not yet include true "hits" (including wire noise and other features) yet, we group steps into 3mm bins and refer to the sum as the "hit".

Figure 5.3 shows the shower spread along each coordinate for the three different energy thresholds. One can see that the events are boosted along the beam direction, as shown by the higher mean and RMS of the $\hat{z}$-axis spread compared to the transverse directions. The average shower spread looks symmetric along the transverse $\hat{x}$ and $\hat{y}$ directions. As the energy threshold applied to hits is increased, the shower spread starts to shrink due to the low-energy "fuzz" on the outskirts of the shower being removed.

It is not clear that γ showers from NCπ^0 events or others need to be fully contained. In particular, if rejecting these events as background, only the first 2cm of the shower need to be studied to use the $\frac{dE}{dx}$ tag to identify the shower as γ-like. If these γ showers

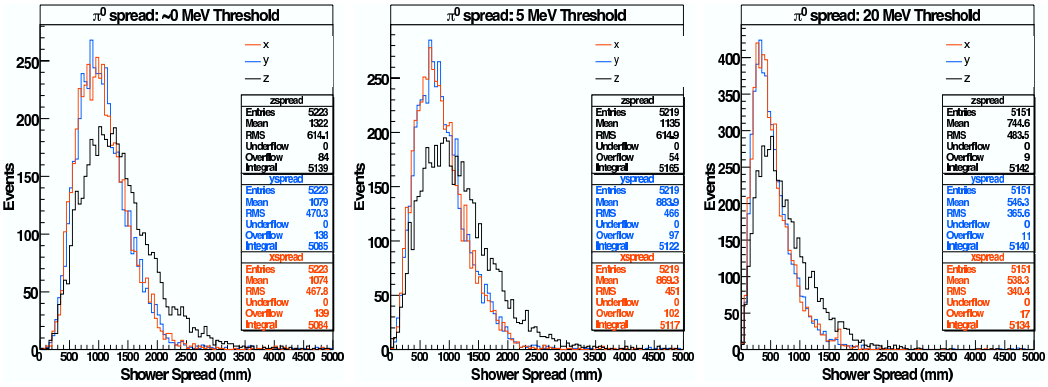

Figure 5.3: Maximum π^0 shower spread along each coordinate axis, when minimum energy thresholds of 0 MeV (Left), 5 MeV (Center), and 20 MeV(Right) are applied to the "hits" in the shower.

are signal events, more of the shower will likely need to be contained to determine the energy of the γ. Detailed study of different event classes is ongoing.

5.1.3 Efficiency Studies

With the basic simulation in place, initial studies are being performed to determine the efficiencies of several cuts at separating signal (ν_e appearance in a ν_μ beam) and background events (NC π^0) in a LArTPC. Previous analyses have shown that excellent discrimination between electromagnetic showers induced by electrons and electromagnetic showers induced by photons can be achieved by cutting on the energy deposition in the first 2.4 cm of the shower [81]. Such discrimination is desirable since it reduces the probability of misidentifying a photon as an electron, and thus possibly misidentifying a ν_e CCQE event as a NC π^0 event (where $\pi^0 \rightarrow \gamma\gamma$) where one of the photons is not reconstructed, or another singleγ background event. The MIP deposition of a $\gamma \rightarrow e^- e^+$ induced shower should be twice that of a single electron shower.

In comparing 250 MeV π^0s and electrons, Reference [81] electrons are identified with

an efficiency of 90% with an inefficieny in detecting π^0s at 6%. This proposal assumes an electron efficiency of 80% with a π^0 inefficiency of 6%. Studies with the simulation described here are ongoing.

5.2 Reconstruction and Event Displays

One of the major goals of this simulation work is to develop an automated reconstruction algorithm that can be run on data events to aid in event selection and analysis. A detector the proposed size of MicroBooNE will record many millions of events, making automated reconstruction an absolute requirement. By studying a complete simulation of the detector including effects due to electronic noise, cosmic rays, etc.,much progress can be made in the area of event reconstruction before any experiments are actually built.

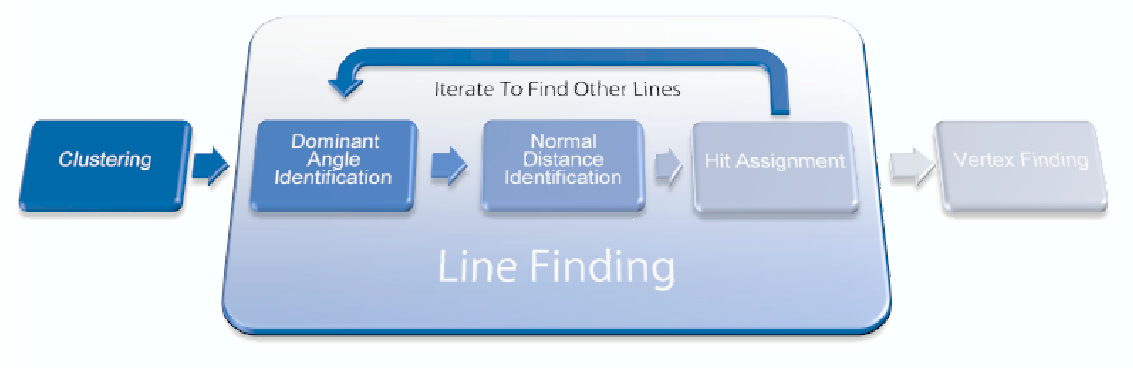

Figure 5.4: Schematic diagram of LAr Reconstruction algorithm.

The current software is implemented in C++ within the `ROOT` framwork, and is designed to reconstruct linear tracks through a parameterization by angle. Linear tracks are the ingredients to reconstruct ν_μ CCQE, CC π^+, and - in general - low multiplicity events. The schematic of the procedure is shown in Figure 5.4, and various results are shown in Figures 5.5 and 5.6[82]. The algorithm has been applied to Monte Carlo from a preexisting GEANT3 based LAr simulation, and will soon be used on the new

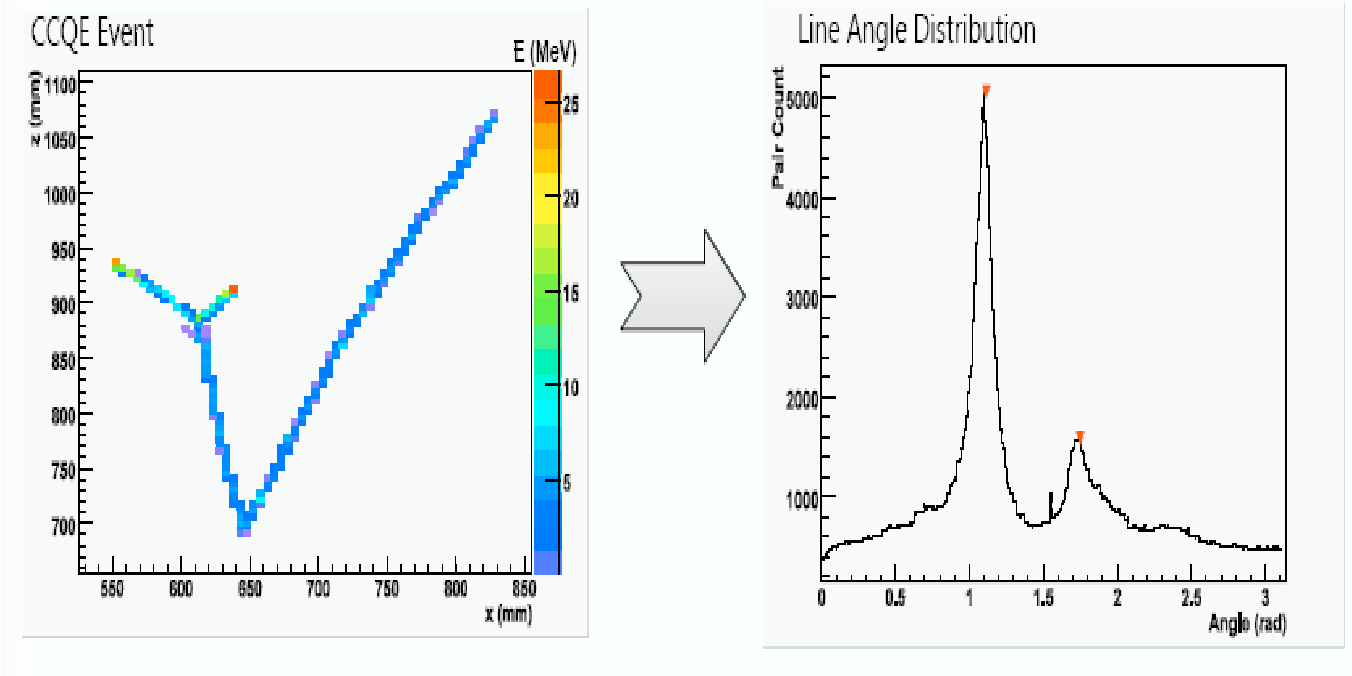

Figure 5.5: Line angle identification.

GEANT4 based simulation. It efficiently identifies primary and secondary vertices, and reconstructs the direction of the momentum for "sufficiently long and straight" tracks within 2 degrees (RMS), which is already sufficiently accurate for a first pass filter. It is worth stressing that this is done in a *fully automated way*. Moving away from analyses based on several steps of hand scanning and visual inspection of the recorded events is crucial when considering the huge amount of data that will be produced by a ∼100 ton LArTPC, such as MicroBooNE.

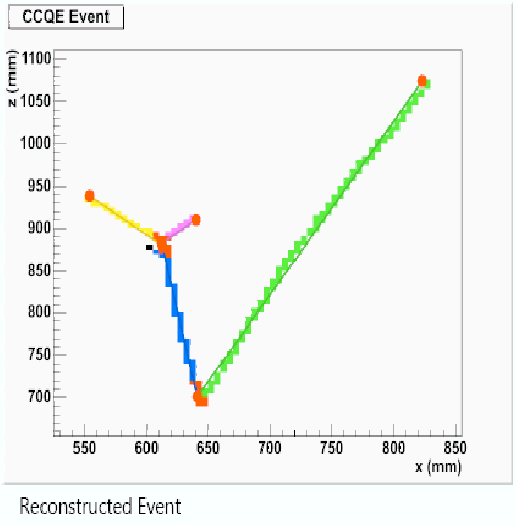

Figure 5.6: Final event reconstruction for a ν CCQE event, with the proton producing a secondary vertex.

Chapter 6

Overview of MicroBooNE Cost

The MicroBooNE detector cost is estimated to be $6.1M in materials. This estimate does not include EDIA or indirect costs. The estimate is based on experience with existing components used in similar detectors and, where possible, on vendor information. Funding for the detector will be pursued through the funding agencies, and university resources.

Table 6.1 summarizes the costs for the detector. Table 6.2 lists the material and labor items used to estimate these costs. The major cost of the detector is driven by the cryostat vessel and supporting cryogenics, followed by the TPC detector and it's electronics. The estimate for the cryostat and supporting systems comes from engineers who have constructed similar sized systems; the estimate for cryogenic storage vessels comes from a vendor quote. The electronics cost of $152 per channel is based on the Atlas calorimeter experience and on electronics made for recent test detectors at FNAL. Estimates for the signal feedthroughs is based on costs for the ATLAS calorimeter feedthroughs and this detector plans to use an identical design.

The MicroBooNE enclosure is a sheilding block hut designed to reduce cosmic ray backgrounds. The cost of the enclosure, estimated by the Fermilab Facilities Engineering

Section, is $425,000 [83], which includes materials, labor, and contingency.

Resource Items		Cost	Materials Cost Estimate	Labor Cost Estimate	Notes
Micro BooNE Project	**Conceptual Design & Cost Estimate**	**$9,358,000.00**	**$6,048,000.00**	**$3,310,000.00**	
Facility & Infrastructure		$425,000.00			FESS estimate of Shield-Block building on newly constructed concrete pad. Pad area includes space for storage vessels. Total floor-load of 600 tons, 500psf. Includes utility conduit to MB enclosure. Includes labor and contingency
Cryostat	Cryostat Vessel, Cryo/Vacuum feedthroughs & flanges, Cryostat Assembly Labor, Detector Head Vessel, LAr Filling,Vessel Insulation	$1,720,000.00	$1,420,000.00	$300,000.00	Cryostat Vessel, including feed-throughs for cryo and vacuum systems. 50+ tons fiducial volume, 175 tons LAr total. Inner cryostat 3.2m OD, 13.2m long. Sits inside vacuum vessel 4.7m OD, 13.5m long. About 100 tons empty. About 300 tons full.
Cryogenics	Storage Dewars: 1 N2, 2 LAr, LAr Purification System, Valves, plumbing, cryo parts, Cryo Controls, 2 Cryo pumps, Vacuum System, Cryogenics Assembly Labor	$2,130,000.00	$1,730,000.00	$400,000.00	Cryogenics system. Includes 5000gal N2 dewar for feed-through cooling loop. 2 23,000gal argon dewars for storage. About 300 tons total weight with liquid gases
TPC	12 sets of Signal FT flange and carriers, HV Feedthrough, Signal and HV FT Assembly, Wire Chamber Frames and Assemblies, HV Cage & resistors, Cables[1],TPC HV PS Pre-Amp power cables HV Cage Assembly	$1,266,000.00	$566,000.00	$700,000.00	3 planes, Y, U&V @60deg. 3mm pitch HV cage 500 V/cm 1 HV feed-through multiple signal feed-through along length
Electronics & Readout	Cold Pre-Amps, Electronics Boards, PA assembly/test Electronics assembly/test, LVPS, LVPS assembly/test labor, outer PA power cables, Signal/Calibration Cables, Cable assembly/test,	$2,507,000.00	$1,707,000.00	$800,000.00	10,000 channels @ $152/ch, single phase. 12 or 14 bit ADC 200-400ns digitization frequency charge injection at wire for calibration
DAQ & Monitoring	DAQ Hardware, DAQ Labor, Detector Monitoring Hardware, Det Monitoring Labor	$310,000.00	$200,000.00	$110,000.00	DAQ Hardware & labor, Detector Monitoring Hardware & Labor
Installation & Integration		$1,000,000.00	$0.00	$1,000,000.00	Installation Labor

Figure 6.1: Cost Estimate for the MicroBooNE Detector.

Schedule_Pass1

ID	Resource Name	Type	Notes	Materials Cost Estimate	Labor Cost Estimate	Cost/Use
1	Cryostat Vessel	Material		$950,000.00	$0.00	$950,000.00
2	Detector Head Vessel	Material		$200,000.00	$0.00	$200,000.00
3	Vessel Insulation	Material		$100,000.00	$0.00	$100,000.00
4	Dewar - N2	Material		$200,000.00	$0.00	$200,000.00
5	Dewar - LAr	Material		$375,000.00	$0.00	$750,000.00
6	LAr Purification System	Material		$300,000.00	$0.00	$300,000.00
7	Valves plumbing etc cryo parts	Material		$500,000.00	$0.00	$500,000.00
8	Cryo Controls	Material		$150,000.00	$0.00	$150,000.00
9	Cryo pumps	Material		$75,000.00	$0.00	$75,000.00
10	vacuum system	Material		$130,000.00	$0.00	$390,000.00
11	Lar Fill	Material		$120,000.00	$0.00	$120,000.00
12	Cryo/Vacuum feedthroughs & flanges	Material		$50,000.00	$0.00	$50,000.00
13	Signal FT flange and pin carrier	Material	Glass Pin Feed-Through. Atlas-like. 12 of these. $7000 for each flange+pin carrier combination	$7,000.00	$0.00	$84,000.00
14	HV Feedthrough	Material		$12,000.00	$0.00	$12,000.00
15	Wire Chamber Frames and Wire Assemblies	Material		$250,000.00	$0.00	$250,000.00
16	HV Cage and resistors	Material		$250,000.00	$0.00	$250,000.00
17	Cryostat Assembly Labor	Work		$0.00	$300,000.00	$300,000.00
18	Cryogenics Assembly Labor	Work		$0.00	$400,000.00	$400,000.00
19	Signal and HV FT Assembly Labor	Work		$0.00	$200,000.00	$200,000.00
20	Wire Plane Assembly Labor	Work		$0.00	$250,000.00	$250,000.00
21	HV Cage Assembly Labor	Work		$0.00	$200,000.00	$200,000.00
22	Signal Cables	Material	Three sets of cables: octopus cables from TPC planes to cryo FT; one set running from the cryo vessel FT to the Vacuum vessel FT; one set from the outside of the vessel to the readout racks	$120,000.00	$0.00	$120,000.00
23	HV Cables	Material	130 KV cable and 300V cables	$10,000.00	$0.00	$10,000.00
24	Calibration Cables	Material		$15,000.00	$0.00	$15,000.00
25	Signal/Calibration Cable assembly/testing	Work		$0.00	$150,000.00	$150,000.00
26	HV cable assembly/testing	Work		$0.00	$50,000.00	$50,000.00
27	Pre-Amp power cables	Material		$12,000.00	$0.00	$12,000.00
28	TPC HV PS	Material		$25,000.00	$0.00	$25,000.00
29	LV PS	Material		$40,000.00	$0.00	$40,000.00
30	LV PS assembly/testing labor	Work		$0.00	$50,000.00	$50,000.00
31	PMTs	Material		$100,000.00	$0.00	$100,000.00
32	PMT assembly/testing	Work		$0.00	$80,000.00	$80,000.00
33	Cold Pre-Amp	Material	10,000 channels at $32 per channel	$320,000.00	$0.00	$320,000.00
34	PA Assembly/Testing	Work		$0.00	$300,000.00	$300,000.00
35	Electronics Boards	Material	All boards outside of the Vessel: Readout boards; Crate control boards; Calibration boards. 10,000 channels at combined $120 per channel...	$1,200,000.00	$0.00	$1,200,000.00
36	Electronics Assembly/Testing	Work		$0.00	$300,000.00	$300,000.00
37	DAQ Hardware	Material		$150,000.00	$0.00	$150,000.00
38	DAQ Labor	Work		$0.00	$100,000.00	$100,000.00
39	Detector Monitoring Hardware	Material		$50,000.00	$0.00	$50,000.00
40	Det Monitoring Labor	Work		$0.00	$10,000.00	$10,000.00
41	Installation Labor	Work		$0.00	$1,000,000.00	$1,000,000.00
42	BNL Mech Engineer	Work		$0.00	$0.00	$0.00
43	FNAL Mech Engineer	Work		$0.00	$0.00	$0.00
44	Design/Drafting	Work		$0.00	$0.00	$0.00
45	Electrical Engineer	Work		$0.00	$0.00	$0.00
46	Physicist	Work		$0.00	$0.00	$0.00
47	Technician	Work		$0.00	$0.00	$0.00

Page 1

Figure 6.2: Detailed list of costs for MicroBooNE.

Chapter 7

Conclusions

We propose to design, construct, and run a Liquid Argon TPC experiment, MicroBooNE, to understand low energy neutrino interactions and serve as the next step in advancing the technology towards massive LArTPCs.

MicroBooNE brings the appropriate technology to address the MiniBooNE low energy excess and study reaction processes of relevance for future long baseline experiments. MiniBooNE, and other modern day neutrino experiments like NOvA and T2K, cannot differentiate electrons from photons. By contrast, MicroBooNE, using LArTPC technology, has excellent performance down to several MeV and can differentiate electrons from photons.

MicroBooNE will be located next to the MiniBooNE detector hall and exposed to the on-axis Booster Neutrino Beam and an off-axis component of the NuMI beam.

Bibliography

[1] A. A. Aguilar-Arevalo *et al.* [The MiniBooNE Collaboration],"A Search for Electron Neutrino Appearance at the Delta m**2 1 eV**2 Scale," Phys. Rev. Lett. **98**, 231801 (2007) [arXiv:0704.1500 [hep-ex]].

[2] M. Maltoni and T. Schwetz,"Sterile neutrino oscillations after first MiniBooNE results,"arXiv:0705.0107 [hep-ph].

[3] S. Goswami and W. Rodejohann, "MiniBooNE Results and Neutrino Schemes with 2 sterile Neutrinos: Possible Mass Orderings and Observables related to Neutrino Masses," arXiv:0706.1462 [hep-ph].

[4] H. Pas, S. Pakvasa and T. J. Weiler,"Sterile - active neutrino oscillations and shortcuts in the extra dimension," Phys. Rev. D **72**, 095017 (2005) [arXiv:hep-ph/0504096].

[5] C. Giunti and M. Laveder, "ν_e Disappearance in MiniBooNE," arXiv:0707.4593 [hep-ph].

[6] T. Katori, A. Kostelecky and R. Tayloe,"Global three-parameter model for neutrino oscillations using Lorentz violation,"Phys. Rev. D **74**, 105009 (2006) [arXiv:hep-ph/0606154].

[7] A. de Gouvea and Y. Grossman, "A three-flavor, Lorentz-violating solution to the LSND anomaly," Phys. Rev. D **74**, 093008 (2006) [arXiv:hep-ph/0602237].

[8] J. A. Harvey, C. T. Hill and R. J. Hil, 0708.1334 [hep-ph].

[9] X. Q. Li, Y. Liu and Z. T. Wei, "Neutrino decay as a possible interpretation to the MiniBooNE observation with unparticle scenario," arXiv:0707.2285 [hep-ph].

[10] S. Amerio *et al.* [ICARUS Collaboration], "Design, construction and tests of the ICARUS T600 detector," Nucl. Instrum. Meth. A **527**, 329 (2004).

[11] "Recommendations to the Department of Energy and the National Science Foundation on a Future U.S. Program in Neutrino Oscillations", submitted by the Neutrino Scientific Assesment Group. http://www.science.doe.gov/hep/hepap_reports.shtm

[12] Talk presented by Rex Tayloe at Lepton Photon '07. http://chep.knu.ac.kr/LP07/

[13] G. Drexlin [KATRIN Collaboration], "KATRIN: Direct measurement of a sub-eV neutrino mass," Nucl. Phys. Proc. Suppl. **145**, 263 (2005).

[14] Rex Tayloe, Private Communication

[15] G.Zeller, "Neutrino Cross Sections Past, Present, and Future," Fermilab Wine and Cheese Seminar and NuInt07 Summary Talk, May 30, 2007.

[16] C.H. Llewellyn Smith, Phys. Rep. **C3**, 261 (1972).

[17] J.J. Kelley, Phys. Rev. **C70**, 068202 (2004).

[18] J. Phys. **G28**, R1 (2002).

[19] R. Gran et al.,Phys. Rev. **D74**, 052002 (2006)

[20] T. Katori, talk presented at NuInt07, Fermilab, May 2007.

[21] S. Nakayama *et al.*, Phys. Lett. **B619**, 255 (2005).

[22] J. Link, talk presented at the NuInt07 Workshop, Fermilab, May 30, 2007.

[23] S. Kopp, "Accelerator Neutrino Beams," Physics Reports **439**, 101-159 (2007).

[24] A. Aguilar-Arevalo (MiniBooNE and MINOS Collaborations), "Neutrinos from the NuMI beam line in the MiniBooNE detector," talk presented at PANIC '05, Oct. 2005.

[25] D. Finley *et al*, "A Large Liquid Argon Time Projection Chamber for Long-baseline, Off-Axis Neutrino Oscillation Physics with the NuMI Beam," Fermilab-FN-0776-E, September 21, 2005.

[26] Fermilab Steering Group Report, August, 2007.

[27] A. Curioni, B. T. Fleming and M. Soderberg, "The Yale Lar TPC," arXiv:0708.0875 [physics.ins-det], A. Curioni, B.T.Fleming, M. Soderberg, "The Yale Liquid Argon Time Projection Chamber", in preparation, to be submitted to JINST

[28] http://t962.fnal.gov

[29] http://lartpc-docdb.fnal.gov/cgi-bin/ShowDocument?docid=265 & http://lartpc-docdb.fnal.gov/cgibin/ShowDocument?docid=67, Work at FNAL to achieve long electron drift lifetime in liquid argon. By D. Finley, et al., FERMILAB-TM-2385-E (Oct 2006) 9p.

[30] Z. Djurcic, "Results of the MiniBooNE Oscillation Experiment," 13th Lomonsov Conference on Elementary Particle Physics, Moscow, Russia, Aug 23-29, 2007.

[31] E. Prebys, talk given at the Aug.20-21 microBooNE meeting, slides available upon request.

[32] M. G. Catanesi *et al.* [HARP Collaboration], "Measurement of the production cross-section of positive pions in p Al collisions at 12.9-GeV/c," Nucl. Phys. B **732**, 1 (2006) [arXiv:hep-ex/0510039].

[33] Flux files are available upon request, contact gzeller@fnal.gov.

[34] Michel Sorel, fermilab-thesis-2005-07

[35] A. Ferrari, P.R. Sala, A. Fasso, J. Ranft, "FLUKA: A multi-particle transport code (Program version 2005)," CERN-2005-010, SLAC-R-773, INFN-TC-05-11, Oct 2005.

[36] D.G. Michael *et al*, "Preliminary Results from MINOS on Muon Neutrino Disappearance Based on an Exposure of 2.5×10^{20} 120 GeV Protons on the NuMI Target," preprint submitted to Lepton-Photon, arXiv:0708.1495 (July, 2007).

[37] Need a reference for NUANCE code.

[38] S.E. Kopp and Z. Pavolovic, Private Communication

[39] Z. Djurcic, talk presented at the 13th Lomonosov Conference on Elementary Particle Physics, Moscow, Russia, 2007.

[40] C. Rubbia, "The Liquid-argon time projection chamber: a new concept for Neutrino Detector", CERN-EP/77-08 (1977).

[41] P. Benetti *et al.*, "Argon purification in the liquid phase," Nucl. Instrum. Meth. A **333**, 567 (1993).

[42] D. Finley *et al.*. "Work at FNAL to achieve long electron drift lifetime in liquid argon." FERMILAB-TM-2385-E (Oct 2006) 9p.

[43] H. Davis, J. Chem Phys, vol 37 no 5 (1962) pp. 947-956

[44] W. Shockley, Bell System Tech. J., vol. 30 (1951) pp. 990

[45] M. Cohen, J. Lekner, Phys. Rev., vol. 158 no 2 (1967) pp. 305-309

[46] E.M. Guschin et al., J. Exper. And Theor. Phys., vol 82 no 5 (1982) pp 1485-1490 (in Russian), translated as Sov. Phys. JETP vol. 55 (1982) pp 650-654

[47] S. Amoruso et al., Nucl. Instr. and Methods, vol. A516 (2004) pp 68-79

[48] L. S. Miller et al., Phys. Rev., vol. 166 no 3 (1967) pp 871-878

[49] H. Schnyders et al., Phys Rev., vol 150 no 1 (1966) pp 127-146

[50] B. Halpern et al., Phys. Rev., vol 156 no 2 (1967) pp 351-352

[51] W. Walkowiak, Nucl. Instr. and Methods, vol. A440 (2000) pp 288-294

[52] E. Shibamura et al., Phys. Rev. A, vol 20 No 6 (1979) pp 2547-2555

[53] T. Doke, Port. Phys vol. 12 (1981) pp 9-48

[54] T. Doke, Nucl Instr. and Methods, vol. 196 (1982) pp 87-96

[55] E. Aprile et al., Noble Gas Detectors, Wiley-VCH 2006 ISBN: 3-527-40597-6

[56] S. Amoruso et al., Nucl Instr and Methods, vol. A523 (2004) pp 275-286

[57] R. T. Scalettar et al., Phys. Rev. A25 (1982) pp 2419

[58] E. Aprile et al., Nucl. Instr. and Methods A261 (1987) pp 519

[59] http://www.ansoft.com/products/em/max2d/

[60] http://www.fwmetals.com/resources_specsheets/304v.php

[61] http://lartpc-docdb.fnal.gov/cgi-bin/ShowDocument?docid=16

[62] http://www.spaceagecontrol.com/calccabm.htm

[63] O. Bunemann et al., Can. Jou. of Res., v A27 (1949) pp191-206

[64] M. Rossella et al., ICARUS collaboration meeting, LNGS 10/3/03 http://www.aquila.infn.it/icarus/icarus_coll_03/rossella.pdf

[65] R. Veenhof, Garfield Simulation of Gaseous Detectors, http://garfield.web.cern.ch/garfield/

[66] http://www.aps.anl.gov/asd/me/Calculators/ElasticBeam2.html

[67] P. Cennini *et al.*, coincidence with ionizing tracks in a chamber," Nucl. Instrum. Meth. A **432**, 240 (1999).

[68] T. Doke *et al.*, Nucl. Instrum. Meth. A **269**, 291 (1988).

[69] M. Di Marco, P. Peiffer and S. Schonert, arXiv:physics/0701001.

[70] N. Ferrari [Warp Collaboration], J. Phys. Conf. Ser. **39**, 111 (2006).

[71] M. G. Boulay and A. Hime, Astropart. Phys. **25**, 179 (2006).

[72] E. Conti, G. Carugno and A. Intravaia, Nucl. Instrum. Meth. A **382**, 475 (1996).

[73] P. Benetti, C. Montanari, G. L. Raselli, M. Rossella and C. Vignoli Nucl. Instrum. Meth. A **505**, 89 (2003).

[74] J.M. Moss *et al.*, "Applications of Antineutrino Detector Technology to Counterterrorism," Physics Div. Research Review, LA-14112-PR.

[75] V. Radeka, "LOW NOISE TECHNIQUES IN DETECTORS," Ann. Rev. Nucl. Part. Sci. **38**, 217 (1988). ARNUA,38,217;

[76] E.M. Guschin et al., J. Exper. And Theor. Phys., vol 82 no 5 (1982) pp 1485-1490 (in Russian), translated as Sov. Phys. JETP vol. 55 (1982) pp 650-654

[77] G. A. Erskine, Nucl. Instr. And Methods, vol. 105 (1972) pp. 565-572

[78] http://lartpc-docdb.fnal.gov/cgi-bin/ShowDocument?docid=96

[79] See for example: http://arxiv.org/pdf/physics/0611299

[80] GEANT4

[81] E. Kearns *et al.* "A Proposal for a Detector 2 km Away From the T2K Neutrino Source"

[82] C. Anderson, talk given at "Neutrino Physics with LArTPCs Workshop", Yale, July 2006

[83] Project Definition Report, MicroBooNE Sheild Block Building, FESS/Engineering Project No.6-7-82

[84] S. S. Gershtein, Yu. Ya. Komachenko, and M. Yu. Khlopov, Sov. J. Nucl. Phys. 33, 860 (1981).

[85] P. Alibran *et al.*, Phys. Lett. 74B, 422 (1978).

Chapter 8

Appendix A

Sterile Neutrinos

Results from LEP limit the number of flavors of active neutrinos to three. However, if LSND and MiniBooNE are signals due to oscillations, then the three oscillation signal-types – Atmospheric, Solar, and LSND/MiniBooNE – cannot be explained with the three Standard Model neutrinos. Sterile neutrinos, neutrinos which do not interact via the weak interaction but can oscillate with the Standard Model neutrinos, have been proposed in a variety of ways to explain the LSND/MiniBooNE data. Following is a description of some of these ideas.

3+2 Models: A recent work integrating the MiniBooNE low energy excess into the other oscillation signals via sterile neutrinos is described here [2]. The authors show that a 3+1 model does not fit the MiniBooNE and LSND data, however a 3+2 or 3+3 model does. In fact, MiniBooNE is in perfect agreement with the LSND result and the null short baseline results from NOMAD and Karmen in a 3+2 model. There is tension at the 3 sigma level when results from disappearance experiments (Bugey, CDHS, Chooz, Palo Verde) are included. Figure 8.1 shows the best fit to the MiniBooNE low energy

excess in this 3+2 model.

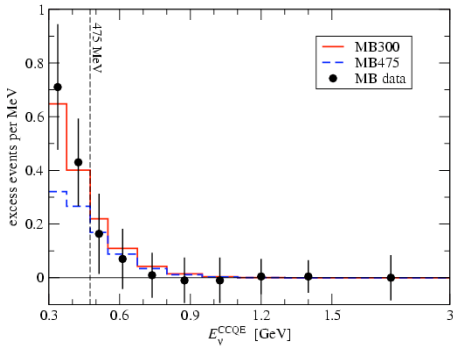

Figure 8.1: Fit to the MiniBooNE data in a 3+2 model using the data down to E_ν=475 MeV (dashed) and down to E_ν=300 MeV (solid) [2]. At the time this analysis was done, MiniBooNE had reported data only down to 300 MeV.

Another recent work [3] describes the implications of a 3+2 model on related neutrino measurements. Specifically, the authors point out that while for some mass orderings for 3+2 models, where the mass orderings describe the masses of the sterile neutrinos with respect to the active ones, the total sum of neutrino masses is near 2 eV, for others the total sum of the neutrino masses is as high as 10 eV. Bounds from cosmological data restrict the sum of the neutrino masses to be a couple of eV. While some of these constraints can be evaded, it is unlikely that they can be relaxed to 10 eV.

Results from the KATRIN experiment [13] could also rule out some of the mass orderings. Specifically, 3+2 scenarios with both sterile neutrinos heavier than the rest cannot be addressed by KATRIN, while the other possible mass orderings will result in a signal in KATRIN. Results from neutrino-less double beta decay will be unlikely to shed light on these models.

Shortcuts Through Extra Dimensions: While many of the theoretical interpretations of the MiniBooNE excess have been post-dictions, it is notable that the model

described here is a prediction [4]. The authors put forth a model where sterile neutrinos can take shortcuts in extra dimensions. This process modifies the active-sterile mixing probablilty such that for different possible values of a shortcut parameter and mixing parameters, different possible mixing probabilites are suggested. For all, the prediction was that no significant signal would be observed in the oscillation region, while a signal was predicted at low energies – as was observed by MiniBooNE. This prediction is shown in Figure 8.2.

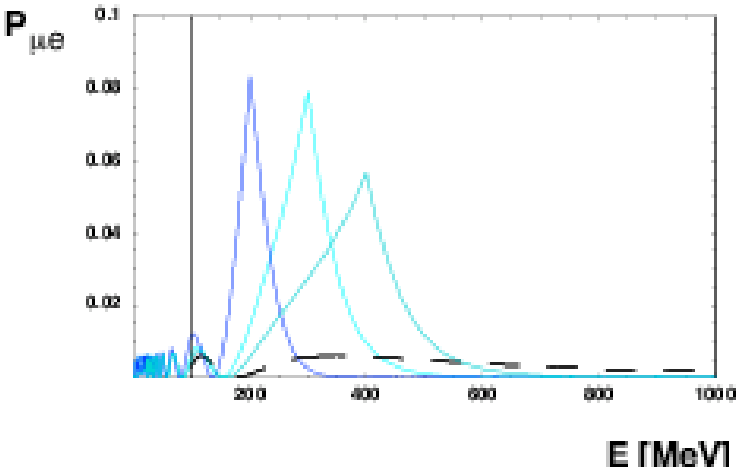

Figure 8.2: Prediction for a low energy excess on MiniBooNE in a 3+1 model where the sterile neutrino can take shortcuts in Extra Dimensions [4].The different curves correspond to different values of the mixing parameters and a shortcut parameter.

Electron Neutrino Disappearance

Electron-neutrino disappearance as observed by the Gallium radioactive source experiments is suggested [5] as the source of the excess of events on MiniBooNE. A renormalization of the absolute neutrino flux prediction for MiniBooNE will change the number of expected intrinsic ν_e events in the beam. This, coupled with ν_e disappearance at high

energies as suggested by the Gallium results, would leave a low energy excess as observed by MiniBooNE.

Lorentz Violation

Several models suggest reconciling the LSND and MiniBooNE signals with the other neutrino oscillation signals by invoking Lorentz Violation. Lorentz Violation has been suggested as a mechanism producing neutrino oscillations. One such model [6] with one mass parameter and two coefficients for Lorentz Violation can replace the conventional description of neutrino oscillations and describe all the exisitng data. The authors of this work are presently working towards incorporating the MiniBooNE low energy excess into the model [14].

Another [7] suggests that one of the active neutrinos couples to a source of Lorentz Violation. All neutrino data is accomodated, including LSND, by varying the flavor composition of the neutrino and the energy dependence of the effect. While the LSND signal can be accomodated, the model must be very fine-tuned to do so.

Neutrino-Photon Interactions

While many interpretations of LSND and the MiniBooNE low energy excess assume the events are electron-like, MiniBooNE cannot distinguish between electrons and photons. A recent paper [8] suggests the events could be due to a Standard Model process involving the coupling of the photon, Z-boson, and ω-meson at finite baryon density. Of particular interest is the process $\nu + N \rightarrow \nu + \gamma + N$ (see Fig. 8). This process had been explored by [84] to try to explain the Gargamelle excess between 1 and 10 GeV [85]. (Couplings between the photon, Z(W)-boson, and the ρ or ϕ mesons are negligible. The ω coupling is expected to dominate based on phenomenological observations [8]).

Considering an incident neutrino of any flavor colliding with a stationary nucleon, and

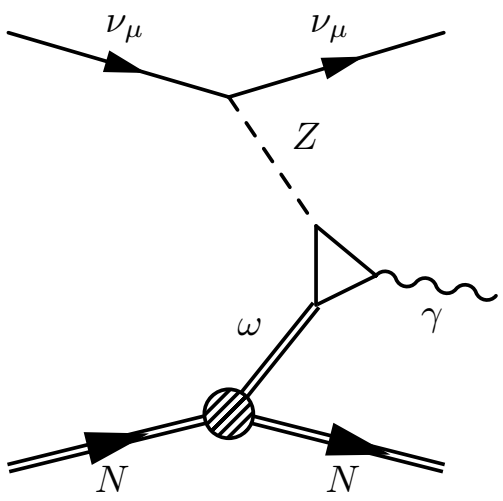

Figure 8.3: Feynman diagram for the process $\nu + N \rightarrow \nu + \gamma + N$ with coupling between γ, Z, and ω.

neglecting recoil, the resulting total cross section is $2.6\text{x}10^{-41}(E_\nu/\text{GeV})^6(g_\omega/10.0)^4$ cm^2, where E_ν is the incident neutrino energy and the value of g_ω is uncertain but expected to be on the order of 10.

These anomaly-mediated neutrino-photon interactions at finite baryon density may also produce a competitive contribution to neutron star cooling at temperatures $\gtrsim 10^9$ K and early stage evolution. Thus, if MicroBooNE sees a positive signal for anomaly-mediated neutrino-photon interactions, interesting measurements can be made that will affect not only neutrino physics but astrophysics as well. These include a measurement of g_ω and the form factor for the nucleus.

Neutrino Decay

A recent model suggests a possible interpretation for the low energy excess as a ν_μ decay to a ν_e and an "unparticle" [9]. This model also suggests possible decays to $\overline{\nu}$, however this decay mode is suppressed. In this model, the events should be very forward and results at lower energies should be relevant.